

DOT/FAA/AR-95/108

Office of Aviation Research
Washington, D.C. 20591

Characterization of Early Stages of Corrosion Fatigue in Aircraft Skin

February 1996

Final Report

This document is available to the U.S. public
through the National Technical Information
Service, Springfield, Virginia 22161.



**U.S. Department of Transportation
Federal Aviation Administration**

19960424 107

DETC QUALITY INSPECTED 1

NOTICE

This document is disseminated under the sponsorship of the U.S. Department of Transportation in the interest of information exchange. The United States Government assumes no liability for the contents or use thereof. The United States Government does not endorse products or manufacturers. Trade or manufacturer's names appear herein solely because they are considered essential to the objective of this report.

1. Report No. DOT/FAA/AR-95/108	2. Government Accession No.	3. Recipient's Catalog No.	
4. Title and Subtitle Characterization of Early Stages of Corrosion Fatigue in Aircraft Skin		5. Report Date February 1996	
		6. Performing Organization Code	
7. Author(s) C. G. Schmidt, J. E. Crocker, J. H. Giovanola, C. H. Kanazawa, D. A. Shockey		8. Performing Organization Report No. PYD-5082	
9. Performing Organization Name and Address SRI International 333 Ravenswood Avenue Menlo Park, CA 94025-3493		10. Work Unit No. (TRAIS)	
		11. Contract or Grant No. 93-G-065	
12. Sponsoring Agency Name and Address U.S. Department of Transportation Federal Aviation Administration Office of Aviation Research Washington, D.C. 20591		13. Type of Report and Period Covered Sept. 93 - Sept. 95 Final Report	
		14. Sponsoring Agency Code AAR-430	
15. Supplementary Notes FAA Project Monitor: Dr. Thomas Flournoy			
16. Abstract <p>SRI International is conducting research to characterize and quantitatively describe the early stages of corrosion fatigue in the fuselage skin of commercial aircraft. Specific objectives are to gain an improved deterministic understanding of the transition from corrosion pit to short crack to long crack and to delineate the effects of environment, skin surface condition, and loading conditions on crack nucleation and propagation rates. This Phase I report summarizes the effort in the first two years of this five-year program.</p> <p>The results suggest that corrosion fatigue in Alclad 2024-T3 involves two competing crack nucleation mechanisms—hydrogen effects in the cladding and pitting at constituent particles in the core alloy. In a given situation, the mechanism which dominates depends on environment (particularly pH) and (weakly) on specimen orientation. Cracks do not necessarily nucleate at the largest corrosion pit, suggesting that the main effect of a pit is not to raise the local stress. Rather, a high local hydrogen concentration associated with accelerated corrosion at a pit could cause cracking in a nearby favorably oriented grain.</p> <p>Propagation rates of short cracks were slightly higher in acidic environments and in specimens with painted surfaces, but were unaffected by material orientation and surface roughness. Corrosion fatigue observations and data from the laboratory experiments are being compared with those from field components to check whether research results represent in-service experience.</p>			
17. Key Words corrosion crack nucleation aluminum fatigue aircraft skin clad 2024-T3 pitting Alclad hydrogen		18. Distribution Statement This document is available to the public through the National Technical Information Service, Springfield, VA 22161.	
19. Security Classi. (of this report) Unclassified	20. Security Classi. (of this page) Unclassified	21. No. of Pages 148	22. Price

CONTENTS

Section	Page
EXECUTIVE SUMMARY	ix
1 INTRODUCTION.....	1
2 OBJECTIVES AND APPROACH.....	5
3 EXPERIMENTAL PROCEDURE.....	7
3.1 Test Material	7
3.2 Specimen Fabrication	15
3.3 Stress Calculation	15
3.4 Corrosion-Fatigue Testing and Data Analysis	23
3.5 Metallographic Preparation.....	25
4 EXPERIMENTAL RESULTS AND DISCUSSION	27
4.1 Pitting Characteristics.....	27
4.2 Corrosion-Fatigue Tests.....	35
4.2.1 Corrosion-Fatigue Crack Nucleation Kinetics	35
4.2.2 Corrosion-Fatigue Crack Propagation Kinetics.....	53
4.3 Hydrogen Effects Experiments	82
5 SUMMARY AND CONCLUSIONS.....	93
5.1 Comparison of Corrosion-Fatigue Damage Produced In-Service Versus in the Laboratory	93
5.2 Corrosion-Fatigue Crack Nucleation.....	93
5.3 Corrosion-Fatigue Crack Propagation	94
6 REFERENCES	95
APPENDIX	A-1

FIGURES

Figure		Page
1	Critical conditions for corrosion-fatigue crack nucleation	3
2	Location of panels obtained from retired Boeing 737 aircraft.....	8
3	Section of recovered Boeing 737 fuselage	9
4	Cross section of Boeing 737 aircraft skin	10
5	Unetched metallographic cross sections of skin material from a retired Boeing 737 aircraft showing the distribution of constituent particles.....	11
6	Etched metallographs cross sections of skin material from a retired Boeing 737 aircraft showing grain structure	12
7	Anodized metallographic cross sections of skin material from a retired Boeing 737 aircraft showing the grain structure of the Alclad	14
8	Tapered corrosion-fatigue specimen.....	16
9	Photomicrographs showing the roughness of the through-thickness surface of untested corrosion-fatigue specimens	17
10	Surface roughness profiles from tapered tensile fatigue specimens.....	19
11	Load-strain behavior for as received and clad only Boeing 737 skin material specimens.....	21
12	Stress-strain behavior for Boeing 737 skin material with paint and clad removed (bare material).....	22
13	Distribution of cracks on tapered gage section	24
14	Pit on outer surface of skin from Boeing 737 aircraft.....	28
15	Corrosion-fatigue crack nucleation from pre-existing pits in the Alclad layer of Boeing 737 skin material	29
16	Typical corrosion damage on bare specimens (clad and coatings removed) of aircraft skin material	30
17	Crystallographic pits on a through-thickness plane of the Alclad layer of a corrosion-fatigue specimen in the as received condition (Specimen 2).....	31

Figure		Page
18	Pitting damage on a through-thickness plane of a corrosion-fatigue specimen in the as received condition (Specimen 41).....	33
19	Corrosion damage on a through-thickness plane of as received skin material after a 4-day exposure to pH10 salt solution.....	34
20	Number of cracks on replicate test specimens.....	38
21	Effect of pH on the number of cracks.....	39
22	Effect of specimen orientation on the number of cracks.....	40
23	Effect of surface roughness on the number of cracks.....	41
24	Effect of surface coating on the number of cracks	42
25	Residuals for crack nucleation analysis.....	49
26	Effect of pH on the crack growth rate of small cracks in aircraft skin	55
27	Effect of orientation on the crack growth rate of small cracks in aircraft skin.....	61
28	Effect of surface roughness on the crack growth rate of small cracks in aircraft skin.....	66
29	Effect of surface coating on the crack growth rate of small cracks in aircraft skin.....	71
30	Crack growth rate trends of all corrosion-fatigue tests performed on aircraft skin material in salt water.....	75
31	Residuals for crack propagation analysis.....	78
32	Comparison of corrosion-fatigue crack growth rates in laboratory air and NaCl solutions.....	81
33	Corrosion-fatigue crack nucleation from pit in bare 2024-T3 aluminum.....	83
34	Corrosion-fatigue crack nucleation in the cladding of a 2024-T3 aluminum alloy	84
35	Corrosion-fatigue crack nucleation in the clad layer of Alclad 2024-T3 aircraft skin.....	85
36	Cycles to failure for tests conducted in air after various pretreatments.....	88
37	Fracture surfaces of corrosion-fatigue specimens tested in laboratory air after exposure to various pretest environments.....	90

TABLES

Table		Page
1	Corrosion-Fatigue Tests Used in the Analysis of the Nucleation and Growth Rate of the Early Stages of Cracking	36
2	Comparison of Crack Counts in Replicate Tests.....	37
3	Effect of pH on Crack Nucleation and Growth Rate.....	43
4	Effect of Orientation on Crack Nucleation and Growth Rate	44
5	Effect of Roughness on Crack Nucleation and Growth Rate	45
6	Effect of Surface Coating on Crack Nucleation and Growth Rate.....	46
7	Statistical Analysis of the Number of Cracks on Corrosion-Fatigue Specimens.....	48
8	Statistical Analysis of the Crack Growth Rate Determined from the Corrosion-Fatigue Specimens	76
9	Corrosion-Fatigue Tests Conducted in Air after Various Pretreatments.....	87

EXECUTIVE SUMMARY

Corrosion fatigue in difficult-to-access areas of an aircraft fuselage is an occasional problem in commercial aircraft and has the potential to affect the structural integrity and the useful life of aircraft structures. The effects of fatigue and corrosion have been extensively documented; however, their synergy continues to be an area of considerable interest that is not thoroughly understood.

This report summarizes the technical accomplishments of the first two years of a continuing study at SRI International to characterize the early stages of corrosion fatigue of the skin of commercial aircraft fuselages. To achieve this objective, laboratory experiments were conducted to observe corrosion-fatigue cracking behavior and control the conditions that influence the behavior. To better relate the results of this investigation to in-service aircraft, we conducted our laboratory experiments on fuselage skin specimens obtained from a retired Boeing 737 aircraft.

We developed an experimental technique to produce corrosion fatigue cracks in the laboratory in a manner that allowed examination of crack nucleation and growth kinetics in both a statistical and deterministic manner. A range of environments, material conditions, and loading conditions were investigated experimentally in an effort to assess their effect on the crack nucleation and growth rate.

We found that

- Crack nucleation in bare material (i.e., clad and paint removed) was slower than crack nucleation in clad material. The mechanisms of crack nucleation were substantially different in these two materials: in bare material, cracks nucleated at constituent particles, whereas in clad material, cracks usually nucleated at or near crystallographic pit colonies.
- Crack nucleation from crystallographic pits in the clad did not always occur at the largest pit. The lack of correlation between crack nucleation sites and geometrical features suggests that the main effect of a pit is not to raise the local stress. Rather a high local hydrogen concentration in the clad created by accelerated corrosion processes associated with pitting possibly promoted cracking in a nearby favorably oriented grain.
- In aircraft skin, the crack nucleation mechanism that dominates depended on environment (e.g., pH), the presence or absence of a clad layer, and perhaps,

additional variables not within the scope of this investigation, such as material composition and heat treatment.

- Crack propagation rates in the early stages of corrosion fatigue were slightly higher in a pH 2 environment as compared to pH 6 or pH 10 environments. This result is generally consistent with the results of other investigators and is attributed to the enhancement of cathodic reaction rates in acidic solutions.
- Surface roughness did not affect the early stages of corrosion-fatigue crack propagation. However, cracks growing from exposed edges of painted skin material had a slightly higher crack growth rate than unpainted material. We speculate that a local occluded environment may be the reason for the enhanced crack growth rate.

Our laboratory tests were performed under conditions relevant to conditions in service without necessarily simulating them. Our intention was to conduct corrosion fatigue tests that would yield results that would clarify the underlying mechanisms. Additional experimental and analytical work will be necessary to translate a new or more comprehensive understanding of the early stages of damage into more reliable life prediction capability and new opportunities to mitigate corrosion-fatigue cracking in aircraft skin.

Section 1

INTRODUCTION

Corrosion fatigue in difficult-to-access areas of an aircraft fuselage is an occasional problem in commercial aircraft and has the potential to affect the structural integrity and the useful life of aircraft structures. The effects of fatigue and corrosion have been extensively documented; however, their synergy continues to be an area of considerable interest that is not thoroughly understood. As a result, the Federal Aviation Administration, through the National Aging Aircraft Research Program (NAARP) initiated a program of research to quantitatively investigate the interaction of corrosion and fatigue in the presence of an aggressive chemical environment.

Specifically, the NAARP seeks to develop an understanding of the synergism between mechanical fatigue and corrosion; to develop crack growth rate data and estimate residual strength of fuselage panels with cracks, through tests involving full-scale and skin panel specimens; and to develop inspection interval criteria with an associated probability of detection for each nondestructive inspection technique.* We designed the SRI investigation to contribute to the NAARP objectives and to complement ongoing research supported by the FAA Grants Program and NASA, as well as efforts by aircraft manufacturers.

Most previous studies of environmental effects on corrosion fatigue have emphasized the rate of propagation of long cracks, as opposed to the nucleation of cracks. This is, at least in part, due to the sensitivity of modern design philosophy, such as damage tolerance design, on the fatigue crack propagation rate. Less clear, though, is the utility of understanding the effect of environment on the nucleation kinetics of fatigue cracks, because current design practices do not require a knowledge of crack nucleation kinetics.

Nevertheless, despite the lack of a clear, direct, and immediate application of crack nucleation kinetics in aircraft design, improving our understanding of the environmental effects on fatigue crack nucleation has significant value. That value stems from the continual need to develop improved measures to retard the effects of environment and fatigue wherever and whenever possible. The inhibitive measures could involve the design of the metallic components of the skin

*Program Plan, National Aging Aircraft Research Program, DOT/FAA/CT-88/32-1, Department of Transportation, Federal Aviation Administration Technical Center, Atlantic City International Airport, New Jersey 08405 (September 1991).

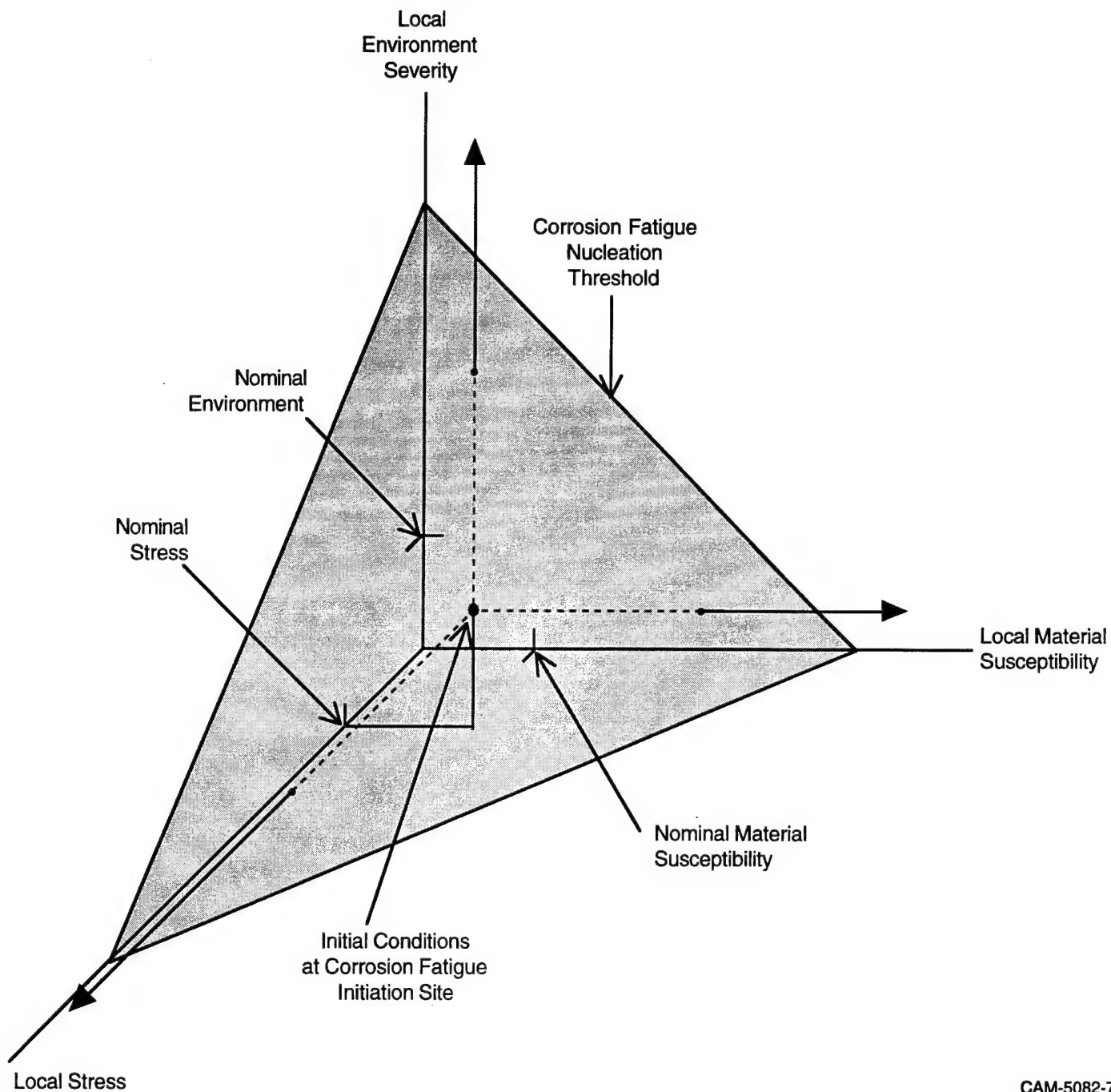
(core and clad), the choice of coatings (primers, paints, and corrosion inhibitors), and the design of skin splices.

The development of improved inhibitive measures requires, in part, a broader understanding of the mechanisms of fatigue crack nucleation that more precisely defines the conditions of material susceptibility, mechanical loading, and environment that are needed to nucleate cracks. During the first two years of a five-year investigation, we considered the possibility that aggressive environments might accelerate the crack nucleation process by three mechanisms: (1) local increase in stress resulting from pitting, (2) local material embrittlement possibly by hydrogen, and (3) local increase in the aggressiveness of the environment possibly from acidification within pits. In fact, conditions necessary to nucleate cracks might result from some change involving all three of these processes.

This is illustrated in figure 1, where the conditions for fatigue crack formation are depicted as a surface in three-dimensional space defined by axes of local stress, local material susceptibility, and local environment severity. The figure depicts a point in space representing initial conditions where crack nucleation does not occur. As conditions change over time, the local conditions could follow a wide range of trajectories that represent different combinations of change in the local stress, material susceptibility, and environment.

Most models of corrosion-fatigue crack nucleation¹⁻⁵ focus on the changes in local stress that result from pitting. This is equivalent to following a trajectory of increasing local stress that parallels the local stress axis in figure 1. In such models, a critical condition is assumed to occur when the stress intensity produced by the pit is of a sufficient magnitude for cracks to nucleate. The inherent assumption in this approach is that conditions of material susceptibility and environment do not change over time. This assumption might be unrealistic. However, a more comprehensive understanding is needed if a range of interactions between environment, stress, and material susceptibility are to be considered. Such analyses have been attempted and, at least in one case,³ a quantitative description of how the critical pit size is affected by the environment has been proposed.

In the present program of research, we continue to pursue such efforts with specific application to corrosion fatigue nucleation in commercial aircraft skin. Ultimately, we expect that the results of our program, combined with the efforts of other participants in the NAARP, will lead to more accurate predictions and additional opportunities to mitigate corrosion-fatigue cracking in aircraft skin.



CAM-5082-7

Figure 1. Critical conditions for corrosion-fatigue crack nucleation.

Section 2

OBJECTIVES AND APPROACH

The goal of this research program is to characterize and quantitatively describe the early stages of corrosion fatigue in the fuselage skin of commercial aircraft. Specific objectives are to gain an improved deterministic understanding of the transition from corrosion pit to short crack to long crack and to delineate the effects of environment, clad and paint, and loading conditions on crack nucleation and propagation rates.

The technical approach for achieving these objectives is to apply appropriate diagnostic techniques to the geometric and chemical characterization of corrosion-damaged regions in aluminum alloys that lead to corrosion fatigue cracks. The application of these diagnostic techniques focuses on corrosion fatigue damage produced in laboratory experiments performed on fuselage skin specimens obtained from a retired Boeing 737 aircraft.

During the first two years of this study, we developed an experimental technique to produce corrosion fatigue cracks in the laboratory in a manner that would allow us to examine the crack nucleation and growth kinetics in both a statistical and deterministic manner. A range of environments, material conditions, and loading conditions were investigated experimentally in an effort to assess their effect on the crack nucleation and growth rate.

We selected experimental conditions relevant to conditions in service without necessarily simulating them. Our intention was to conduct corrosion-fatigue tests that would yield results that would clarify the underlying mechanisms. Additional experimental and analytical work is necessary to translate a new or more comprehensive understanding of the early stages of damage into improved life prediction capability and new opportunities to mitigate corrosion fatigue in aircraft skin.

Section 3

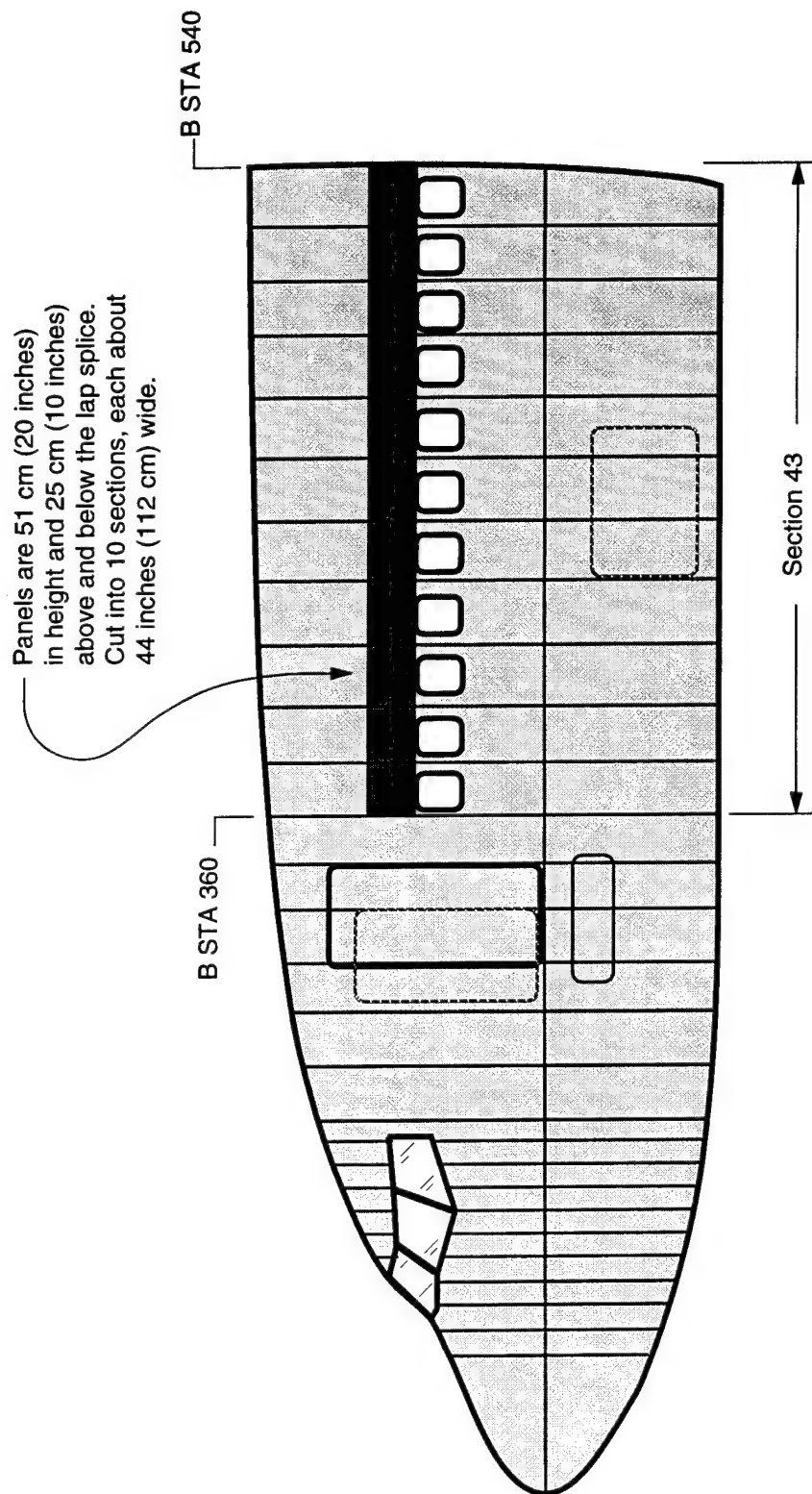
EXPERIMENTAL PROCEDURE

3.1 TEST MATERIAL.

We obtained the test specimen material examined in this investigation from sections of fuselage skin from a retired Boeing 737 aircraft. The aircraft, line number 176, entered service in 1968, experienced 56,228 flight hours, and was retired in February 1992. Material was obtained in the form of 10 equal-sized sections taken from above and below the 10-L and 10-R lap joints (above the windows) between body stations 360 and 540 (i.e., aft of the forward door to a location roughly in line with the leading edge of the wing). The location of the five sections taken from the left side of the aircraft is shown in figure 2. One of the ten body sections is shown in figure 3.

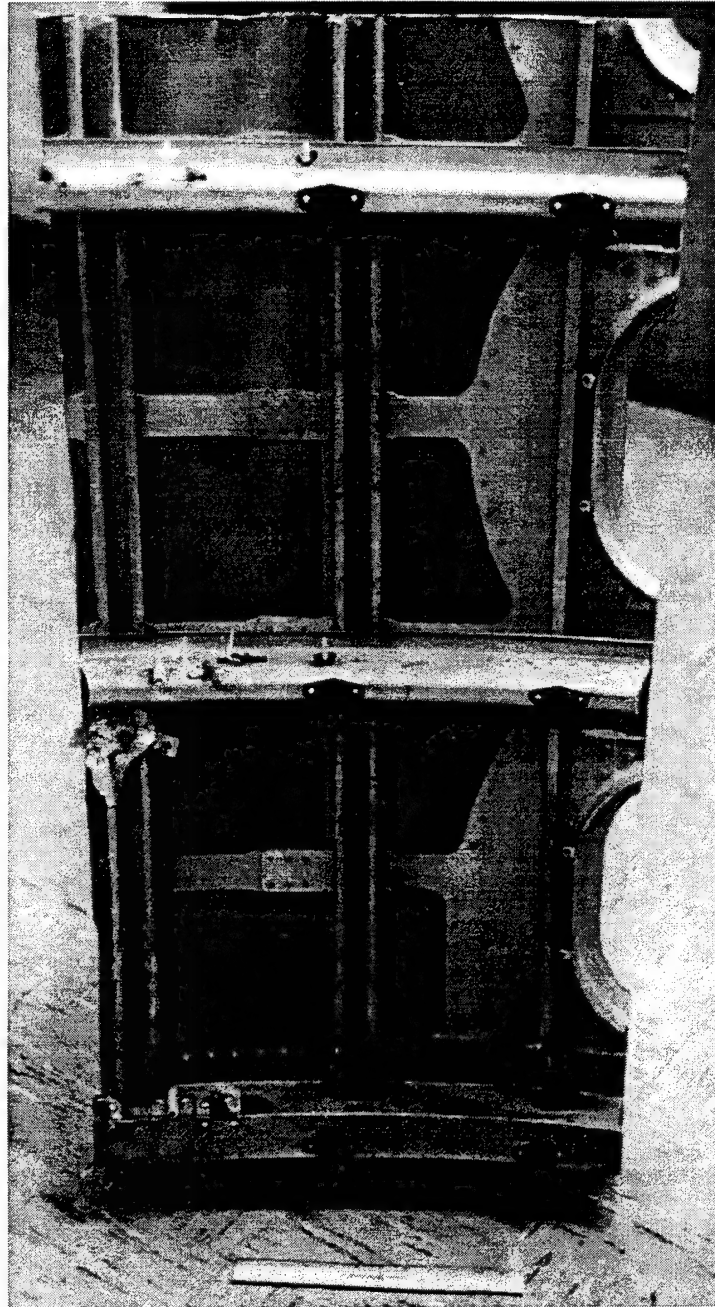
The aircraft was constructed with the early design lap joints that were cold bonded (later Boeing 737 aircraft were constructed with a hot bonding process). The aircraft had undergone extensive retrofitting of the top row of lap joint rivets to impede fatigue cracking (so-called terminating action), as mandated by Airworthiness Directive AD90-06-02, April 17, 1990. A history of the painting maintenance was not available; however, the paint on the exterior surface and the zinc chromate primer on the interior surface were generally in good condition. The skin consisted of a 0.81-mm (0.032-in.)-thick core of 2024-T3, Alclad layers on both sides that were about 0.06 mm (0.002 in.) thick, a paint layer on the outer surface about 0.08 mm (0.003 in.) thick, and a corrosion inhibitor layer on the inside that was about 0.10 mm (0.004 in.) thick (see figure 4). The 2024-T3 alloy and the Alclad (1230 alloy) had nominal weight percentage compositions of Al-4.5, Cu-0.6, Mn-1.5, Mg and Al-0.1, Cu(max)-0.05, Mn(max)-0.70, Si+Fe(max), respectively.

Metallographic examination of the 2024-T3 core material revealed a microstructure with constituent particles that were distributed with only moderate directionality (see figure 5). The grain structure, revealed by etching with Keller's reagent, was equiaxed in the in-plane orientation with a mean linear intercept distance of 30 μm (see figure 6). The through-thickness orientations were similar in appearance and consisted of moderately elongated grains with a mean linear intercept distance of 15 μm in the through-thickness direction. The Alclad grain structure, as shown in figure 7, contained few constituent particles and had an equiaxed grain structure when viewed normal to the



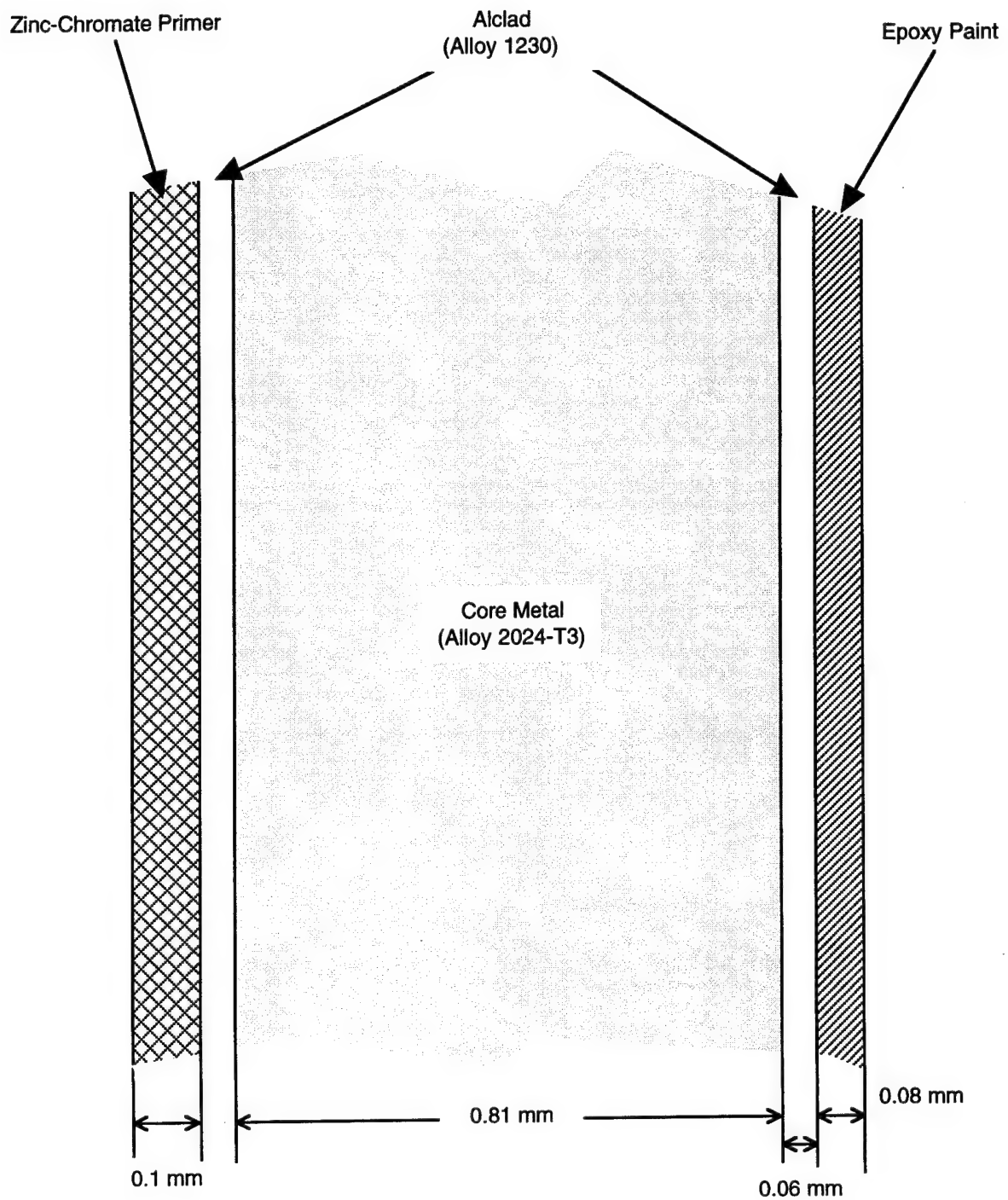
CM-5082-6

Figure 2. Location of panels obtained from retired Boeing 737 aircraft.



CP-5082-8

Figure 3. Section of recovered Boeing 737 fuselage.



CAM-5082-9

Figure 4. Cross section of Boeing 737 aircraft skin.

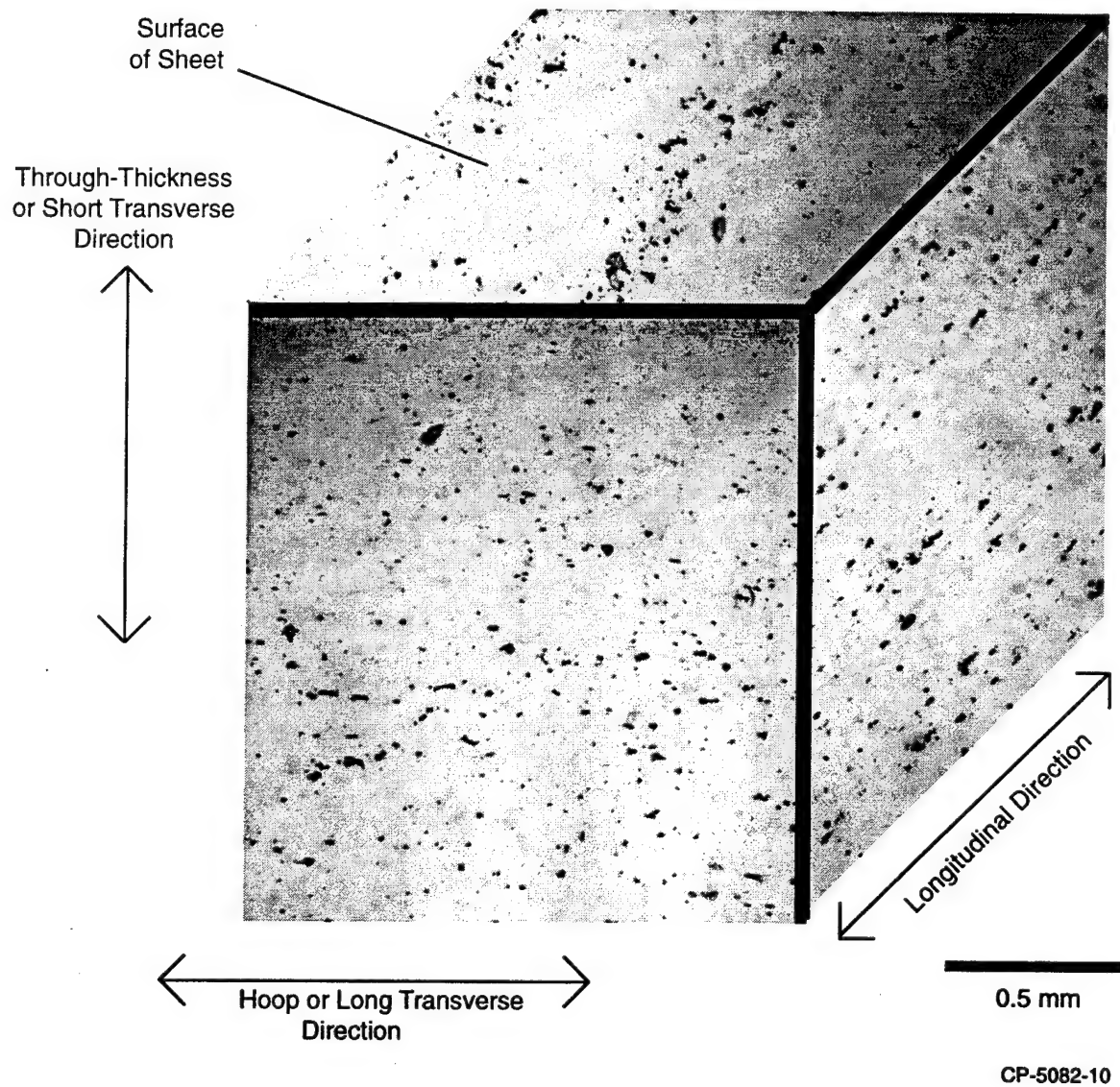
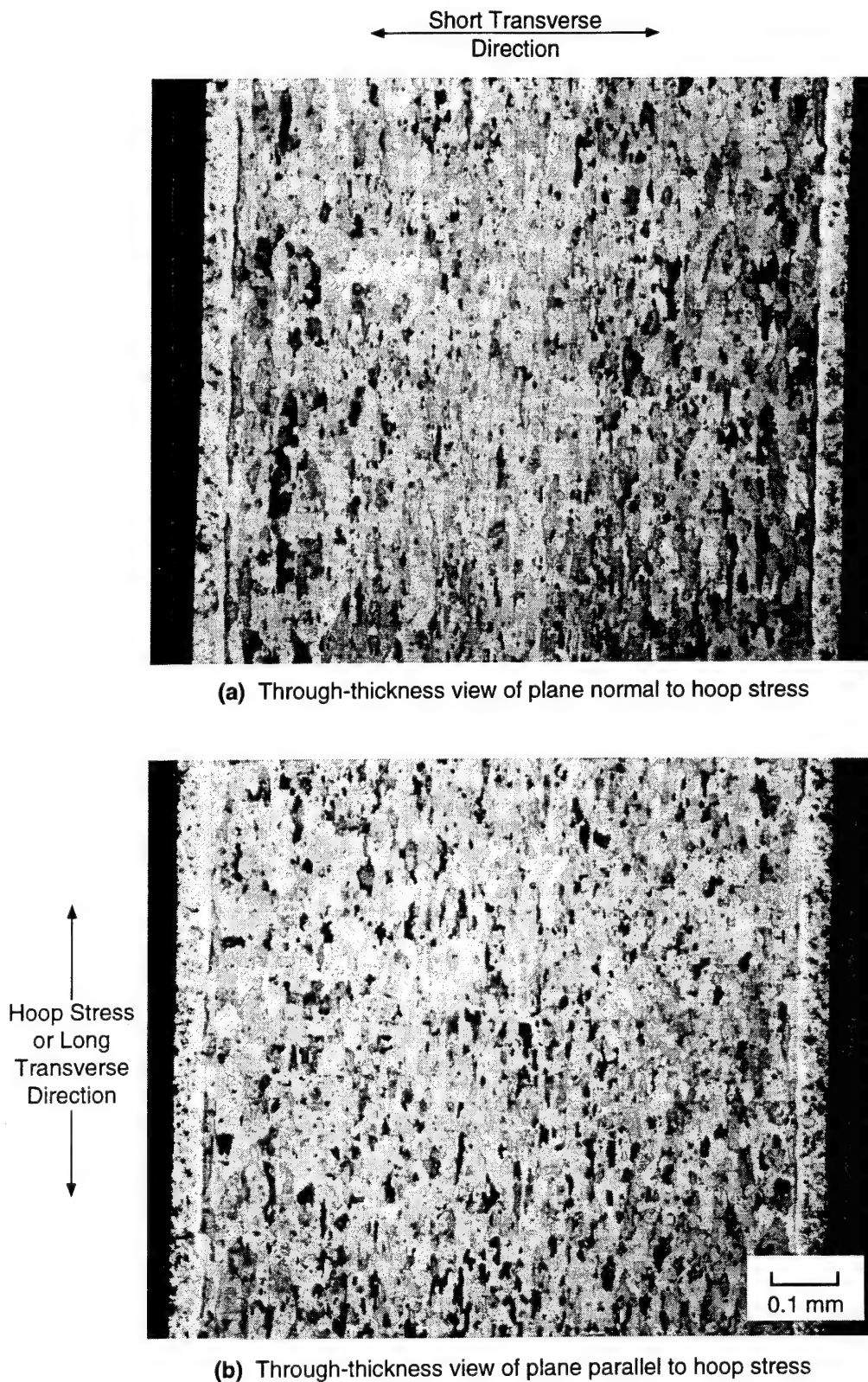
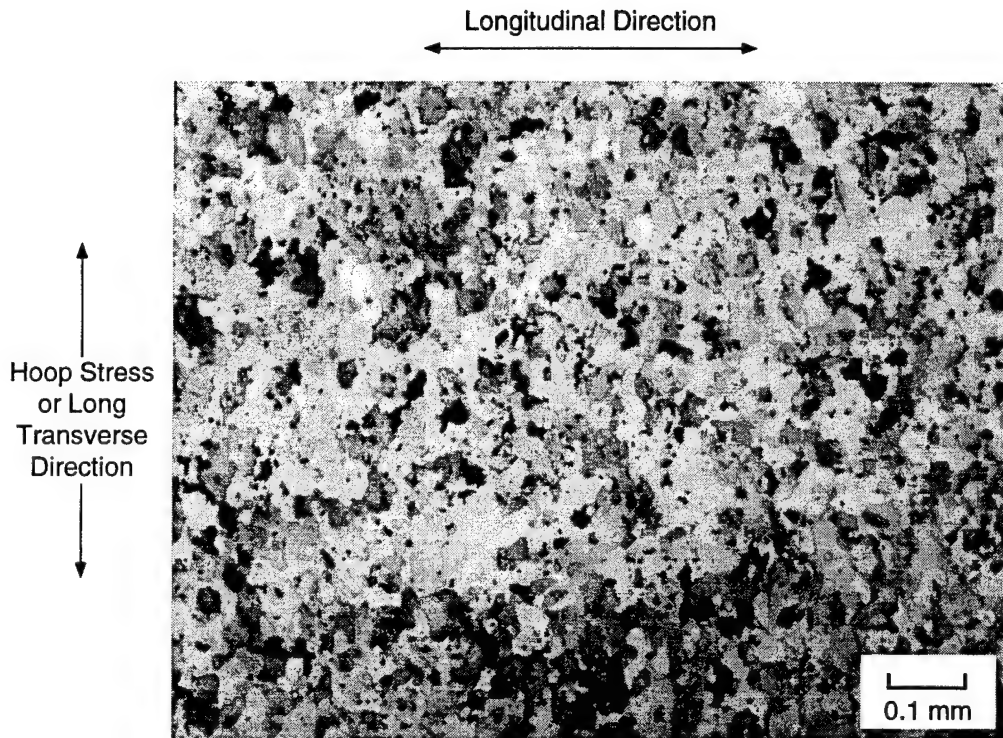


Figure 5. Unetched metallographic cross sections of skin material from a retired Boeing 737 aircraft showing the distribution of constituent particles.



CP-5082-11

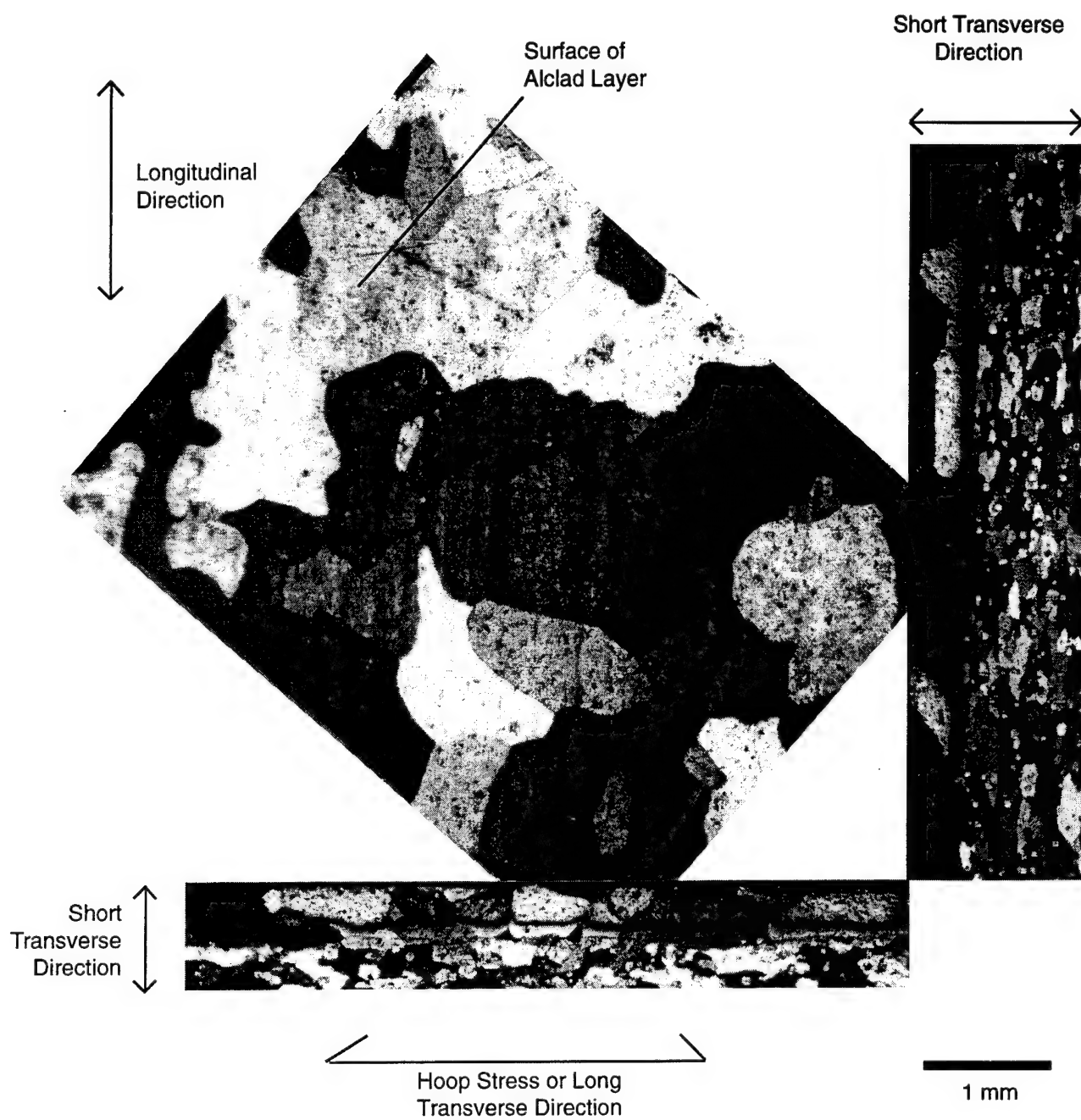
Figure 6. Etched metallographs cross sections of skin material from a retired Boeing 737 aircraft showing grain structure.



(c) In plane view of core material

CP-5082-12

Figure 6. Etched metallographs cross sections of skin material from a retired Boeing 737 aircraft showing grain structure (Concluded).



CP-5082-13

Figure 7. Anodized metallographic cross sections of skin material from a retired Boeing 737 aircraft showing the grain structure of the Alclad.

plane of the sheet with a mean linear intercept distance of 550 μm . In the through-thickness directions, the grains frequently encompassed the entire thickness of the clad, about 70 μm .

The Alclad layer was substantially softer than the 2024-T3 core. Microhardness tests revealed that the core and the Alclad had Vickers' hardnesses of 120.4 ± 1.5 and 32.2 ± 2.3 kg/mm^2 , respectively.

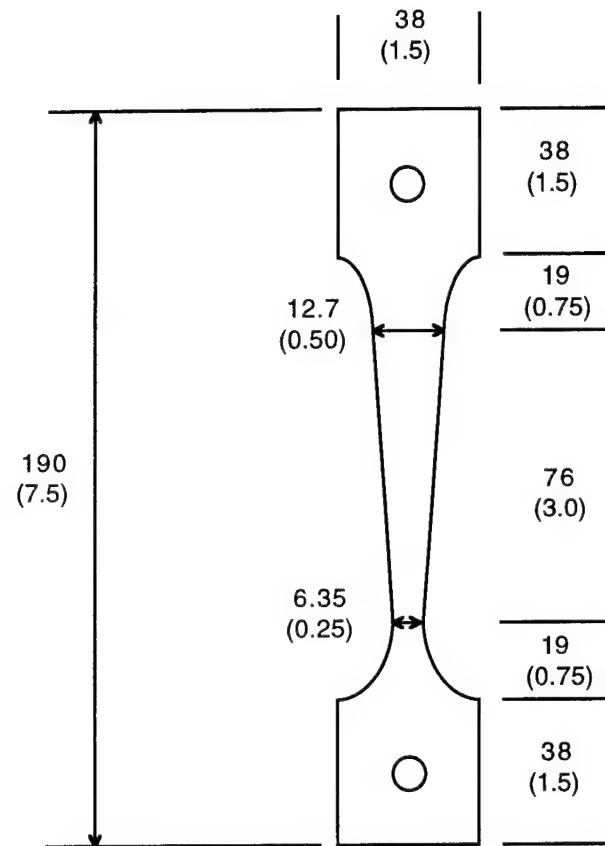
3.2 SPECIMEN FABRICATION.

Tapered, corrosion-fatigue specimens, such as the one shown in figure 8, were obtained from regions of the skin that were free of rivet holes and doublers. The specimens were extracted from the panel in the vertical and horizontal orientations (i.e., with the longitudinal axis of the specimens perpendicular or parallel to the lap splice, respectively). Specimens were tested in three conditions: with the clad and paint intact (the as received condition), with the paint chemically removed (the clad only condition), and with the paint and clad ground off (the bare condition). Paint was removed from the clad only specimens with Turco 5351 Thin by immersion for 6 to 12 hours followed by a water rinse. The bare specimens were prepared by surface grinding to remove the paint and the Alclad layer.

The through-thickness surfaces of the specimens were left with as-machined, 30- μm , 5- μm , or 0.05- μm finishes. The 30- μm finish was produced by polishing with Struers 500 grit SiC paper. The SiC paper was wrapped around a glass mandrel and was translated longitudinally along the through-thickness surfaces of the specimen gage section. The 5- μm finish was produced by final polishing with 4000 grit SiC paper, and the 0.05- μm finish was produced by final polishing with 0.05 μm Al_2O_3 powder in water. Figure 9 shows photomicrographs of the surface finish. Figure 10 shows quantitative topographic measurements made with a scanning laser microscope. Based on these measurements, the standard deviation about the mean surface elevation for the as-machined, 30- μm , 5- μm , and 0.05- μm finishes was 3.4, 0.8, 0.3, and 0.2 μm , respectively.

3.3 STRESS CALCULATION.

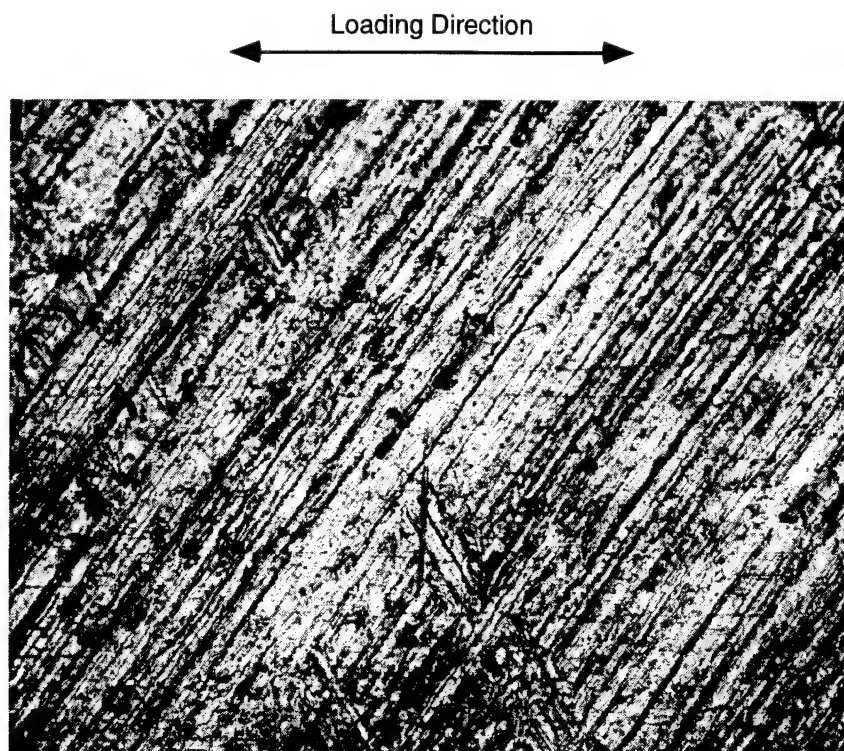
To compare the corrosion fatigue test results from the as received, clad, and bare skin materials, the stress values used for the corrosion fatigue tests were based on the measured yield stress values for each material and are expressed in terms of the yield normalized stress, σ/σ_y . In this way, the load supported by the paint layers and the clad, when present, are excluded and the stress values reflect the stress in the 2024-T3 core material.



Dimensions in mm (inches)

CAM-5082-14

Figure 8. Tapered corrosion-fatigue specimen.



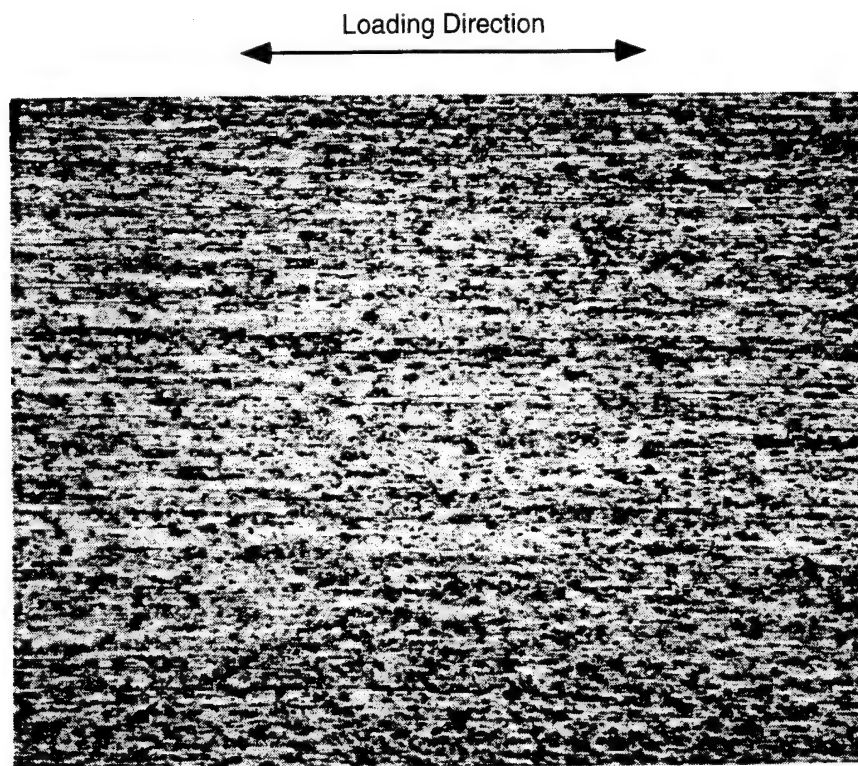
(a) As-machined finish



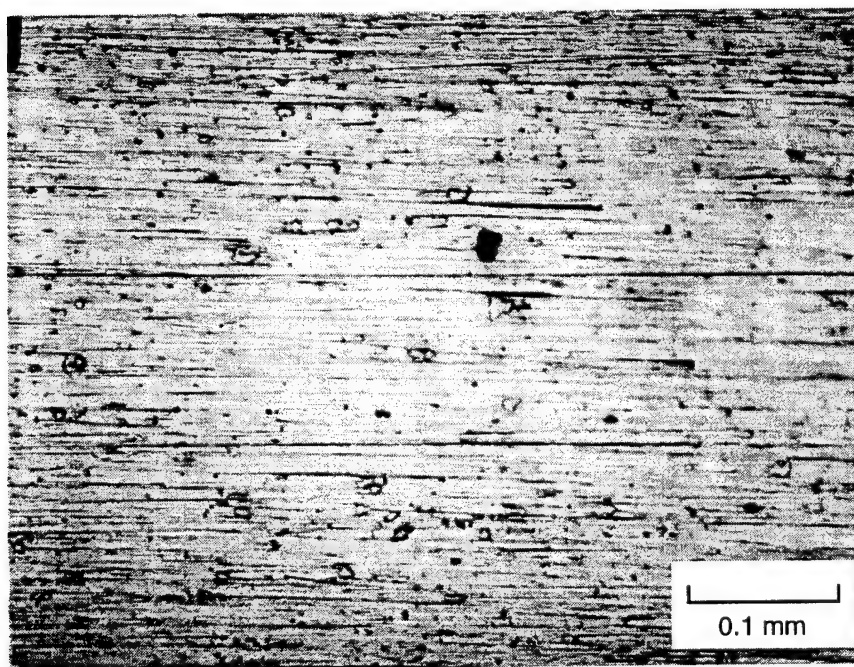
(b) 30- μ m finish

CP-5082-15

Figure 9. Photomicrographs showing the roughness of the through-thickness surface of untested corrosion-fatigue specimens.



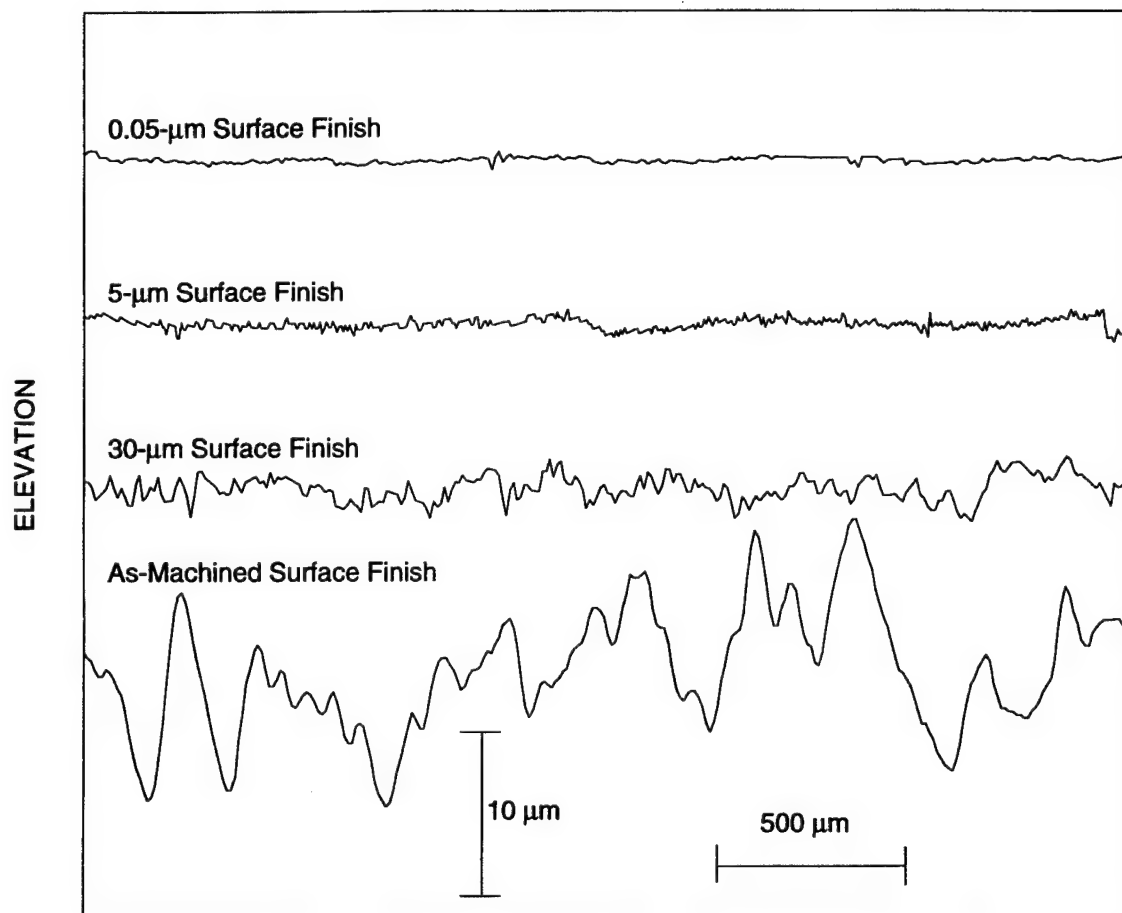
(c) 5- μ m finish



(d) 0.05- μ m finish

CP-5082-16

Figure 9. Photomicrographs showing the roughness of the through-thickness surface of untested corrosion-fatigue specimens (Concluded).



CAM-5082-17

Figure 10. Surface roughness profiles from tapered tensile fatigue specimens.

Figure 11 compares the load-displacement behavior for the as received and clad materials and expresses the load on a per unit specimen width basis, F/w . The value of the load at the yield point, F_y/w , for the as received and clad materials is 1060 N/cm (1856 lbs/in.) and 1040 N/cm (1822 lbs/in.), respectively. Based on these results, we established the following method to compute normalized stress values for the as received and clad specimens by assuming that the thickness of each type of specimen is constant and that the width varies.

$$\left(\frac{\sigma}{\sigma_y} \right)_{\text{as received}} = \frac{F}{1060 \text{ (N/cm)} * w} = \frac{F}{1856 \text{ (lbs./in.)} * w} \quad (1)$$

$$\left(\frac{\sigma}{\sigma_y} \right)_{\text{clad}} = \frac{F}{1040 \text{ (N/cm)} * w} = \frac{F}{1822 \text{ (lbs./in.)} * w} \quad (2)$$

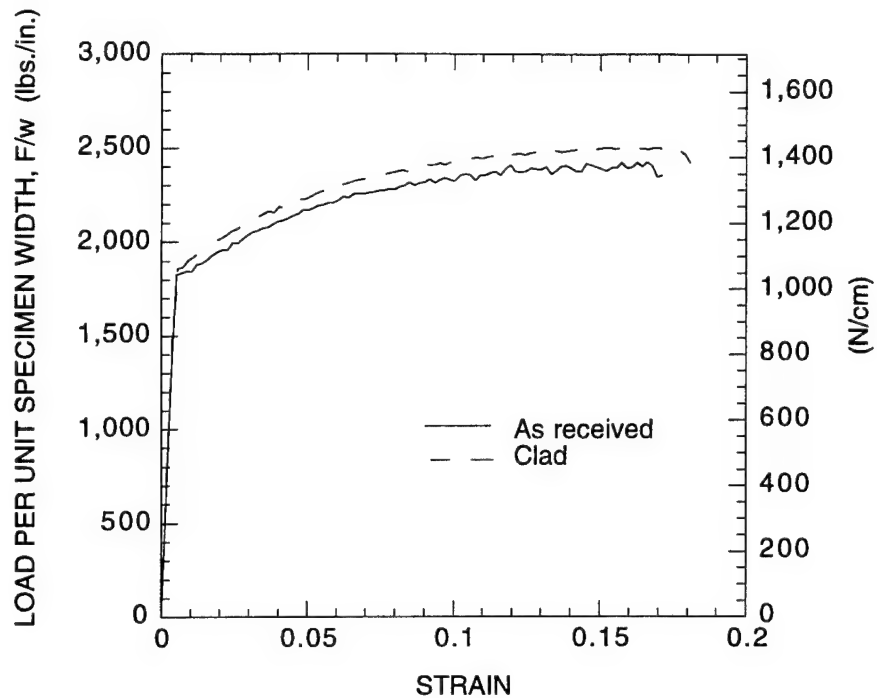
The average yield strength for the core material (2024-T3) was determined from replicate tensile tests, as shown in figure 12, and was found to be 368 MPa (53.4 ksi). The thickness, t , of the specimens obtained from bare material varied because of variations in the grinding procedure that removed the paint and clad layers. Thus, for specimens made from bare material, the normalized stress was computed as follows.

$$\left(\frac{\sigma}{\sigma_y} \right)_{\text{bare}} = \frac{F}{368 \text{ (MPa)} * w * t} = \frac{F}{53.4 \text{ (ksi)} * w * t} \quad (3)$$

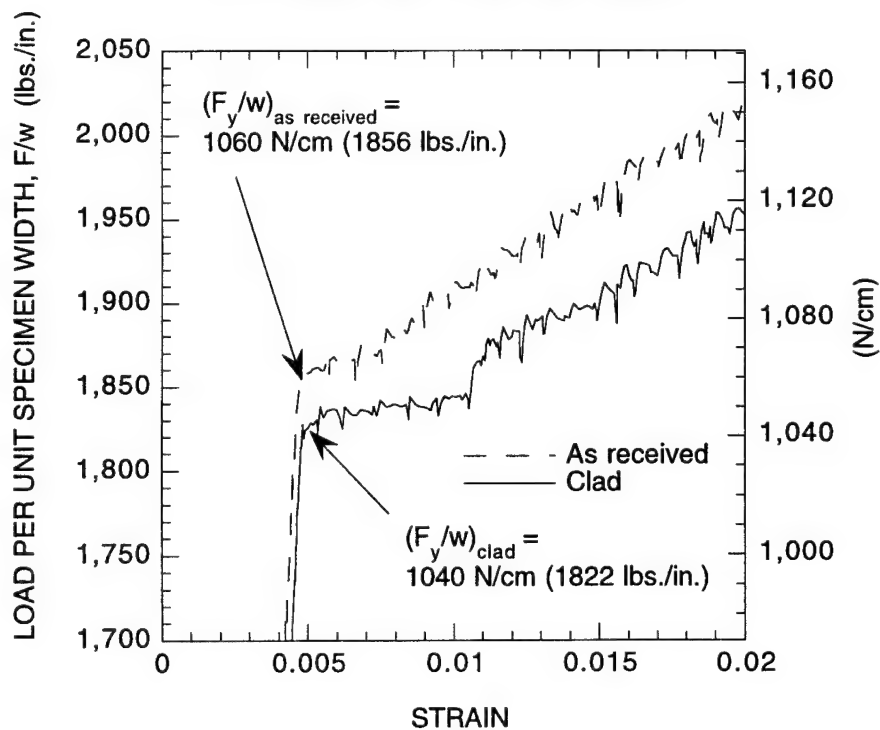
The stress as a function of location on the specimen taper was computed as follows.

$$\frac{\sigma(x=x)}{\sigma_y} = \frac{\sigma(x=0)}{\sigma_y} \left[1 - \frac{x}{L} \left\{ 1 - \frac{w(x=0)}{w(x=L)} \right\} \right] \quad (4)$$

where $\sigma(x=x)$ and $\sigma(x=0)$ are the stresses at position $x=x$ and at the minimum specimen width ($x=0$), respectively; x is the distance from the minimum specimen width; L is the tapered gage length; and $w(x=0)$ and $w(x=L)$ are the minimum and maximum specimen widths.



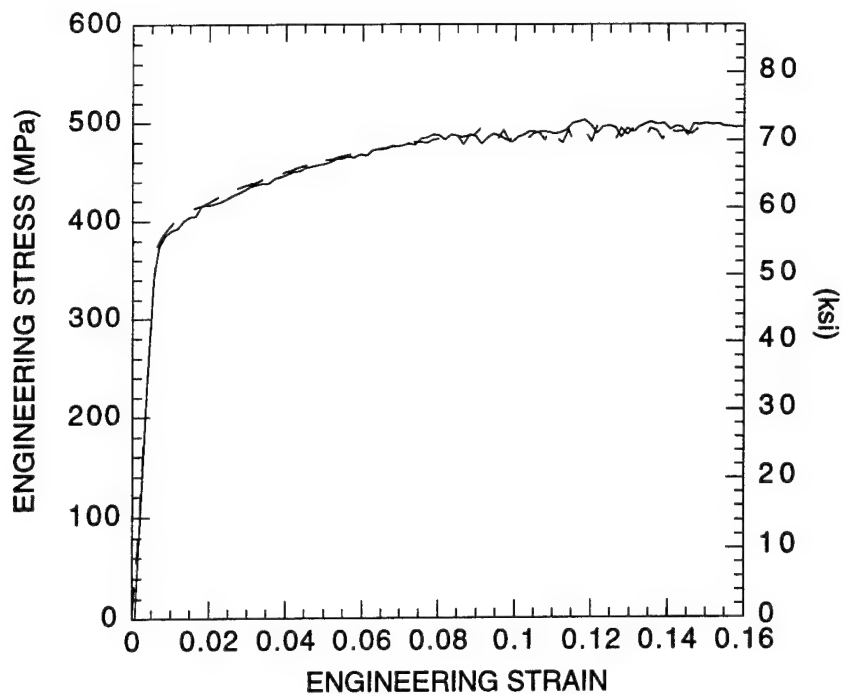
(a) Full-scale view of load-strain behavior.



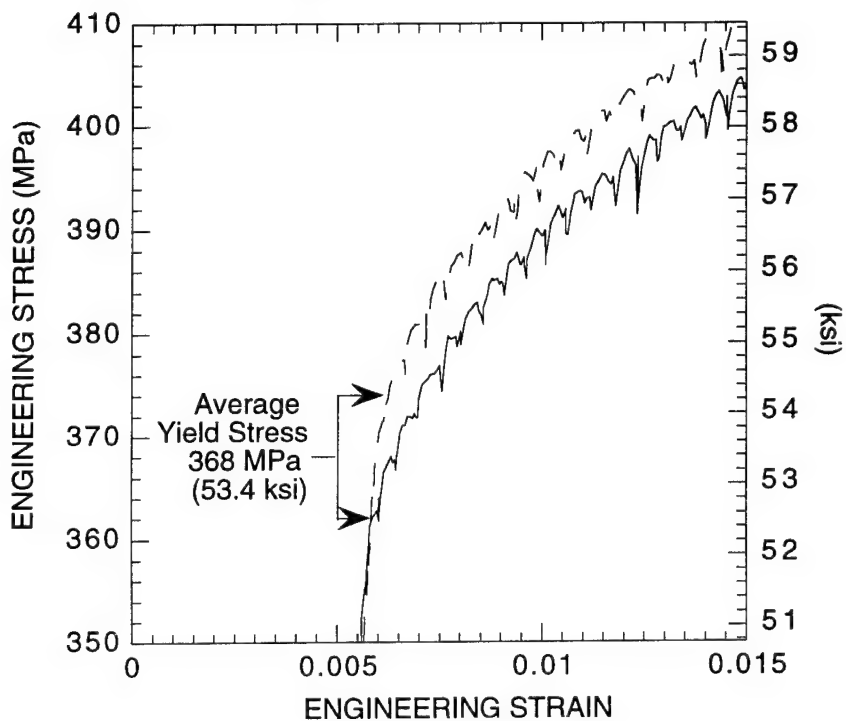
(b) Expanded scale view showing yield behavior

CAM-5082-18

Figure 11. Load-strain behavior for as-received and clad-only Boeing 737 skin material specimens.



(a) Full-scale view showing yield behavior from replicate tests.



(b) Expanded-scale view showing yield behavior from replicate tests.

CAM-5082-19

Figure 12. Stress-strain behavior for Boeing 737 skin material with paint and clad removed (bare material)

3.4 CORROSION-FATIGUE TESTING AND DATA ANALYSIS.

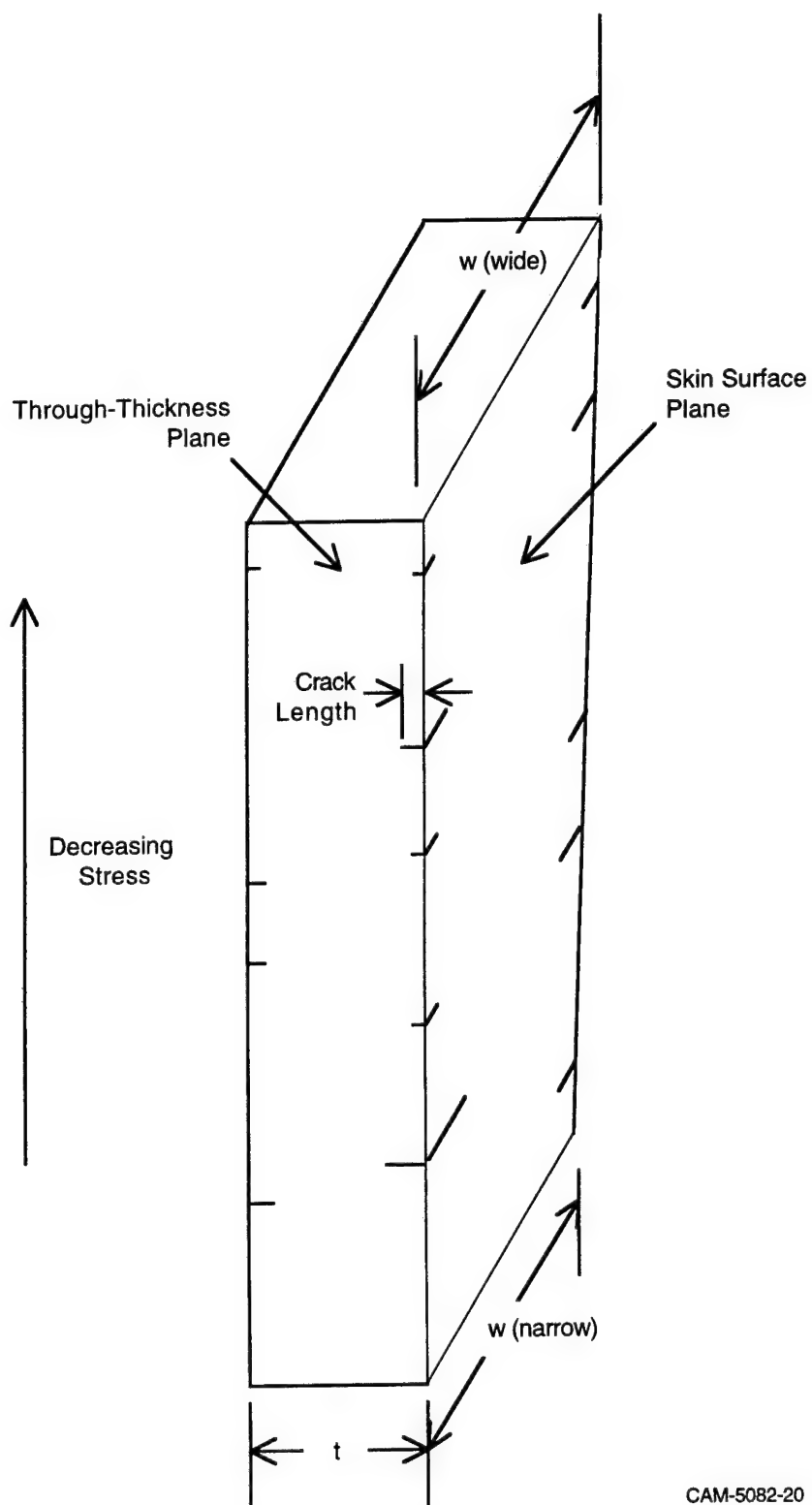
Corrosion-fatigue testing was conducted in a stagnant, 0.5 M NaCl, aerated solution. Specimens were pretreated by soaking in the test solution for three days before the mechanical loading. The pH values were adjusted by the addition of HCl or NaOH. The fatigue tests were conducted at 5 Hz with a sinusoidal waveform and an R value ($= \sigma_{\min}/\sigma_{\max}$) of 0.1.

After fatigue testing, the through-thickness surfaces of the tapered gage section were examined for evidence of pitting damage and cracking. Corrosion deposits were removed with a solution consisting of 17.5 mL H_3PO_4 , 5 g CrO_3 , and 1000 mL of deionized water at 50° to 60°C. The specimens were immersed for approximately 10 minutes and then rinsed in water. The air time between leaving the solution and entering the water was as short as possible (about 1 second) to prevent a film from forming on the surfaces. If a film appeared to be present, it was removed with a 1-minute dip in HNO_3 .

After removal of the corrosion deposits, the specimen gage lengths were examined in a scanning electron microscope (SEM). Cracks in the edges of the specimens, from the minimum width of the gage length (or fracture surface, if the specimen was loaded to final failure) and along the gage length taper, were counted by inspection of images on the SEM screen at a magnification of about 1000X. Figure 13* is a schematic of the relative position of the cracks. Cracks as small as 5 μm could be readily counted by this procedure for the 30- μm , 5- μm , and 0.05- μm finishes. Specimens with as-machined surfaces required larger cracks before they could be consistently resolved. As a consequence, specimens tested in the as-machined condition were not included in the crack propagation rate analysis.

Crack growth rate during the early stages of crack growth was obtained by measuring the length and location of cracks along the gage length. In most cases, the crack population at any region of the gage length consisted of crack lengths ranging from the detection limit (about 5 μm) to a maximum crack length. A fairly clear trend was observed; longer cracks were observed in the higher stressed regions of the gage length. In our crack growth rate analysis, it was necessary to assume that all cracks had nucleated and begun to grow at the start of the fatigue loading phase of each test. To reduce the effect of cracks that nucleated later in the test, we eliminated from

*Figure 13 also illustrates the meaning of the terminology used in this report regarding the orientation of the exposed surfaces on corrosion-fatigue test specimens. The "through-thickness" planes are exposed cross sections of the skin material that include regions of the 2024-T3 core material, the Alclad Layers, and the interior and exterior paint layers, as shown in figure 4. The "skin surface" planes are the interior or exterior surfaces of the fuselage skin.



CAM-5082-20

Figure 13. Distribution of cracks on tapered gage section.

consideration all but the four longest cracks in each 50- μm longitudinal section of the gage section. Data shown in appendix A have been censored in this manner.

In describing the crack growth rate, Paris Equation behavior is assumed as follows:

$$\frac{da}{dN} = C (\Delta K)^m \quad (5)$$

where a is the crack length, N is the number of cycles, K is the stress intensity, and C and m are constants. Newman and Raju⁶ computed a relationship describing K for a circular corner crack with the crack plane normal to both surfaces as follows:

$$K = 0.722 \sigma \sqrt{\pi a} \quad (6)$$

Eliminating K from equations 5 and 6 and integrating from an initial crack length, a_0 , results in the following when m is assumed to be 2:

$$a = a_0 \exp[(0.722 \Delta\sigma)^2 C N \pi] \quad (7)$$

We set m equal to 2 because (1) results from other investigations of similar data⁷ exhibited this value, (2) early analyses of the present data where the value of m was allowed to vary resulted in values close to 2, and (3) fixing the value of m at 2 made the analysis more computationally expedient. To obtain a measure of the crack growth rate from the distribution of crack lengths measured on a tapered specimen gage section, we performed a least squares analysis on equation 7 using Kaleidagraph 3.0.⁸ The results of the least squares analyses are plotted as the solid line fit to the data in the appendix.

3.5 METALLOGRAPHIC PREPARATION.

Aluminum samples were mechanically polished with SiC papers and, in the final stages, with 0.05 μm Al_2O_3 polishing powder. Etched microstructures were produced with a solution consisting of 10 ml H_3PO_4 and 90 ml H_2O . Dark field images showing the microstructure of the Alclad layer were produced by anodizing a mechanically polished surface with a solution consisting of 2000 mL of water, 92 mL of 50% fluoroboric acid (HBF_4), and 14 g of boric acid (HBO_3). Anodizing was performed with a Buehler Electromet 4, at a potential of 20 V, under a current of < 2 amps, and at an anode-to-cathode distance of about 25 mm. The current was applied for about 2 minutes.

Section 4

EXPERIMENTAL RESULTS AND DISCUSSION

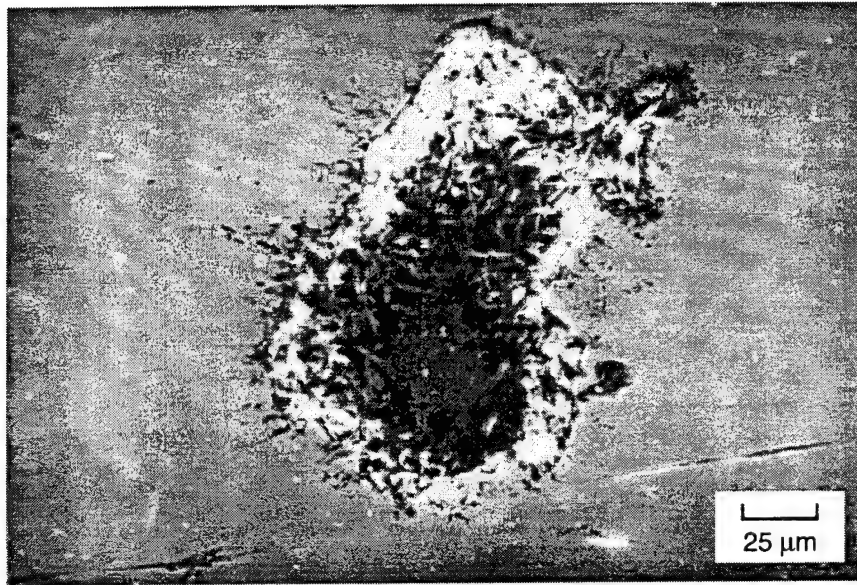
4.1 PITTING CHARACTERISTICS.

We undertook a qualitative characterization of the effect of experimental variables on localized corrosion appearance because of the role pitting often plays in the nucleation of fatigue cracking. We examined the effects of cladding and coatings, pH, material orientation, and surface roughness. The results of our observations are presented in terms of each of these experimental variables.

The material obtained from the retired aircraft had sustained pitting damage on the exterior surface during service. The skin surface exposed to the interior of the aircraft was free of pitting damage. The pits on the exterior surface were observed when the paint on the outer surface was carefully removed by light abrasion with SiC paper (see figure 14). The pits appeared to be flat bottomed and were usually filled with paint or primer, which suggests that the pits were present prior to the application of the last coat of paint. Occasionally, the pits that formed during service (identifiable from the presence of the paint on the fracture surface) would serve as nucleation sites for corrosion-fatigue cracking in the experiments performed with tapered test specimens (see figure 15). The appearance of the pit on the fracture surface indicates that pitting penetration was limited to the depth of the clad as is commonly observed for Alclad protected aluminum alloys.⁹

Pitting behavior along exposed edges of skin material was examined for as received, clad, and bare material. The appearance of pitting damage varied for each nominal material condition; however, we observed generally consistent trends as follows:

- Bare material exhibited two forms of localized corrosion damage: deep pits, apparently a consequence of corrosion at constituent particles, and intergranular cracking. Figure 16 shows typical areas of these two forms of damage. Deep pitting damage is generally associated with accelerated local corrosion of constituent particles that are anodic to the matrix or accelerated local corrosion of the region around constituent particles where the particles are cathodic to the matrix.⁵ Intergranular cracking in 2XXX-series alloys is often a result of copper depleted zones on either side of grain boundaries.¹⁰
- Clad and painted material exhibited crystallographic pit colonies on exposed clad surfaces, as shown in figure 17. Individual pits within the colonies appeared as square, block-shaped depressions approximately 5 μm on a side.



CP-5082-21

Figure 14. Pit on outer surface of skin from Boeing 737 aircraft.

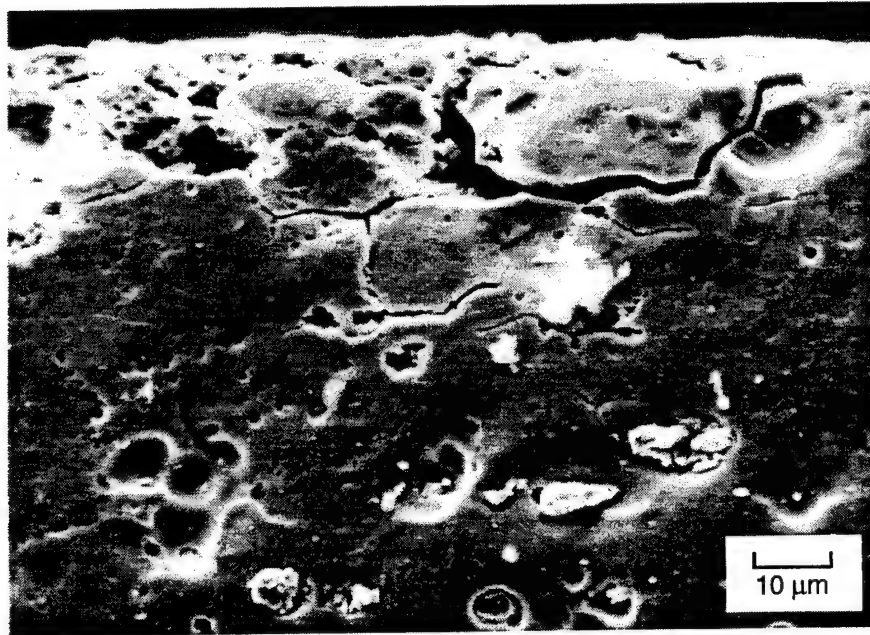
White material is paint residue in pits
in the Alclad layer



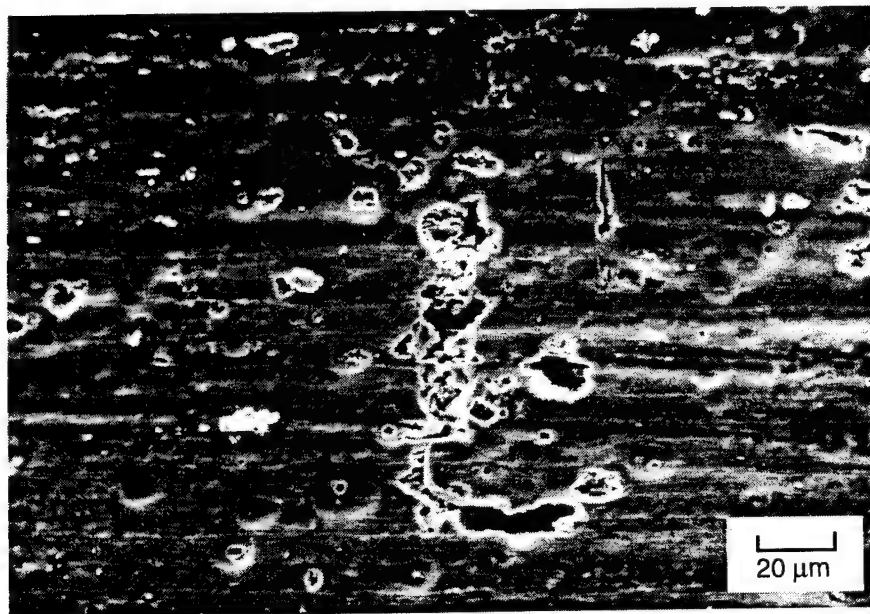
CP-5082-22

Figure 15. Corrosion-fatigue crack nucleation from pre-existing pits in the Alclad layer of Boeing 737 skin material.

Corrosion-fatigue cracking was induced in the laboratory after a 4-day exposure to 0.5 M NaCl solution at pH 10.



(a) Intergranular attack near edge of a through-thickness plane of Specimen 27

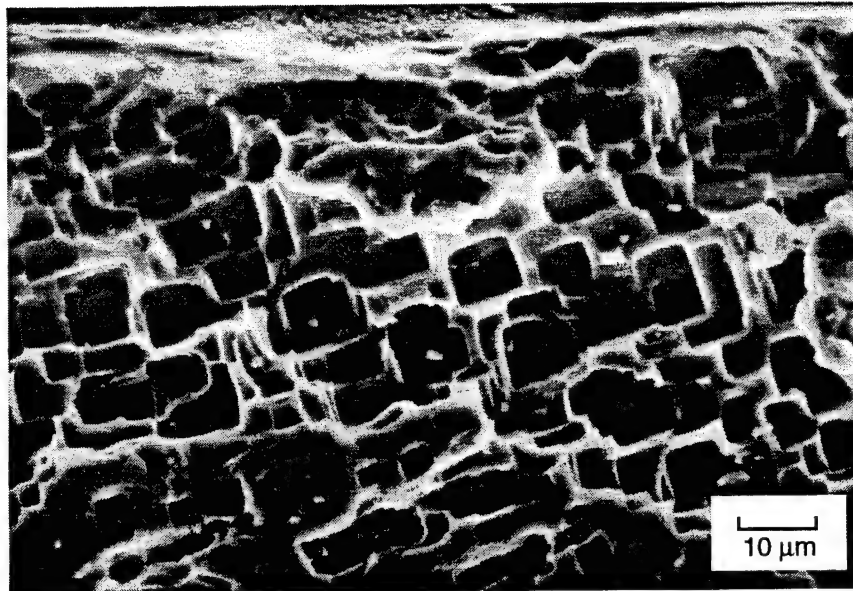


(b) Pitting at constituent particle on through-thickness plane of Specimen 26

CP-5082-23

Figure 16. Typical corrosion damage on bare specimens (clad and coatings removed) of aircraft skin material.

Corrosion damage is a result of a 4-day exposure to 0.5 M NaCl solution at pH 6.



CP-5082-24

Figure 17. Crystallographic pits on a through-thickness plane of the Alclad layer of a corrosion-fatigue specimen in the as-received condition (Specimen 2).

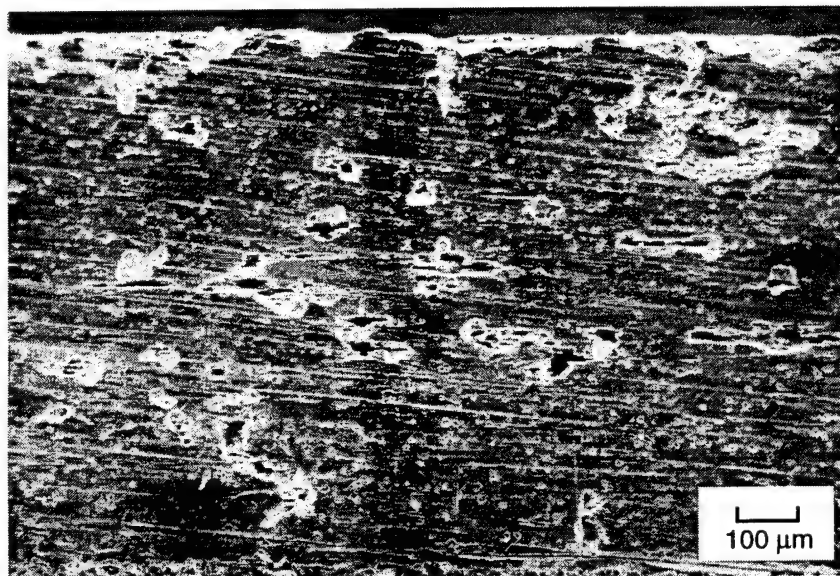
Corrosion damage is a result of a 4-day exposure to 0.5 M NaCl solution of pH 6.

The pit colonies were usually found on the through-thickness surfaces near the corners of the corrosion fatigue specimens and were present at all pH levels tested. Crystallographic pits are often associated with anodic corrosion and are observed in pure aluminum after exposure to salt water solutions where the potential is slightly above the pitting potential.¹¹ The crystallographic character of the pits is attributed to an optimal shape for maintenance of the pit environment and current density.¹²

- After exposure to the pH 2 environment, clad and as received material exhibited deep pits that appeared to nucleate at constituent particles (see figure 18). These pits were similar in appearance to those observed on bare specimens.
- Painted and clad specimens often exhibited more corrosion in the core material than did the clad specimens in the pH 6 and pH 10 solutions, but not in pH 2 solutions. This is a reversal of expected behavior wherein the clad is anodic to the core and, therefore, corrodes more rapidly. The difference in corrosion rate was made evident by the abrupt step in elevation at the clad/core interface, as shown in figure 19. The observation that the exposed surface of the core alloy has corroded more extensively (i.e., is lower than the clad in figure 19) was confirmed by stereo photography.

The reason for the higher corrosion rate of the core material on the corrosion fatigue specimens is uncertain. The catchment area principle (i.e., the direct proportionality between cathode area and galvanic corrosion rate) might explain why the Alclad (anode) is effective in preventing corrosion of the core material (cathode) in situations where the core is only exposed to the environment through small pits or scratches that penetrate the Alclad (i.e., when a small cathode-to-anode ratio prevails). However, it does not explain how a reversal in the relative corrosion rates can occur when the anode-to-cathode ratio is much smaller, as is the case when a through-thickness plane is exposed.

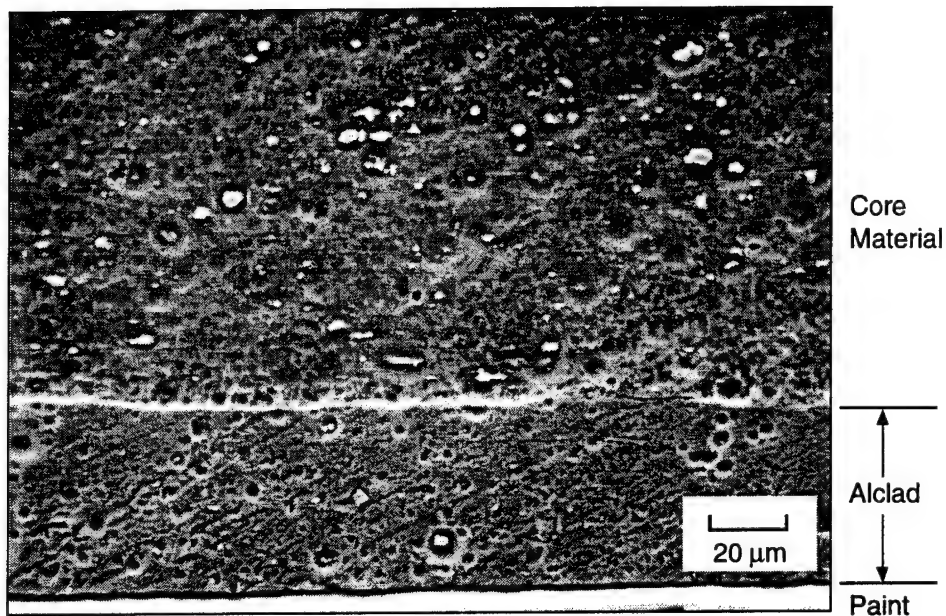
Reversals in the expected rates of corrosion of galvanic couples have been observed in other systems. The most relevant work to the present case involves galvanic couples of magnesium and aluminum. Bothwell,^{14,15} in the corrosion compendium edited by Shreir,¹³ states that when magnesium is coupled to aluminum in sea water, a high local pH develops at the aluminum cathode, which greatly enhances cathodic corrosion. Bothwell goes on to state that experience with Mg alloy/Al alloy couples has shown that cathodic attack can be almost as severe as anodic attack. This suggests that, in the present experiments conducted in solutions with pH 6 or higher, the pH at the surface of the core material (the cathode) increases enough to dissolve the surface oxide (i.e., it achieves a level above about pH 11¹⁶). The alkalinity of the solution at the cathode in the tests conducted in pH 2 solutions appears to be not high enough to induce substantial cathodic corrosion.



CP-5082-25

Figure 18. Pitting damage on a through-thickness plane of a corrosion-fatigue specimen in the as-received condition (Specimen 41).

Corrosion damage is a result of a 4-day exposure to 0.5 M NaCl solution of pH 2.



CP-5082-26

Figure 19. Corrosion damage on a through-thickness plane of as-received skin material after a 4-day exposure to pH 10 salt solution.

The Alclad material exhibited less corrosion attack than the core material. This is indicated by a downward step across the boundary from the Alclad to the core material. The direction of this step was confirmed by stereophotographic analysis (not shown).

4.2 CORROSION-FATIGUE TESTS.

We examined the effects of a wide range of environmental and material variables on the early stages of corrosion fatigue in an effort to identify the dominant physical processes. Clearly, local stress is a critical variable that determines where fatigue cracks nucleate. This is well established from laboratory and service experience. However, in the present study, we address issues of how, in high stress regions, crack nucleation mechanisms are affected by environmental and material variables. This is accomplished by presenting results of tapered corrosion-fatigue tests that were analyzed to describe the kinetics of crack nucleation and of early growth.

4.2.1 Corrosion-Fatigue Crack Nucleation Kinetics.

Table 1 gives a summary of the test conditions used to analyze the nucleation and early growth rate of corrosion fatigue cracks. To characterize the effect of environment and material condition on crack nucleation kinetics, we compared the number of cracks present on the corners of the tapered gage section of the specimens, as shown schematically in figure 13. We made comparison between tests that differed with respect to solution pH, specimen orientation, surface roughness, and surface coating. To better estimate the significance of the observed differences in crack nucleation kinetics, we conducted a series of replicate tests and determined the magnitude of random variations in crack density. Examination of results from replicate tests (see table 2 and figure 20) shows that the maximum difference, expressed as a ratio, is no greater than a factor of 2.1 and, on average, the difference is 1.52. Using these factors as a basis to estimate the relative magnitude of the random variation, figures 21 through 24 show the effects of pH, specimen orientation, surface roughness, and surface coating, respectively, on the number of cracks found in the test specimens.

Tables 3 through 6 show the results in tabular form. The observed trends in crack density were as follows:

- The pH 2 and pH 10 environments produce approximately the same number of cracks, which is greater than that produced by the pH 6 environment.
- A slight but consistent tendency for lower crack densities was observed in specimens in the horizontal orientation (i.e., when the applied stress was parallel to the rolling direction).
- The 30- μ m surfaces exhibited higher crack densities than the 5- μ m surfaces in the pH 6 environment. Very little effect of surface roughness was observed in the pH 2 environment. Crack densities in the as-machined condition were not included in the comparison because of the difficulties in obtaining accurate crack counts. Deep machining scratches are difficult to distinguish from cracks.

Table 1

**CORROSION-FATIGUE TESTS USED IN THE ANALYSIS OF THE NUCLEATION
AND GROWTH RATE OF THE EARLY STAGES OF CRACKING**

Test No.	Condition of Skin Surface	Surface Condition of Edge of Sheet	Environment	pH	Orien-tation	s_{max} (% s_y)	Number of Cycles	Number of Cracks
1	As received	Machined	Air		V	95.8	42,000	0
2	As received	Machined	0.5 M NaCl	6	V	95.8	28,600	63
3	Bare	Machined	0.5 M NaCl	6	V	86.9	24,800	0
4	As received	Machined	0.5 M NaCl	2	V	95.4	19,650	80
5	As received	Machined	0.5 M NaCl	6	V	46.3	160,810	11
7	Clad only	Machined	0.5 M NaCl	6	V	95.3	24,660	6
8	As received	5 μ m polish	0.5 M NaCl	6	V	93.5	26,330	16
10	As received	5 μ m polish	0.5 M NaCl	6	V	93.4	20,000*	21
11	As received	Machined	0.5 M NaCl	6	V	93.5	14,630	21
12	As received	Machined	0.5 M NaCl	6	V	93.4	20,000*	23
13	As received	Machined	0.5 M NaCl	6	V	97.9	16,580	126
14	As received	Machined	0.5 M NaCl	6	V	49.9	264,380	17
15	As received	Machined	0.5 M NaCl	6	V	50.0	150,000*	56
16	As received	Machined	0.5 M NaCl	6	V	75.0	30,000*	64
17	Clad only	5 μ m polish	0.5 M NaCl	6	V	50.0	150,000*	23
19	As received	5 μ m polish	0.5 M NaCl	6	V	75	30,000*	95
21	Clad only	5 μ m polish	0.5 M NaCl	6	V	100	20,000	79
22	As received	5 μ m polish	0.5 M NaCl	6	V	50	104,440	24
23	Clad only	30 μ m polish	0.5 M NaCl	6	V	50	150,000*	31
24	Bare	30 μ m polish	0.5 M NaCl	6	V	50	150,000*	0
25	Bare	30 μ m polish	0.5 M NaCl	6	V	75	30,000*	3
26	Bare	30 μ m polish	0.5 M NaCl	6	V	100	20,000*	2
27	Bare	5 μ m polish	0.5 M NaCl	6	V	70	77,550	0
28	Bare	5 μ m polish	0.5 M NaCl	6	V	50	150,000*	0
29	Clad only	5 μ m polish	0.5 M NaCl	6	V	100	20,000*	69
30	As received	30 μ m polish	0.5 M NaCl	6	V	50	105,025	54
31	As received	30 μ m polish	0.5 M NaCl	2	V	75	24,790	65
32	Bare	30 μ m polish	0.5 M NaCl	2	V	50	150,000*	0
33	As received	30 μ m polish	0.5 M NaCl	6	V	50	80,880	107
34	Bare	5 μ m polish	Air	-	V	50	150,000*	0
35	Clad only	30 μ m polish	0.5 M NaCl	2	V	50	150,000*	28
36	Clad only	30 μ m polish	0.5 M NaCl	2	V	75	30,000*	54
37	As received	5 μ m polish	0.5 M NaCl	2	V	50	99,540	68
38	As received	5 μ m polish	0.5 M NaCl	10	V	50	94,310	71
39	Clad only	30 μ m polish	0.5 M NaCl	10	V	50	126,100	18
40	As received	5 μ m polish	0.5 M NaCl	2	V	50	80,060	52
41	As received	30 μ m polish	0.5 M NaCl	2	H	50	150,000*	35
42	As received	30 μ m polish	0.5 M NaCl	6	H	50	125,160	53
43	As received	30 μ m polish	Air	-	H	50	150,000*	0
44	As received	30 μ m polish	0.5 M NaCl	10	H	50	150,000*	78
45	Clad only	30 μ m polish	0.5 M NaCl	10	H	50	150,000*	35
46	Clad only	0.05 μ m polish	Air	-	H	50	150,000*	2
47	Clad only	0.05 μ m polish	0.5 M NaCl	6	H	50	132,340	5
48	Clad only	30 μ m polish	0.5 M NaCl	6	H	75	30,000*	38
49	Clad only	30 μ m polish	0.5 M NaCl	10	H	75	30,000*	37
50	Clad only	30 μ m polish	0.5 M NaCl	2	H	100	20,000*	55
51	Clad only	30 μ m polish	0.5 M NaCl	6	H	100	20,000*	52
52	Clad only	30 μ m polish	0.5 M NaCl	6	H	75	30,000*	67
53	Clad only	30 μ m polish	0.5 M NaCl	2	H	75	30,000*	40
60	Clad only	5 μ m polish	0.5 M NaCl	2	V	50	97,290	46
61	As received	5 μ m polish	0.5 M NaCl	6	H	50	150,000*	9
66	As received	5 μ m polish	0.5 M NaCl	2	H	50	74,500	44
71	As received	5 μ m polish	0.5 M NaCl	10	H	50	150,000*	15
72	As received	5 μ m polish	0.5 M NaCl	6	V	50	125,190	11
114	Clad only	Machined	Air	-	V	75	82,730	0

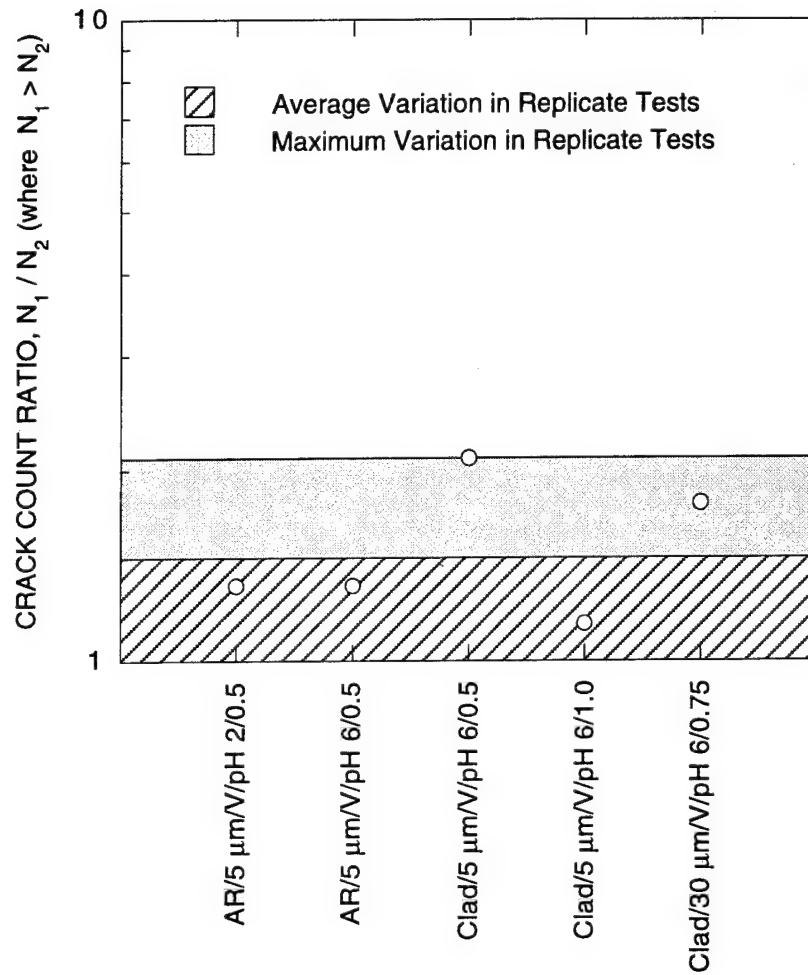
* Test interrupted at prescribed number of cycles. Specimen did not fail.

Table 2

COMPARISON OF CRACK COUNTS IN REPLICATE TESTS^a

Specimen Number	Number of Cracks	Log Difference in Number of Cracks
As received condition, 5 μm polish, vertical orientation, pH 2, $\sigma_{\text{max}} = 0.5 \sigma_y$		
37	68	0.12
40	52	
As received condition, 5 μm polish, vertical orientation, pH 6, $\sigma_{\text{max}} = \sigma_y$		
10	21	0.12
8	16	
Clad only condition, 5 μm polish, vertical orientation, pH 6, $\sigma_{\text{max}} = 0.5 \sigma_y$		
17	23	0.32
72	11	
Clad only condition, 5 μm polish, vertical orientation, pH 6, $\sigma_{\text{max}} = \sigma_y$		
29	69	0.06
21	79	
Clad only condition, 30 μm polish, vertical orientation, pH 6, $\sigma_{\text{max}} = 0.75 \sigma_y$		
48	38	0.25
52	67	

^a Log difference = $\log_{10} (X_1) - \log_{10} (X_2)$

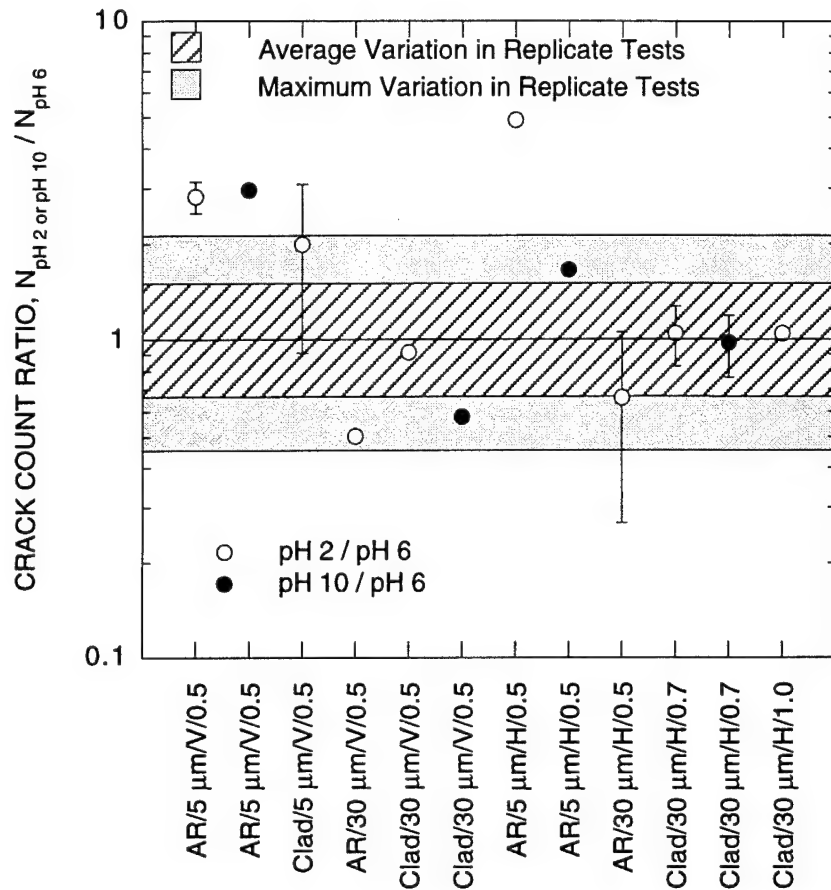


CAM-5082-27

Figure 20. Number of cracks on replicate test specimens.

Each data point is the ratio of the number of cracks on specimens tested under identical conditions. Test condition designations on the abscissa are interpreted as follows:

Coating (AR = as received or Clad = clad only)
 / Surface Roughness (5 μm or 30 μm)
 / Orientation (H = horizontal or V = vertical) / pH (2 or 6)
 / Maximum Stress ($\sigma_{\text{max}}/\sigma_y$)



CAM-5082-28

Figure 21. Effect of pH on the number of cracks.

Each data point is the ratio of the number of cracks on specimens run under identical conditions except for pH level. Error bars indicate the range of data.

Test condition designations on the abscissa are interpreted as follows:

Coating (AR = as received or Clad = clad only)
 / Surface Roughness (5 μm or 30 μm)
 / Orientation (H = horizontal or V = vertical)
 / Maximum Stress ($\sigma_{\text{max}}/\sigma_y$)

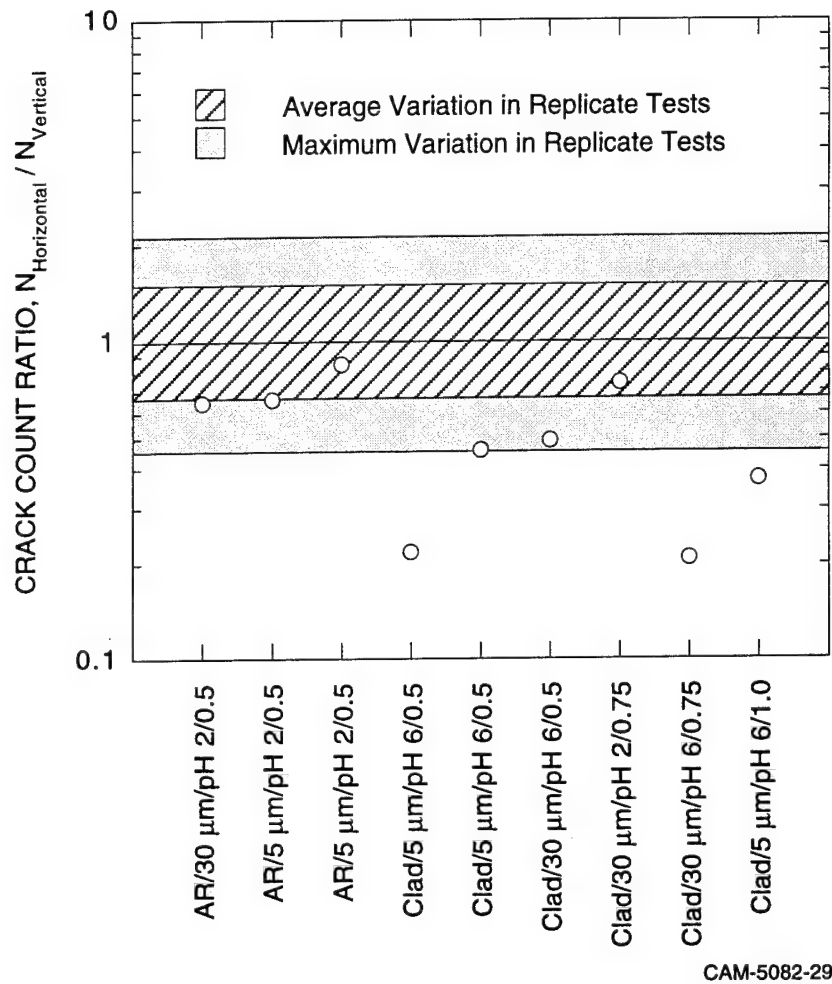
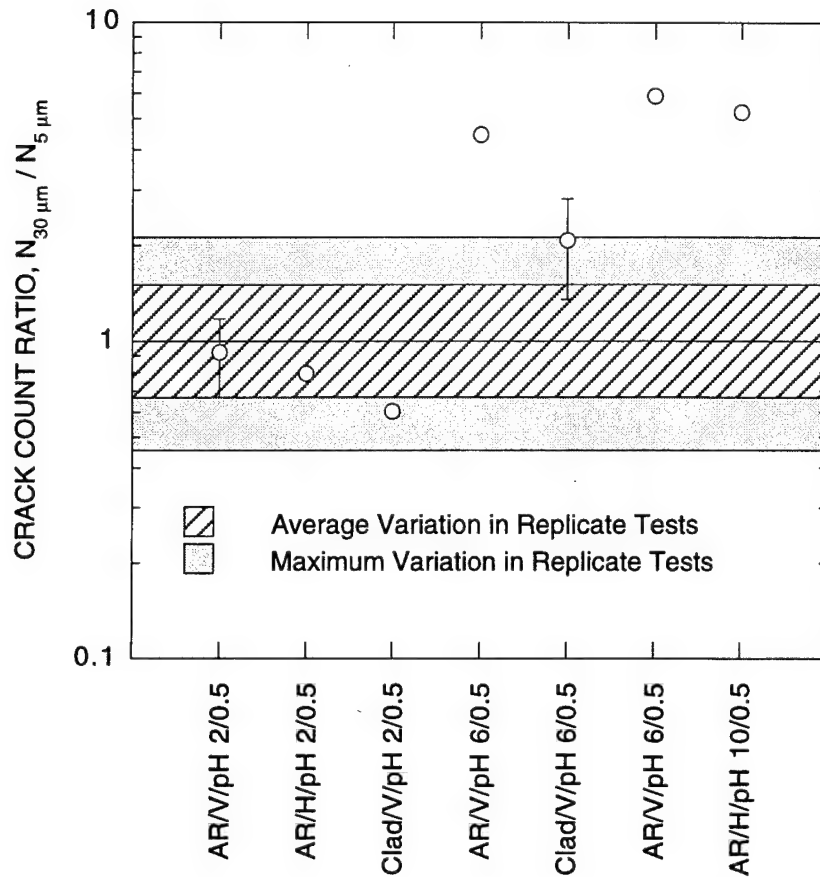


Figure 22. Effect of specimen orientation on the number of cracks.

Each data point is the ratio of the number of cracks on specimens run under identical conditions except for specimen orientation.
 Test condition designations on the abscissa are interpreted as follows:

Coating (AR = as received or Clad = clad only)
 / Surface Roughness (5 μm or 30 μm)
 / pH (2 or 6) / Maximum Stress ($\sigma_{\text{max}} / \sigma_y$)



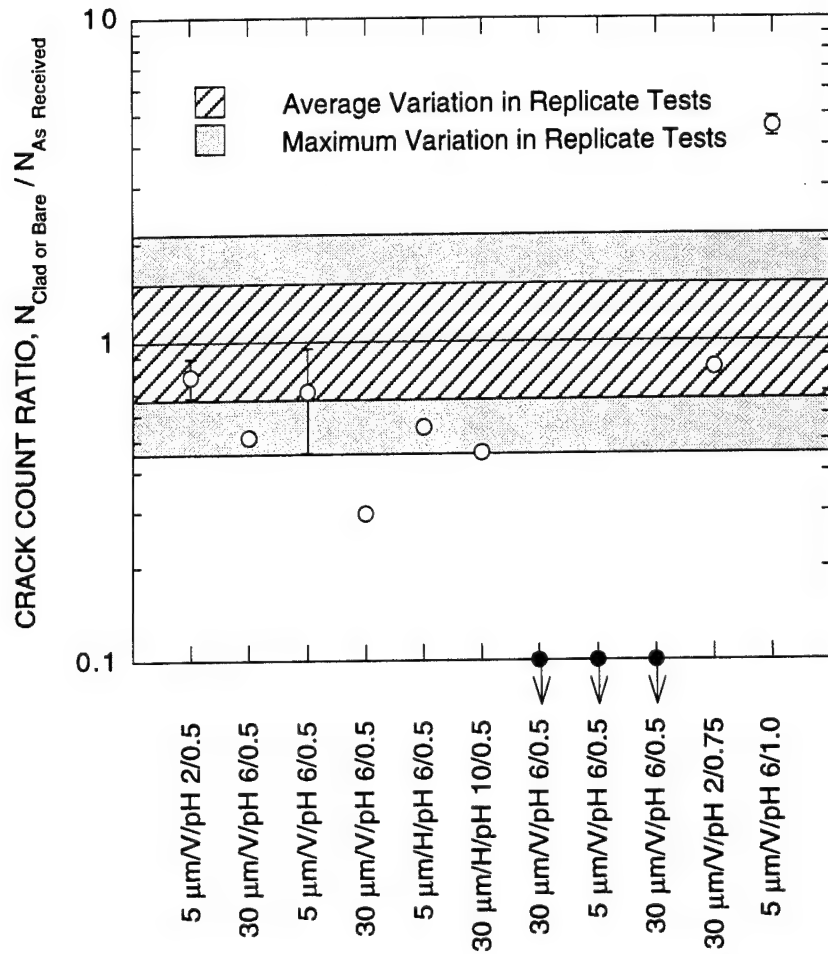
CAM-5082-30

Figure 23. Effect of surface roughness on the number of cracks.

Each data point is the ratio of the number of cracks on specimens run under identical conditions except for surface roughness. Error bars indicate the range of data.

Test condition designations on the abscissa are interpreted as follows:

Coating (AR = as received or Clad = clad only)
 / Orientation (H = horizontal or V = vertical)
 / pH (2 or 6) / Maximum Stress (σ_{\max}/σ_y)



CAM-5082-31

Figure 24. Effect of surface coating on the number of cracks.

Each data point is the ratio of the number of cracks on specimens run under identical conditions except for specimen coating. Error bars indicate the range of data.

Test condition designations on the abscissa are interpreted as follows:

Surface Roughness (5 μm or 30 μm)
 / Orientation (H = horizontal or V = vertical)
 / pH (2 or 6) / Maximum Stress ($\sigma_{\text{max}}/\sigma_y$)

Table 3
EFFECT OF pH ON CRACK NUCLEATION AND GROWTH RATE^{a,b}

Specimen Number	pH	Number of Cracks	Log Difference in Number of Cracks	Crack Growth Rate	Log Difference in Crack Growth Rate
As received condition, 5 μ m polish, vertical orientation, $\sigma_{\max} = 0.5 \sigma_y$					
37	2	68	0.45	4.30 E-09	0.09
40	2	52	0.34	1.35 E-09	-0.41
22	6	24		3.47 E-09	
38	10	71	0.47	8.90 E-10	-0.59
Clad only condition, 5 μ m polish, vertical orientation, $\sigma_{\max} = 0.5 \sigma_y$					
60	2	46	0.30 0.62	1.41 E-09	1.00 1.16
17	6	23		1.41 E-10	
72	6	11		2.06 E-09	
As received condition, 30 μ m polish, vertical orientation, $\sigma_{\max} = 0.5 \sigma_y$					
30	2	54		1.13 E-09	
33	6	107	-0.30	3.00 E-10	0.58
Clad only condition, 30 μ m polish, vertical orientation, $\sigma_{\max} = 0.5 \sigma_y$					
35	2	28	-0.04	1.40 E-09	0.82
23	6	31		2.11 E-10	
39	10	18	-0.24	2.06 E-09	0.99
As received condition, 5 μ m polish, horizontal orientation, $\sigma_{\max} = 0.5 \sigma_y$					
66	2	44	0.69	4.09 E-09	1.13
61	6	9		3.01 E-10	
71	10	15	0.22	9.82 E-11	-0.49
As received condition, 30 μ m polish, horizontal orientation, $\sigma_{\max} = 0.5 \sigma_y$					
41	2	35	-0.18	1.62 E-09	-0.08
42	6	53		1.95 E-09	
44	10	78	0.16	1.49 E-09	-0.12
Clad only condition, 30 μ m polish, horizontal orientation, $\sigma_{\max} = 0.75 \sigma_y$					
53	2	40	0.02 -0.22	1.70 E-09	0.31 0.24
48	6	38		8.41 E-10	
52	6	67		9.70 E-10	
49	10	37	-0.01 -0.26	2.08 E-10	-0.61 -0.67
Clad only condition, 30 μ m polish, horizontal orientation, $\sigma_{\max} = \sigma_y$					
50	2	55	0.02	1.22 E-09	-0.02
51	6	52		1.29 E-09	

^a Log differences = $\log(X) - \log(X_{pH\ 6})$

^b Crack growth rates were obtained from a fit to an integrated form of the Paris Equation to the crack size distribution on each specimen. The crack growth rates are for $\Delta K = 1 \text{ MPa}\sqrt{\text{m}}$. Units are in m/cycle.

Table 4

EFFECT OF ORIENTATION ON CRACK NUCLEATION AND GROWTH RATE^{a,b}

Specimen Number	Orientation	Number of Cracks	Log Difference in Number of Cracks	Crack Growth Rate	Log Difference in Crack Growth Rate
As received condition, 30 μm polish, pH 2, $\sigma_{\text{max}} = 0.5 \sigma_y$					
41	Horizontal	35	-0.19	1.625 E-09	0.16
30	Vertical	54		1.125 E-09	
As received condition, 5 μm polish, pH 2, $\sigma_{\text{max}} = 0.5 \sigma_y$					
66	Horizontal	44		4.094 E-09	
37	Vertical	68	-0.18	4.262 E-09	-0.02
40	Vertical	52	-0.07	1.349 E-09	0.48
Clad only condition, 5 μm polish, pH 6, $\sigma_{\text{max}} = \sigma_y$					
61	Horizontal	9	-0.43	3.013 E-10	-1.06
22	Vertical	24		3.466 E-09	
Clad only condition, 5 μm polish, pH 6, $\sigma_{\text{max}} = 0.5 \sigma_y$					
47	Horizontal	5			
17	Vertical	23	-0.66	1.414 E-10	
72	Vertical	11	-0.34	2.063 E-09	
Clad only condition, 30 μm polish, pH 2, $\sigma_{\text{max}} = 0.75 \sigma_y$					
53	Horizontal	40	-0.13	1.697 E-09	0.27
36	Vertical	54		9.218 E-10	
Clad only condition, 30 μm polish, pH 6, $\sigma_{\text{max}} = 0.5 \sigma_y$					
42	Horizontal	53	-0.31	1.953 E-09	0.81
33	Vertical	107		3.004 E-10	
Clad only condition, 30 μm polish, pH 6, $\sigma_{\text{max}} = 0.75 \sigma_y$					
71	Horizontal	15	-0.68	9.824 E-11	-0.96
38	Vertical	71		8.897 E-10	

^a Log differences = $\log(X_{\text{horizontal}}) - \log(X_{\text{vertical}})$

^b Crack growth rates were obtained from a fit to an integrated form of the Paris Equation to the crack size distribution on each specimen. The crack growth rates are for $\Delta K = 1 \text{ MPa}\sqrt{\text{m}}$. Units are in m/cycle.

Table 5

EFFECT OF ROUGHNESS ON CRACK NUCLEATION AND GROWTH RATE^{a,b}

Specimen Number	Roughness	Number of Cracks	Log Difference in Number of Cracks	Crack Growth Rate	Log Difference in Crack Growth Rate
As received, vertical orientation, pH 2, $\sigma_{\max} = 0.5 \sigma_y$					
37	5 μm	68		4.262 E-09	
40	5 μm	52		1.349 E-09	
30	30 μm	54	-0.10 0.02	1.125 E-09	-0.58 -0.08
As received, horizontal orientation, pH 2, $\sigma_{\max} = 0.5 \sigma_y$					
66	5 μm	44		4.094 E-09	
41	30 μm	35	-0.10	1.625 E-09	-0.40
As received, vertical orientation, pH 6, $\sigma_{\max} = 0.5 \sigma_y$					
22	5 μm	24		3.466 E-09	
33	30 μm	107	0.65	3.004 E-10	-1.06
Clad only, vertical orientation, pH 6, $\sigma_{\max} = 0.5 \sigma_y$					
17	5 μm	23		1.414 E-10	
72	5 μm	11		2.063 E-09	
23	30 μm	31	0.45 0.13	2.109 E-10	0.17 -0.99
As received, vertical orientation, pH 6, $\sigma_{\max} = 0.5 \sigma_y$					
61	5 μm	9		3.013 E-10	
42	30 μm	53	0.77	1.953 E-09	-1.19
As received, horizontal orientation, pH 10, $\sigma_{\max} = 0.5 \sigma_y$					
71	5 μm	15		9.824 E-11	
44	30 μm	78	0.72	1.490 E-09	1.18

^a Log differences = $\log(X_{30\mu\text{m}}) - \log(X_{5\mu\text{m}})$

^b Crack growth rates were obtained from a fit to an integrated form of the Paris Equation to the crack size distribution on each specimen. The crack growth rates are for $\Delta K = 1 \text{ MPa}\sqrt{\text{m}}$. Units are in m/cycle.

Table 6

**EFFECT OF SURFACE COATING ON CRACK NUCLEATION
AND GROWTH RATE^{a,b}**

Specimen Number	Surface Coating	Number of Cracks	Log Difference in Number of Cracks	Crack Growth Rate	Log Difference in Crack Growth Rate
5 μm polish, vertical orientation, pH 2, $\sigma_{\text{max}} = 0.5 \sigma_y$					
37	As received	68		4.262 E-09	
40	As received	52		1.349 E-09	
60	Clad only	46	-0.17 -0.05	1.407 E-09	-0.48 0.02
30 μm polish vertical orientation, pH 6, $\sigma_{\text{max}} = 0.5 \sigma_y$					
30	As received	54		1.125 E-09	
35	Clad only	28	-0.29		
30 μm polish, vertical orientation, pH 2, $\sigma_{\text{max}} = 0.75 \sigma_y$					
31	As received	65		1.379 E-09	
36	Clad only	54	-0.08	9.218 E-10	-0.17
5 μm polish, vertical orientation, pH 6, $\sigma_{\text{max}} = 0.5 \sigma_y$					
22	As received	24		3.466 E-09	
17	Clad only	23	-0.02	1.414 E-10	-1.39
72	Clad only	11	-0.34	2.063 E-09	-0.23
30 μm polish, vertical orientation, pH 6, $\sigma_{\text{max}} = 0.5 \sigma_y$					
33	As received	107		3.004 E-10	
23	Clad only	31	-0.53	2.109 E-10	-0.15
5 μm polish, vertical orientation, pH 6, $\sigma_{\text{max}} = \sigma_y$					
10	As received	21		2.059 E-09	
8	As received	16		1.732 E-09	
29	Clad only	69	0.52 0.63	2.157 E-09	0.02 0.10
21	Clad only	79	0.58 0.69	7.732 E-10	-0.43 -0.35
30 μm polish, horizontal orientation, pH 10, $\sigma_{\text{max}} = 0.5 \sigma_y$					
44	As received	78		1.490 E-09	
45	Clad only	35	-0.34	5.896 E-10	0.40

^a Log differences = $\log(X_{\text{clad only}}) - \log(X_{\text{as received}})$

^b Crack growth rates were obtained from a fit to an integrated form of the Paris Equation to the crack size distribution on each specimen. The crack growth rates are for $\Delta K = 1 \text{ MPa}\sqrt{\text{m}}$. Units are in m/cycle.

- Very few cracks were observed in bare material. Clad material produced fewer cracks than as received material, except in two experiments. The two exceptions differed only in that the stress level was the highest of all conditions considered.

In addition to the test-by-test comparison described above, we examined all of the data simultaneously to extract, statistically, evidence of the effects of the independent variables on crack nucleation. Table 7 shows the analysis-of-variance results from a fit to the data with a least squares analysis.¹⁷ In this model, variables based on pH, orientation, roughness, coating, and number of cycles times the maximum stress (cycles * σ_{\max}) were included. The coating and orientation variables were given arbitrary values (0 or 1 in this case) to distinguish between the two conditions treated in the analysis (the clad only and as received conditions for the coating variable and the longitudinal and horizontal conditions for the orientation variable). The model assumes that the effect of pH 2 and 10 are the same, because high and low pH values enhance the solubility of the surface oxide. The effect of number of cycles and stress level was included in the model as the product of these two variables (i.e., cycles * σ_{\max}). Fatigue life correlations often relate stress to number of cycles as follows:

$$N \sigma^p = \text{constant} \quad (8)$$

where N is the number of cycles to failure, σ is the stress amplitude, and p is a constant that is usually between about 8 and 15.¹⁸ For the present case, we preserved the general form of this equation, but set "a" equal to unity to obtain a better correlation (i.e., higher F-statistic) than values in the commonly observed range.

The quality of the correlation meets a 0.05 level of significance in several instances (i.e., in usefulness of the correlation as a whole as defined by the F-statistic and in the significance of coating, roughness, and (cycles * σ_{\max}) as defined by the t-statistic. The other two variables (pH and orientation) miss this level of significance by a small amount. In each case, the direction of the effect of the independent variable on the number of cracks is consistent with the conclusions drawn from the test-by-test comparison of data shown in figures 21 through 24. Figure 25 shows plots of the residuals as a function of each independent variable and reveals no apparent biases. This suggests that the assumptions in formulating the analysis have produced evenly distributed errors that are not biased.

These analyses reveal a modest but statistically significant effect (or nearly so) for each independent variable examined. Possible explanations for their effects are presented below.

Table 7

**STATISTICAL ANALYSIS OF THE NUMBER OF CRACKS
ON CORROSION-FATIGUE SPECIMENS^a**

		1	2	3	4	5
		pH	Orientation	Log (Roughness)	Coating	Log (Cycles* Maximum Stress)
B_i	5.108	-0.1224	0.1432	0.6621	0.1642	-0.5229
SE_i	1.2896	0.0910	0.0937	0.2240	0.0955	0.1956
SE_{N_c}	0.2497					
SS_{reg}	1.3328					
SS_{resid}	1.6215					
df	26					
$ t_i $		1.34	1.53	2.96	1.72	2.67
$ t_i > t_{\alpha/2}$ $t_{\alpha/2} = 1.71$		no	no	yes	yes	yes
r^2	0.4511					
F	4.274					
$F > F_{crit}$ $F_{crit} = 2.59$	yes					

^a $\text{Log}(N_c) = B_0 + B_1 X_1 + B_2 X_2 + B_3 X_3 + B_4 X_4 + B_5 X_5$, where N_c = number of cracks, B_i are coefficients, and X_i are the following independent variables:

X_1 = pH such that 1 = pH 6, 0 = pH 2 and 10

X_2 = orientation such that 0 = horizontal and 1 = vertical

X_4 = coating such that 0 = clad only and 1 = as received

X_3 = log (roughness in micrometers); note: 30 μm finish = 0.8 μm , 5 μm finish = 0.3 μm , 0.5 μm finish = 0.2 μm , as machined finish is not included in the analysis

X_4 = coating such that 0 = clad only and 1 = as received

X_5 = log (number of cycles * maximum stress) with stress stated as a fraction of the yield.

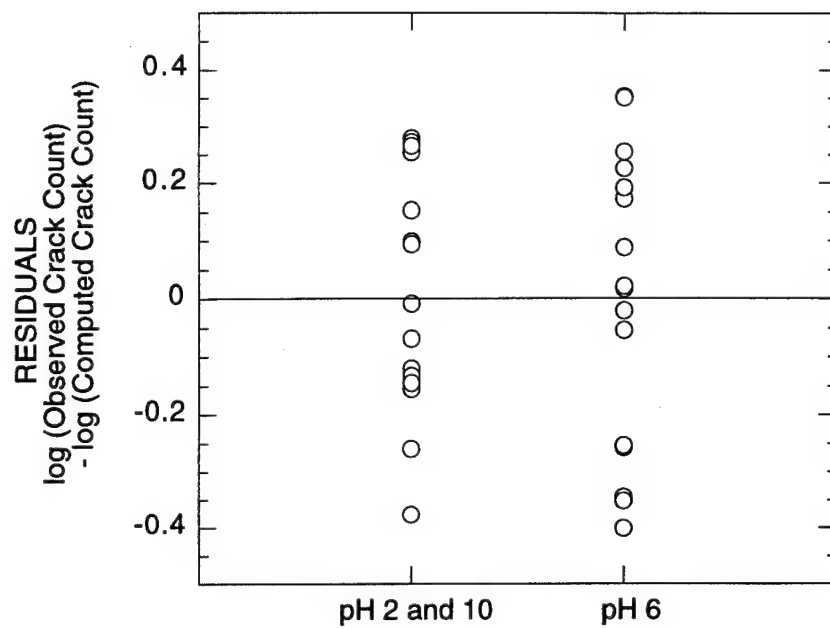
SE_i is the standard error for B_i , SE_{N_c} is the standard error for N_c , SS_{reg} is the regression sum of squares, SS_{resid} is the residual sum of squares, and df is the degrees of freedom.

t_i is the t-statistic value for B_i , and $t_{\alpha/2}$ is the t-statistic value for a level of significance of 0.05.

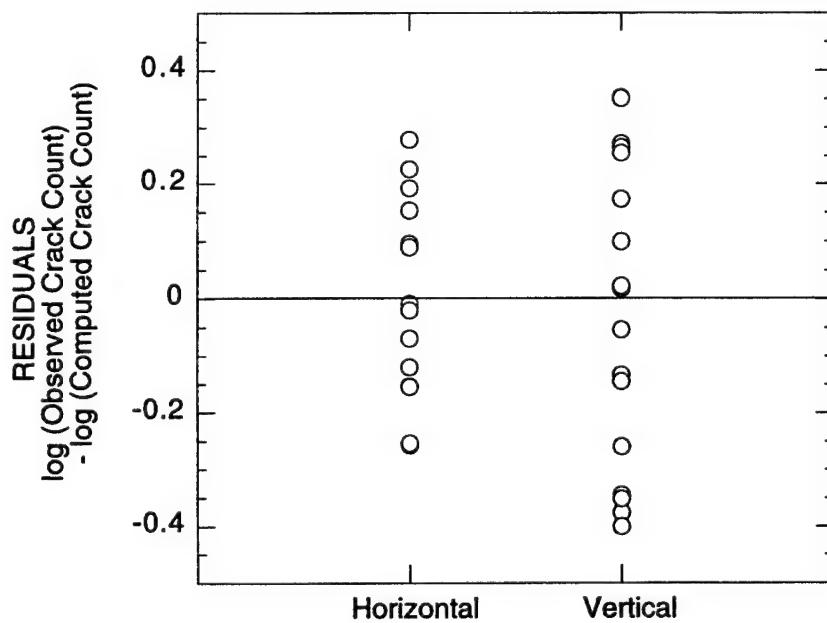
If $|t_i| > t_{\alpha/2}$, then the coefficient is statistically significant to a level of 0.05.

r^2 is the coefficient of determination such that 1 indicates a perfect correlation and 0 indicates that the equation is not helpful in predicting fatigue life.

F determines whether the observed relationship between N_c and the independent variables occurs by chance. If $F > F_{crit}$, the regression equation is useful for prediction to a level of significance of 0.05.



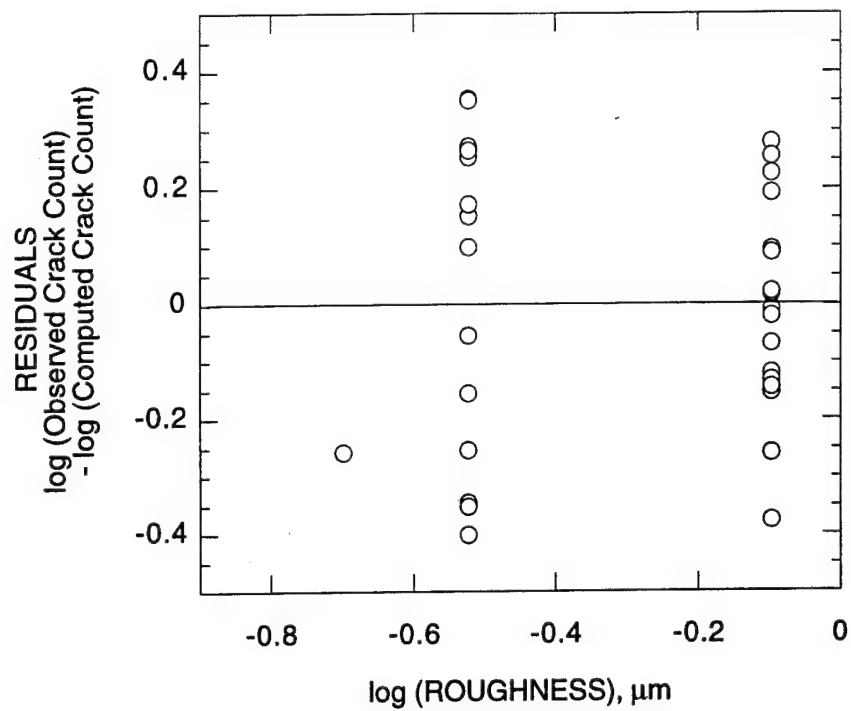
(a) pH residuals



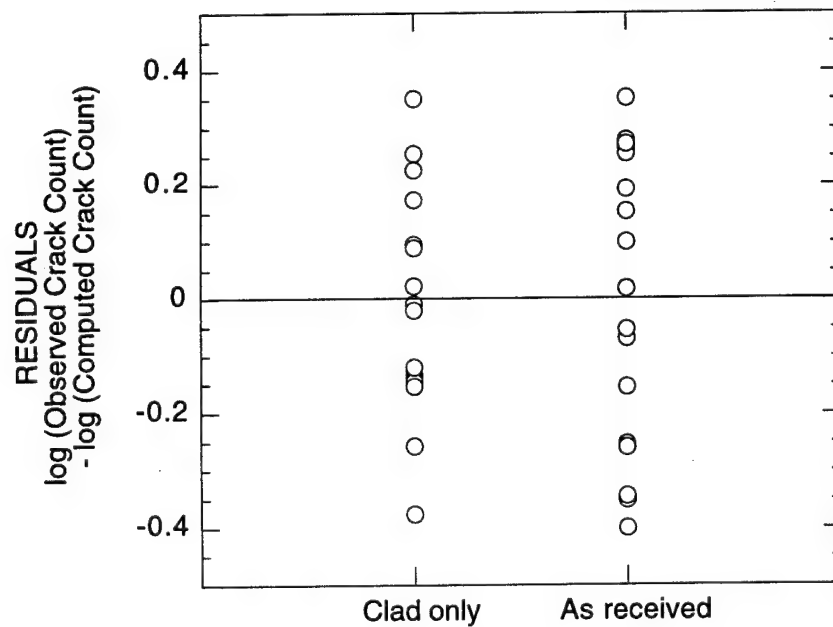
(b) Orientation residuals

CAM-5082-32

Figure 25. Residuals for crack nucleation analysis.



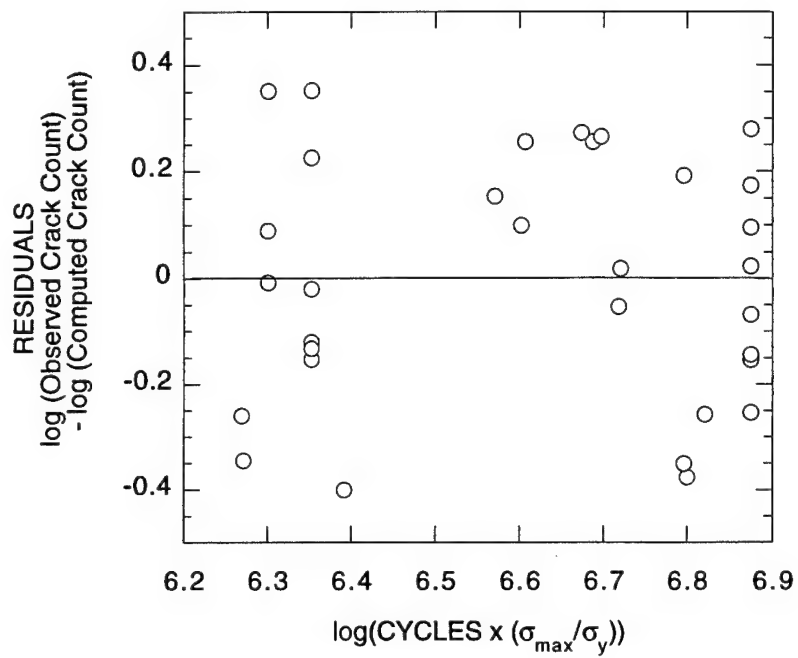
(c) Roughness residuals



(d) Coating residuals

CAM-5082-33

Figure 25. Residuals for crack nucleation analysis (Continued).



(e) Cycles times maximum stress residuals

CAM-5082-34

Figure 25. Residuals for crack nucleation analysis (Concluded).

The increased crack nucleation rate at high and low pH environments is probably a result of the higher solubility of the corrosion products that form on aluminum at pH values above and below pH 6.¹⁹ A more soluble protective film can be expected to enhance corrosion processes that lead to corrosion fatigue cracking.

The source of the effect of specimen orientation on crack nucleation is unclear. The grain structure of the Alclad layer exhibits no directionality (see figure 7). However, traces of a directional etch pattern appear as streaks that traverse the grain structure on the surface of the Alclad layer. These streaks were apparent to the naked eye on the interior surface of the aircraft skin and were oriented perpendicular to the hoop direction. The streaks were not found on the exterior skin surface, apparently because they were obscured by in-service corrosion. They appear to be surface features resulting from the sheet rolling process. Corrosion fatigue tests run with specimens in the vertical orientation produce cracks that run parallel to the streaks. Possibly, perturbations in surface topography or hardness represented by the streaks have created conditions that promote crack nucleation that are orientation dependent. However, no clear interaction was identified from detailed examination of the location of the crack nucleation sites.

One might expect that surface roughness would affect the corrosion fatigue crack nucleation rate when scratches produce local stress concentrations. However, SEM examination did not reveal a clear association between specific scratches and the sites of corrosion fatigue crack nucleation. This suggests that other factors associated with surface preparation might contribute to crack nucleation. Enhanced hydrogen permeability from mechanically deformed surface layers²⁰ and hydrogen uptake resulting from slurry polishing²¹ have been suggested by other investigators to be promoters of hydrogen embrittlement in aluminum that could influence the early stages of crack formation. The lack of a significant effect of roughness in the pH 2 environment could also be considered consistent with a hydrogen-embrittlement-based crack propagation mechanism. If, for example, the enhanced hydrogen absorption resulting from a mechanically deformed roughened surface is swamped by the enhancement resulting from the lack of an effective oxide layer (rendered so by the solubility of the oxide layer in low pH environments), then we might expect the observed result that corrosion-fatigue cracking following exposures to low pH environments do not show a strong effect of surface roughness.

The effect of surface coating on corrosion fatigue crack nucleation kinetics could be due to several things. The low number of crack nucleation sites in the bare skin compared with clad material is a consequence of the substantial differences in environmental attack. Corrosion attack to bare

material was observed as either pitting corrosion at constituent particles or intergranular cracking. In clad material, attack was primarily in the form of crystallographic pits, although some pits nucleated at constituent particles in the pH 2 environment. These observations of crack nucleation sites in clad and bare material are consistent with observations by other investigators.^{20,23} Evidently, the pits that formed in the bare material were sufficiently variable in depth and location that only a few of the largest pits served as crack nucleation sites. In the clad material, cracks usually nucleated in the clad layer at or near the crystallographic pit colonies. Small cracks followed distinct crystallographic planes in a manner often referred to as Stage I cracking.²⁴

In most cases, the as received materials produced slightly more cracks in the clad than did the clad only materials. Here, one is tempted to associate the higher cracking densities of the as received specimens to the catchment effect. That is, in as received material, the painted surface produces a higher current density in the clad area that is exposed than is the case when the clad is bare.[†] The higher current density, in turn, accelerates the environmentally assisted mechanisms, whatever they may be, that lead to crack nucleation.

The one exception to the general observation of the effect of surface coating, as shown in figure 24, is when the comparison is made between tests conducted at the highest maximum stress level, $\sigma_{\max}/\sigma_y = 1.0$. The reason for this is not clear.

In later sections of this report, we continue our examination of the possible role of hydrogen in causing the sensitivity to these variables.

4.2.2 Corrosion-Fatigue Crack Propagation Kinetics.

We analyzed corrosion-fatigue crack propagation by examining the distribution of crack lengths on the tapered gage lengths of the corrosion fatigue test specimens. We evaluated the effect of test conditions in a similar manner to that of the crack nucleation kinetics analysis. We first present a test-by-test comparison to assess the effects of pH, material orientation, surface roughness, and coating on crack growth rate. Then, we present an analysis in which all data are considered simultaneously.

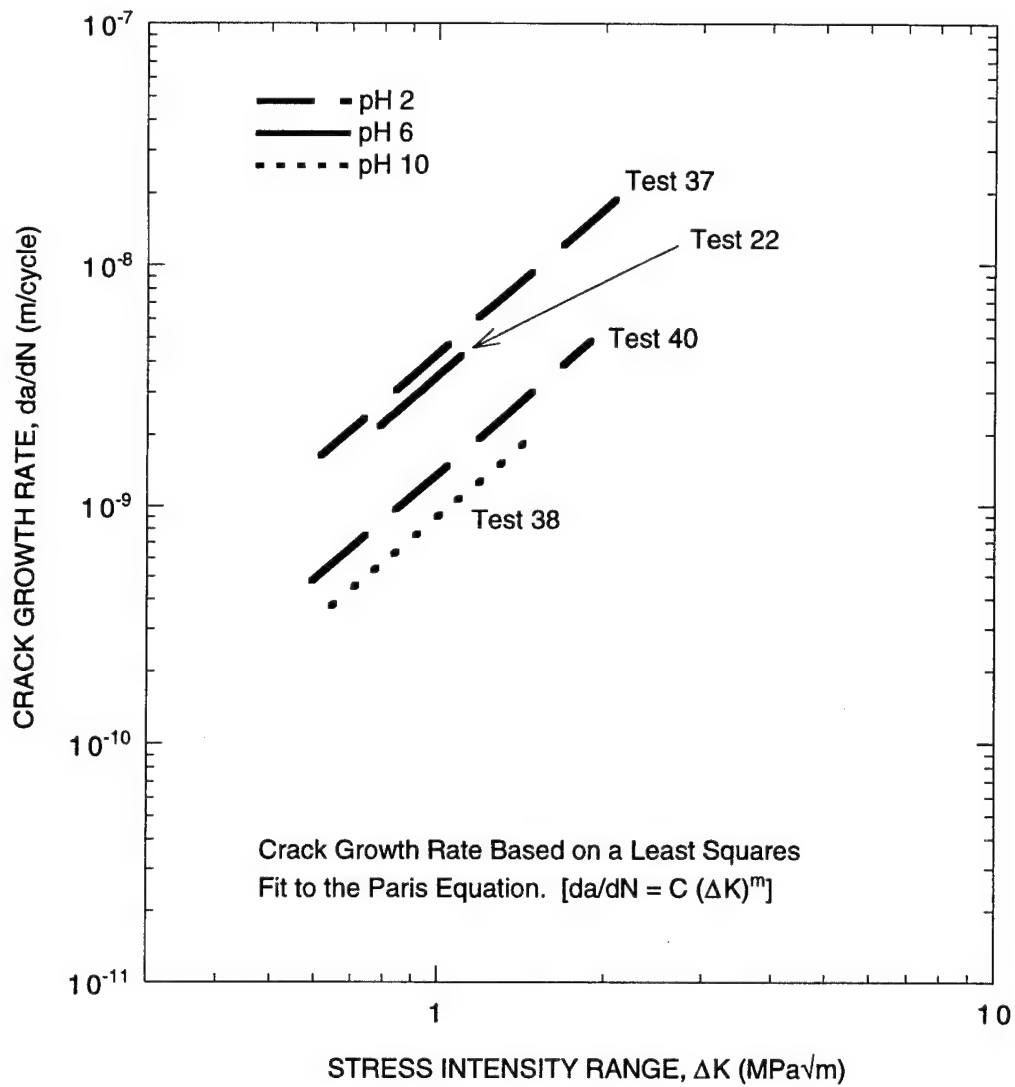
[†]A simple calculation of exposed areas of the corrosion-fatigue specimens indicates that the exposed core to clad ratio (i.e., anode to cathode ratio) is about 7 and 0.1 for the as-received and clad-only specimens, respectively.

Figures 26 through 29 show variations in the crack growth rate trends for tests in which only one parameter is altered. We obtained the crack growth rate trends shown in these figures from the least squares analyses shown in the figures in the appendix. Tables 3 through 6 show the comparisons in tabular form. The trends in crack growth rate that are apparent from an inspection of these data are as follows:

- In some cases, the pH 2 environment exhibits a higher crack growth rate than the pH 6 environment. The pH 10 environment produces a crack growth rate that is roughly equal to, or perhaps slightly below, that of the pH 6 environment.
- Material orientation appears to have no consistent effect on crack growth rate, based on the data in figure 27.
- The effect of surface roughness is mixed and shows no consistent effect in comparisons between the 5- μm and 30- μm finishes (see figure 28). Results from test specimens with machined surfaces were not included due to difficulties in obtaining accurate crack length measurements.
- Crack growth rates were not obtained from the bare specimens because too few cracks were observed on the specimen gage lengths. There is a moderately consistent trend that the as received condition results in a higher crack growth rate than the clad only condition, as is evident in the data shown in figure 29.

In addition to the independent variables described above, a weak dependence of the crack growth rate on stress at low stress intensities was observed that was not entirely accounted for by the Paris Equation. Figure 30 shows the least squares fits to equation 5 for all the tests presented in figures 26 through 29. The data are scattered due, in part, to the range of test conditions considered. However, the overall distribution of the data suggests that the lowest ΔK values fall below a linear extrapolation of the trends shown by the data at the highest ΔK values. This, in turn, suggests that the data at the lowest ΔK values may be approaching a threshold stress intensity that equation 5 (the Paris Equation) does not accurately describe.

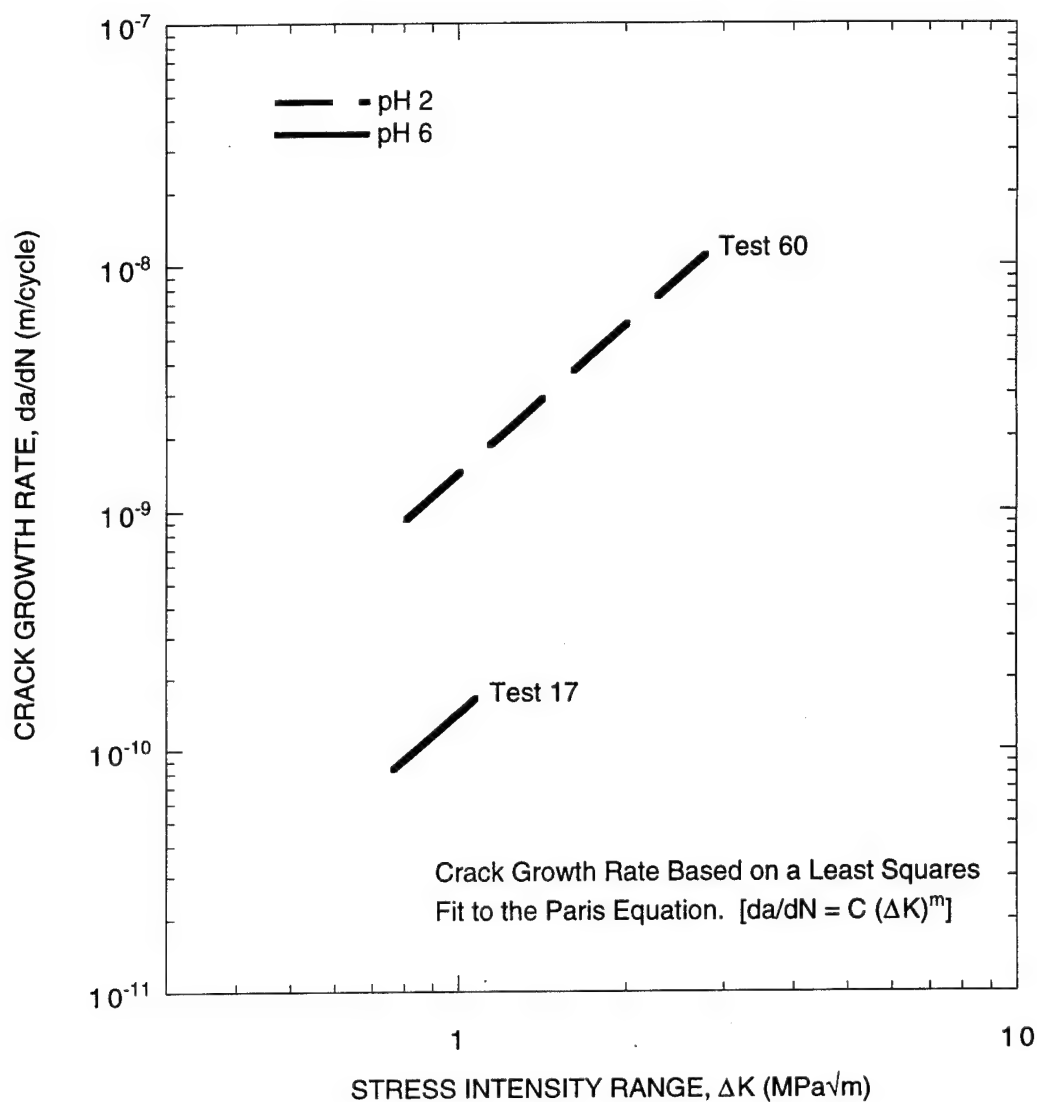
Table 8 shows the analysis-of-variance results from a least squares fit to the crack growth rate obtained from the fits of the Paris Equation to the data at a common value of ΔK (1 MPa $\sqrt{\text{m}}$, in this case). This is equivalent to an analysis-of-variance on the coefficient "C" in the Paris Equation as the dependent variable. The model used in this analysis (shown in the footnote for table 8) included independent variables based on pH, orientation, roughness, coating, and maximum stress. As with the crack nucleation analysis, the coating and orientation variables were given arbitrary values (0 or 1 in this case) to distinguish between the two conditions treated in the analysis (the clad only and as received conditions for the coating variable and the longitudinal and horizontal conditions for the orientation variable). Unlike the crack nucleation analysis, the model



(a) Comparison of specimens in the vertical orientation in the as-received condition with a 5 μm polish on the through-thickness surfaces

CAM-5082-35

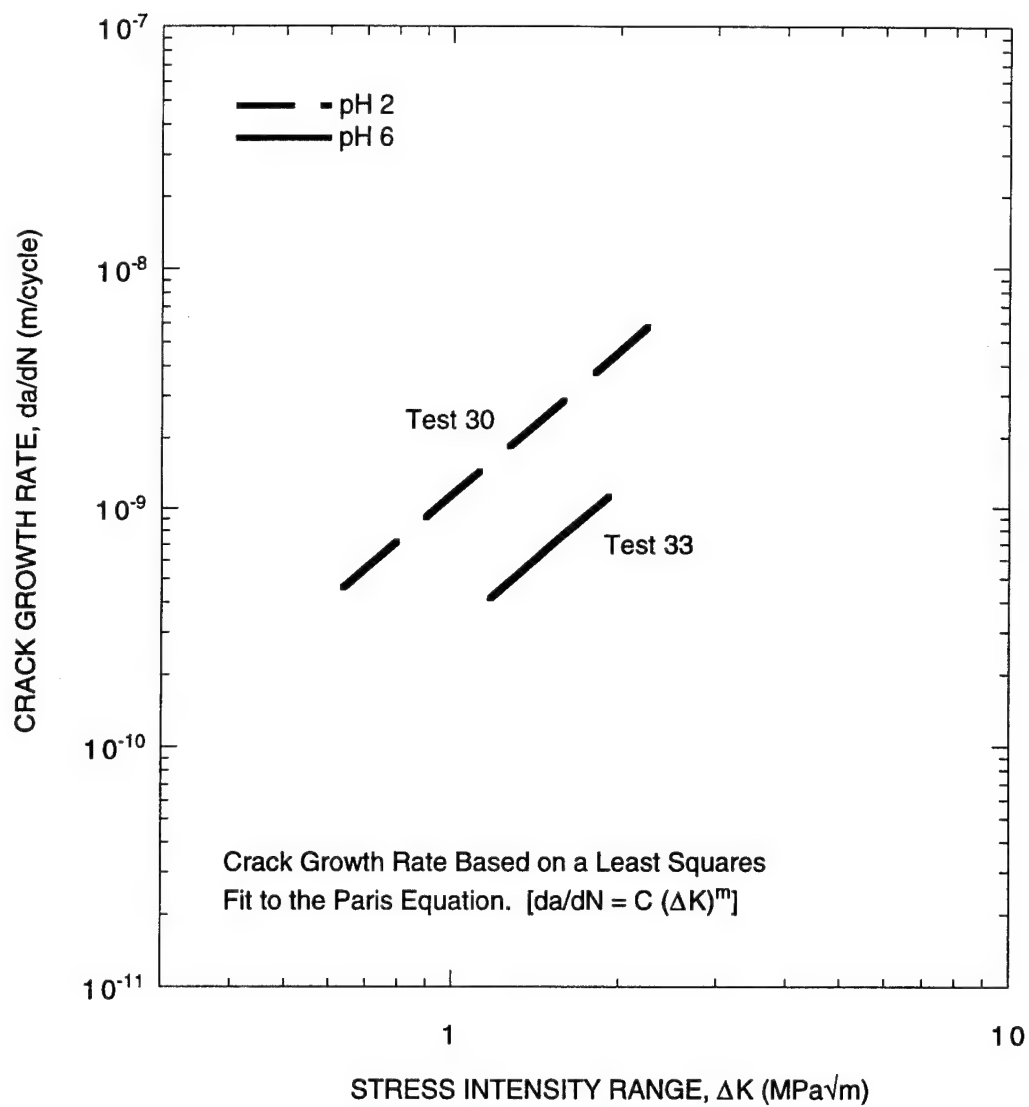
Figure 26. Effect of pH on the crack growth rate of small cracks in aircraft skin.



(b) Comparison of specimens in the vertical orientation in the clad-only condition with a 5 μ m polish on the through-thickness surfaces

CAM-5082-36

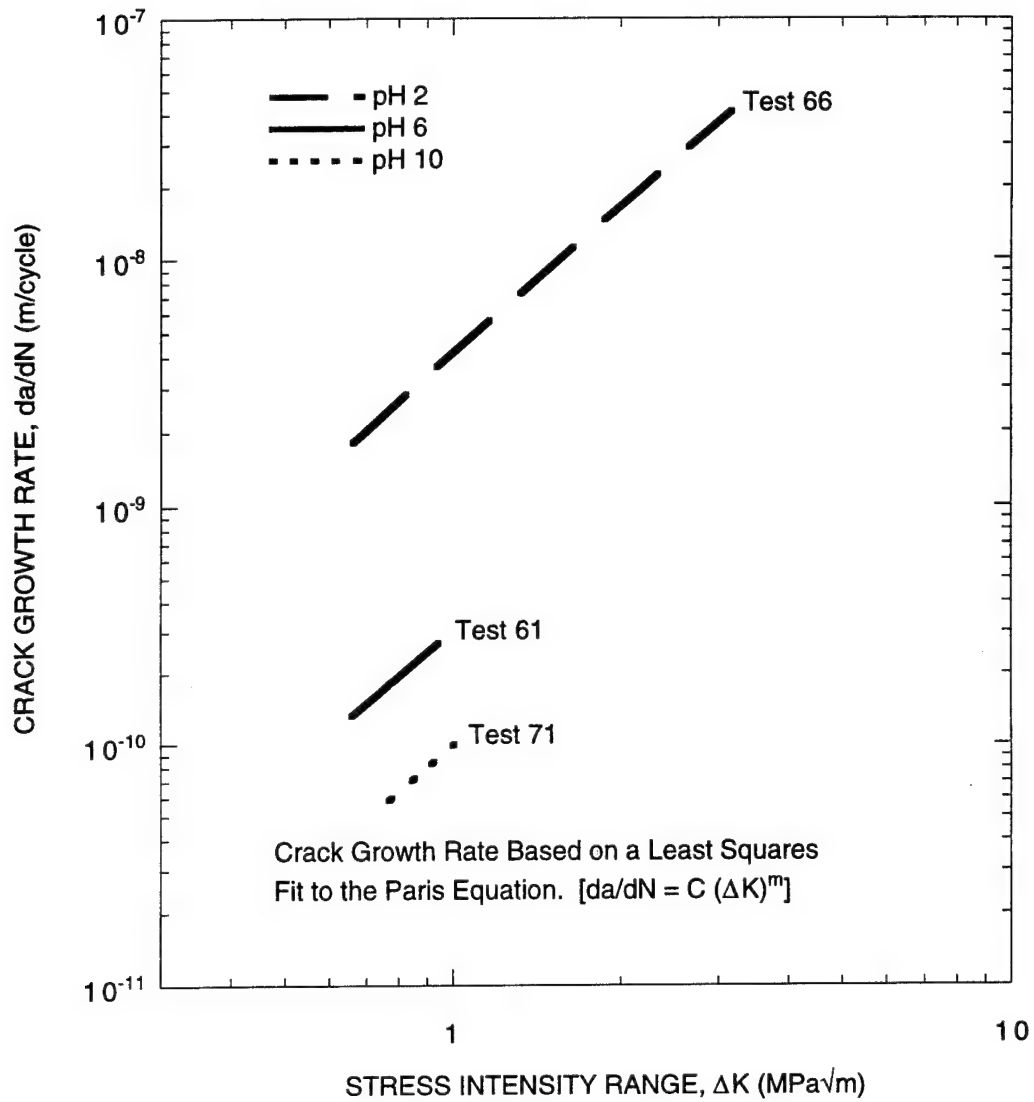
Figure 26. Effect of pH on the crack growth rate of small cracks in aircraft skin (Continued).



(c) Comparison of specimens in the vertical orientation in the as-received condition with a 30 μm polish on the through-thickness surfaces

CAM-5082-37

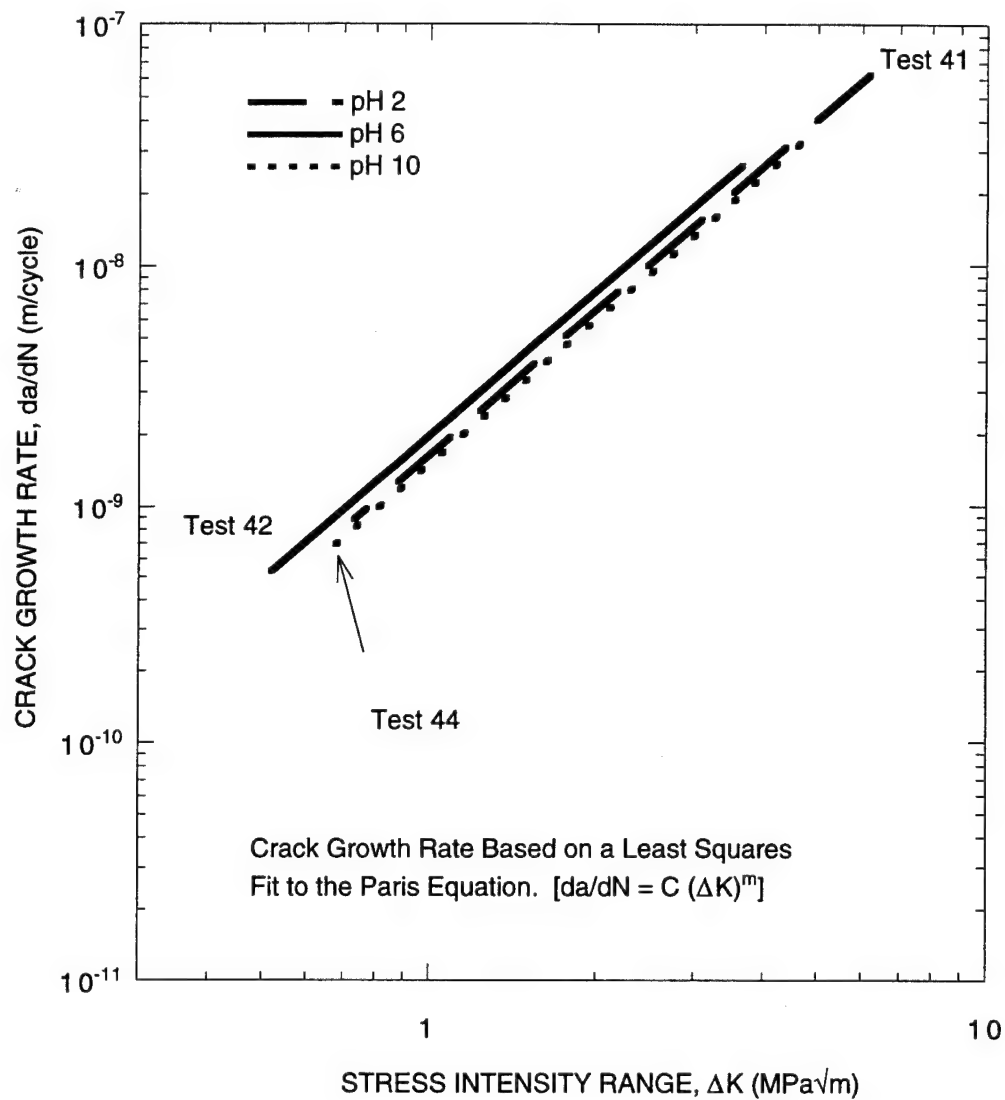
Figure 26. Effect of pH on the crack growth rate of small cracks in aircraft skin (Continued).



(d) Comparison of specimens in the horizontal orientation in the as-received condition with a 5 μm polish on the through-thickness surfaces

CAM-5082-38

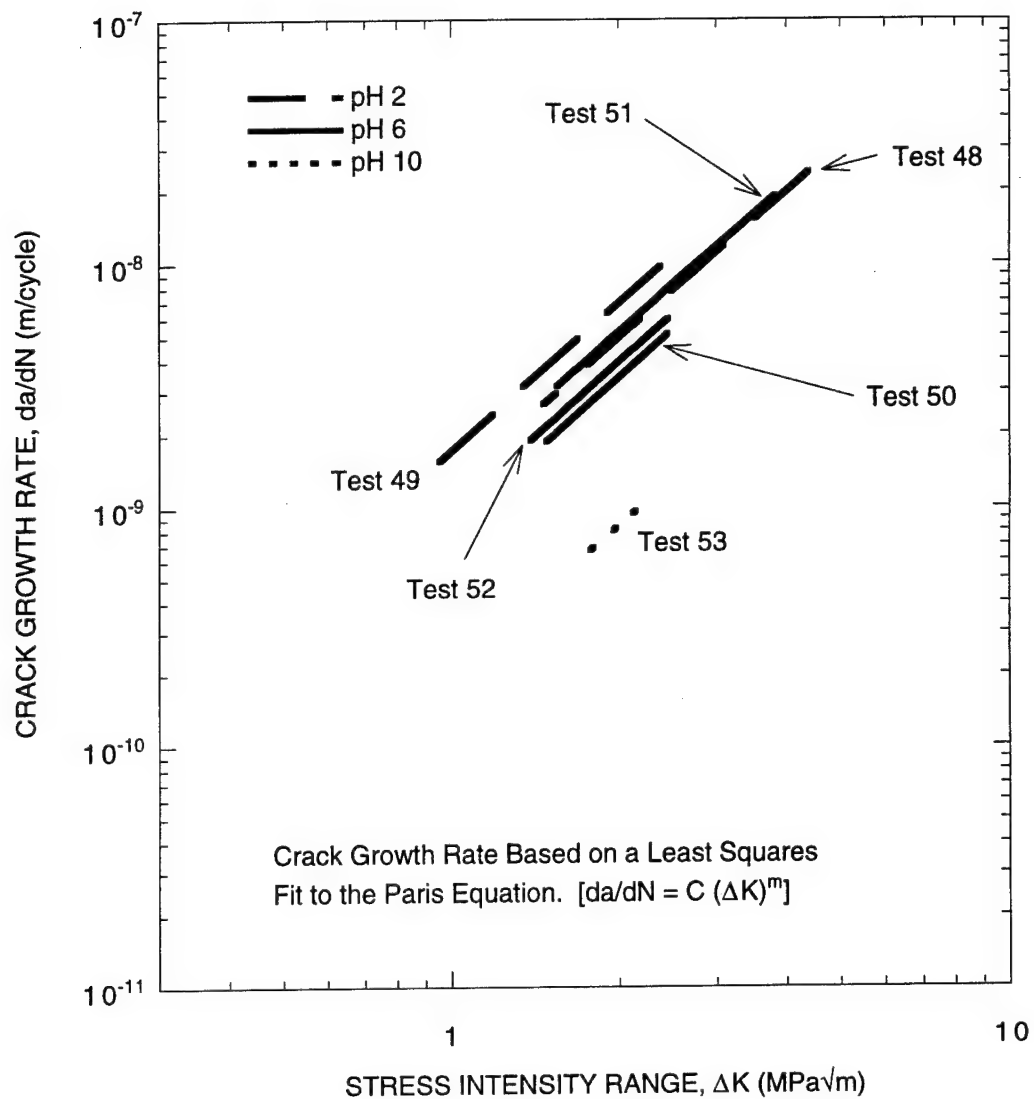
Figure 26. Effect of pH on the crack growth rate of small cracks in aircraft skin (Continued).



(e) Comparison of specimens in the horizontal orientation in the as-received condition with a 30 μm polish on the through-thickness surfaces

CAM-5082-39

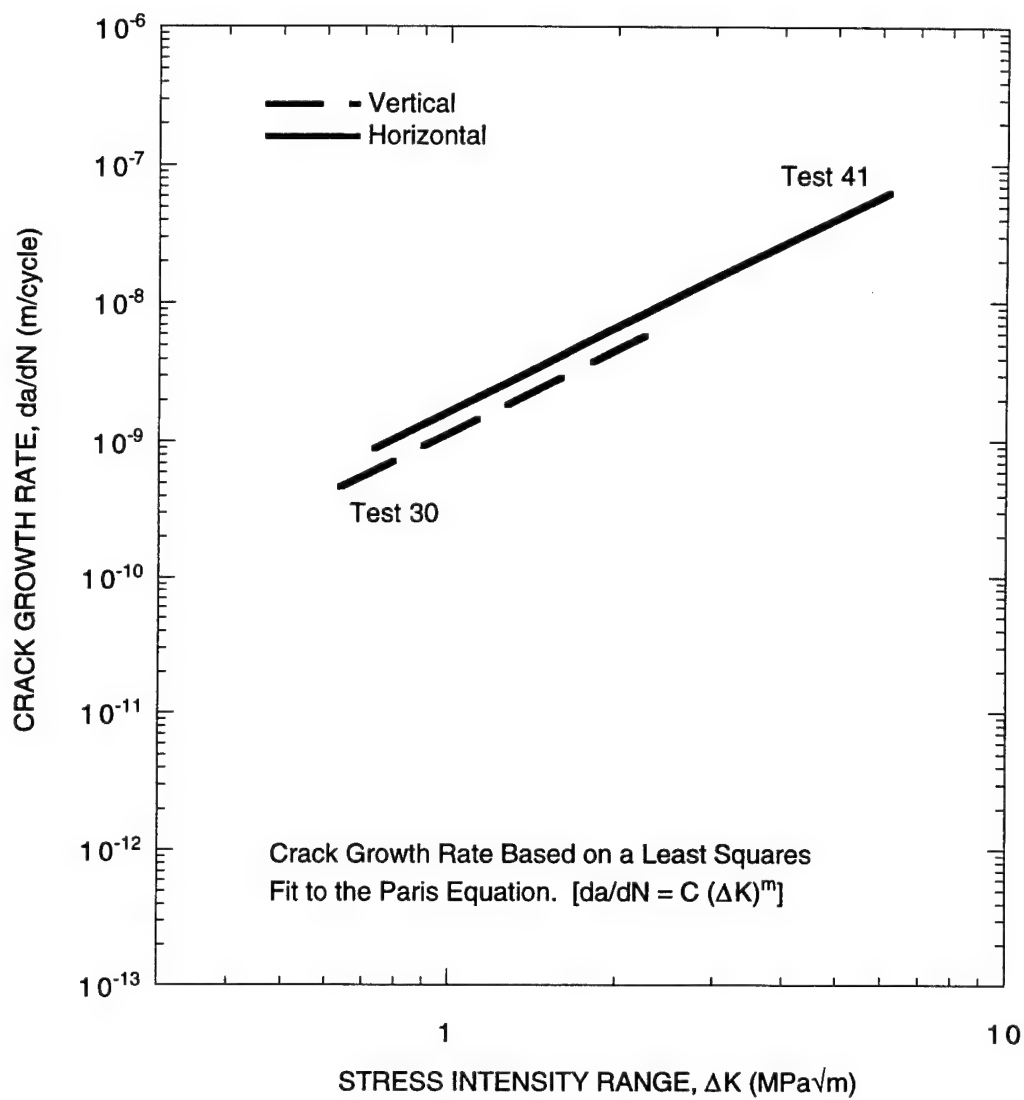
Figure 26. Effect of pH on the crack growth rate of small cracks in aircraft skin (Continued).



(f) Comparison of specimens in the horizontal orientation in the clad-only condition with a 30 μm polish on the through-thickness surfaces

CAM-5082-40

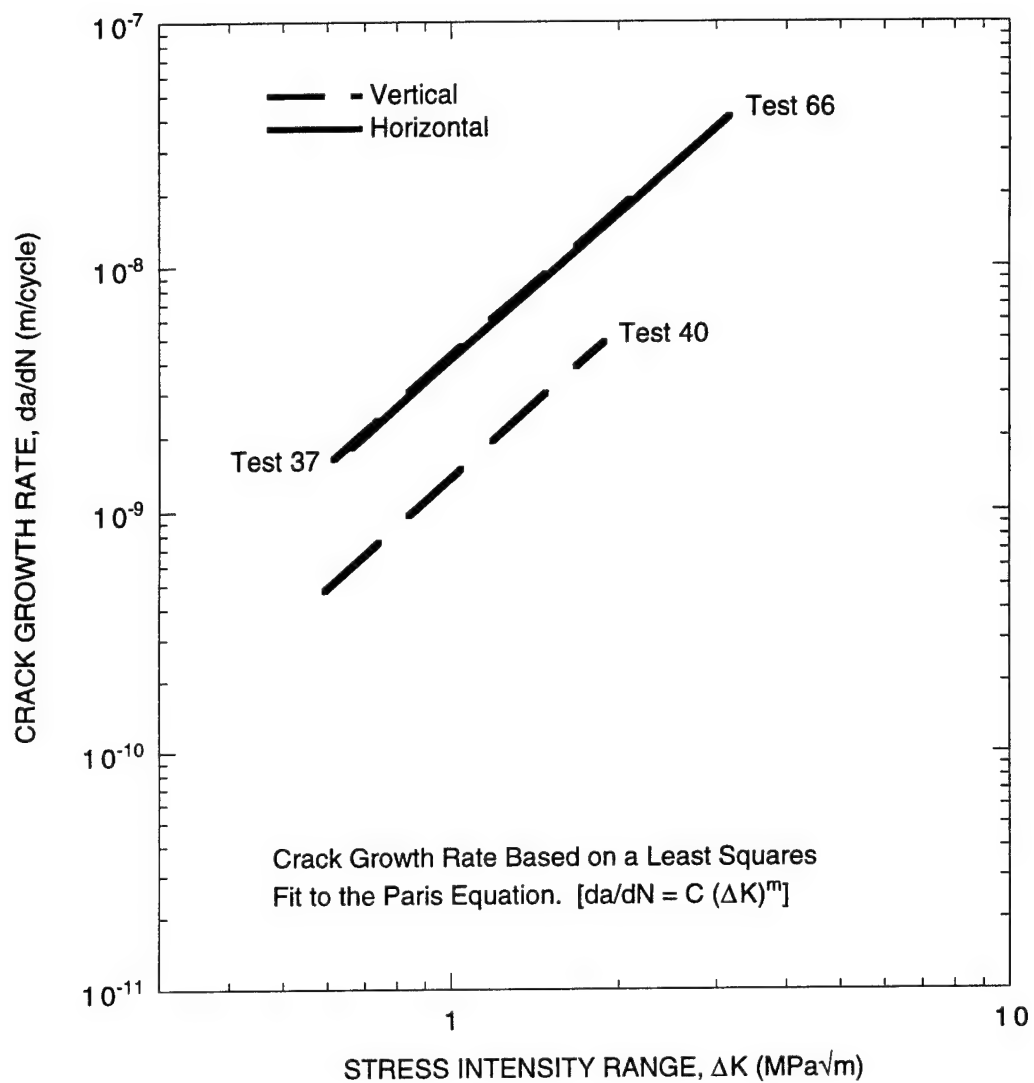
Figure 26. Effect of pH on the crack growth rate of small cracks in aircraft skin (Concluded).



(a) Comparison of specimens in the as-received condition with a 30 μm polish on the through-thickness surfaces in the pH 2 environment

CAM-5082-41

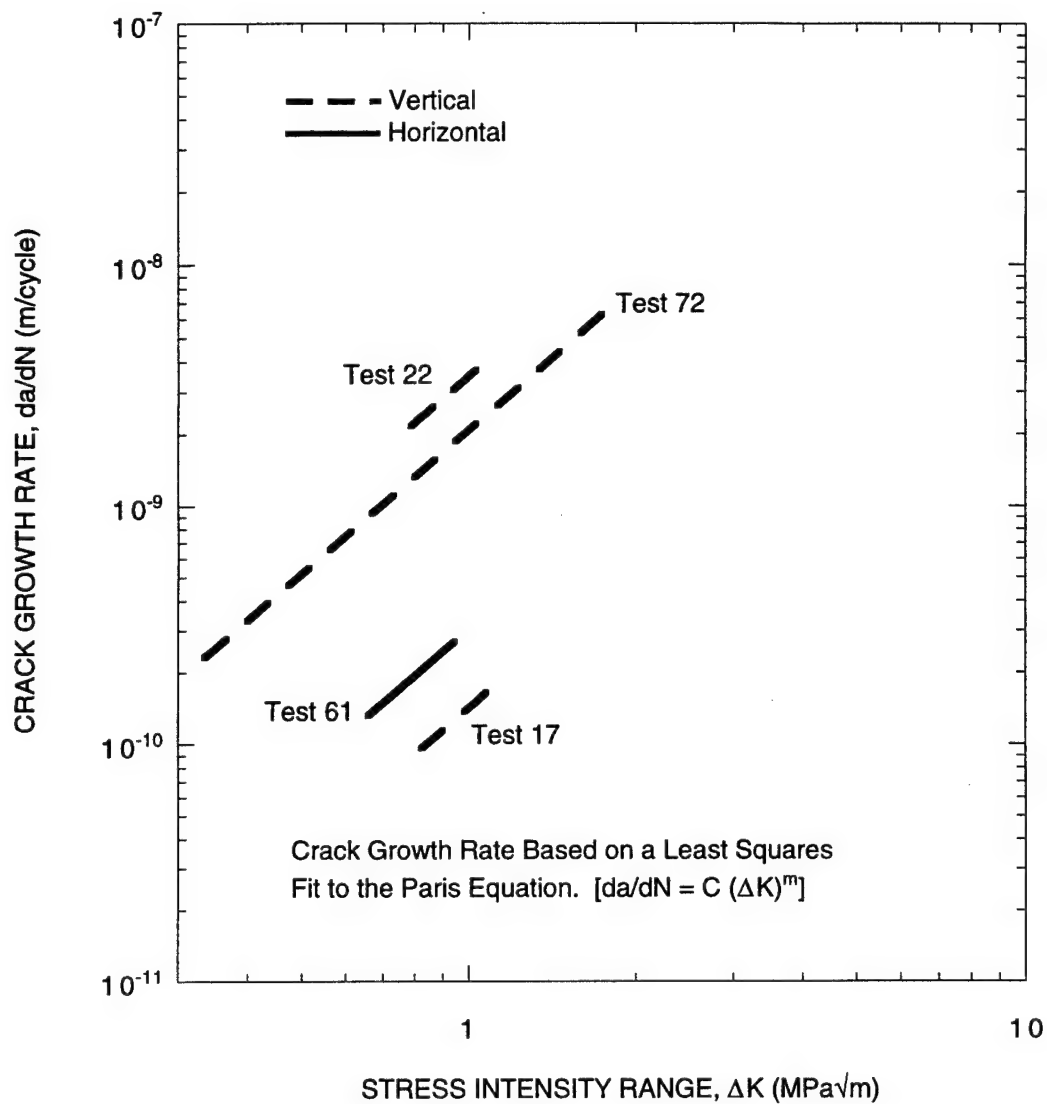
Figure 27. Effect of orientation on the crack growth rate of small cracks in aircraft skin.



(b) Comparison of specimens in the as-received condition with a 5 μ m polish on the through-thickness surfaces in the pH 2 environment

CAM-5082-42

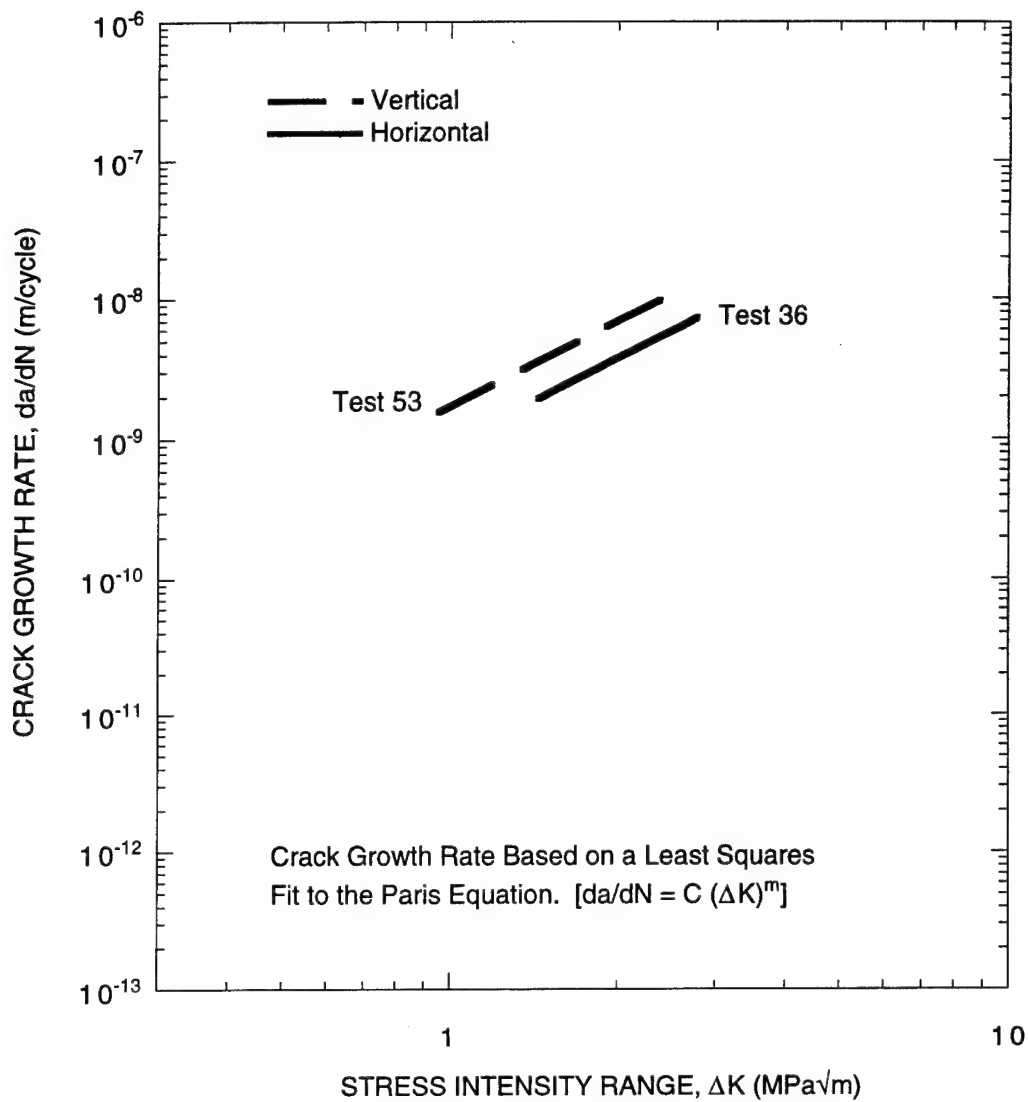
Figure 27. Effect of orientation on the crack growth rate of small cracks in aircraft skin (Continued).



(c) Comparison of specimens in the clad-only condition with a 5 μm polish on the through-thickness surfaces in the pH 6 environment

CAM-5082-43

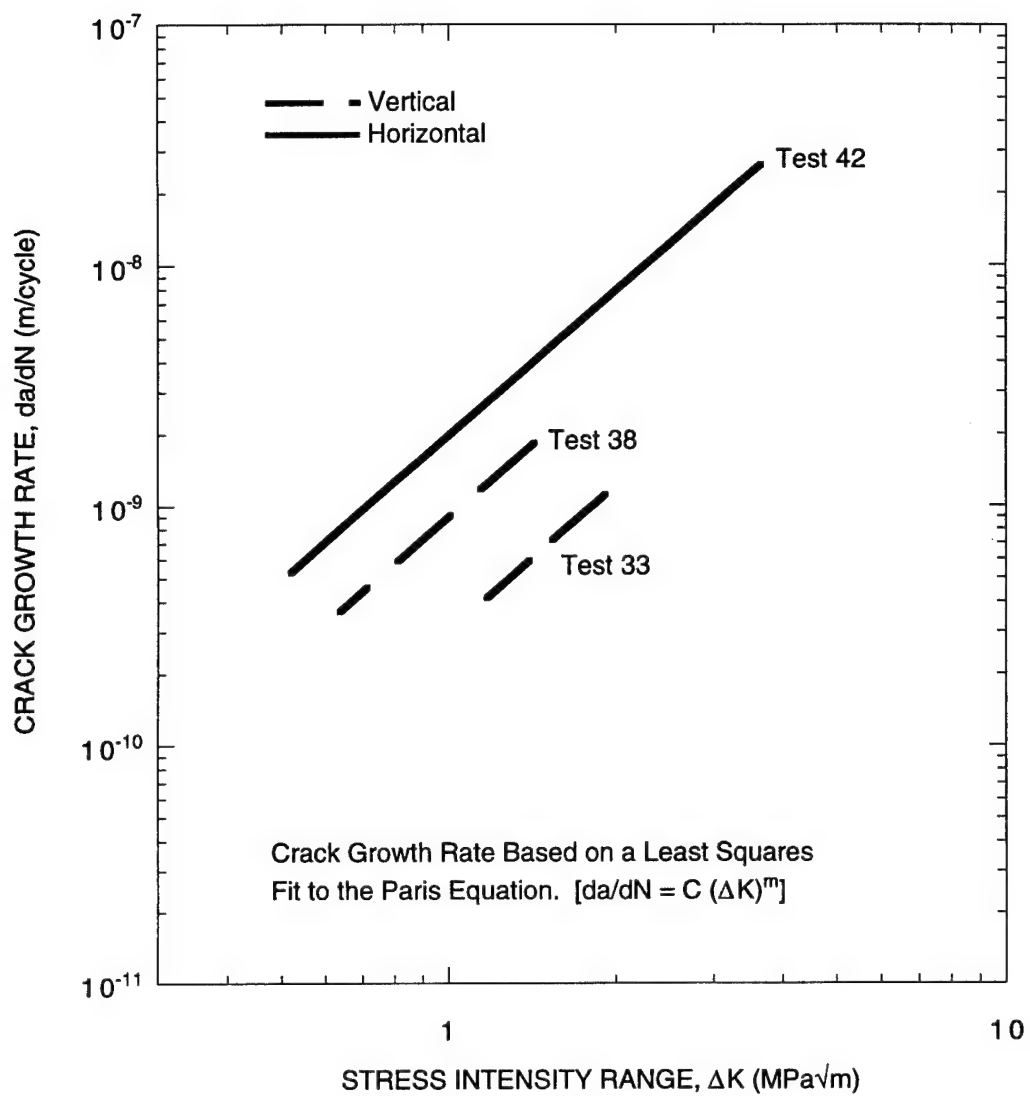
Figure 27. Effect of orientation on the crack growth rate of small cracks in aircraft skin (Continued).



(d) Comparison of specimens in the clad-only condition with a 30 μm polish on the through-thickness surfaces in the pH 2 environment

CAM-5082-44

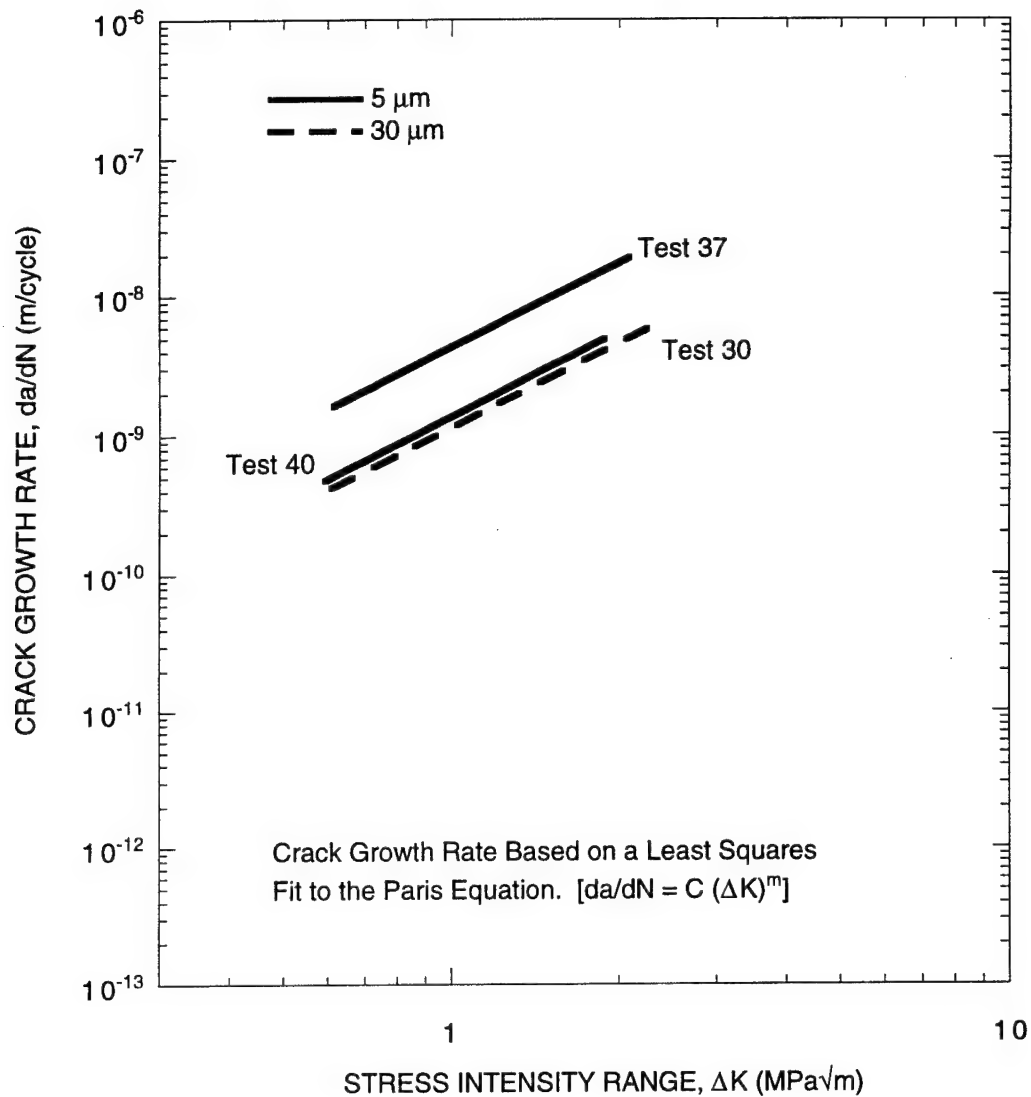
Figure 27. Effect of orientation on the crack growth rate of small cracks in aircraft skin (Continued).



(e) Comparison of specimens in the clad-only condition with a 30 μm polish on the through-thickness surfaces in the pH 6 environment

CAM-5082-45

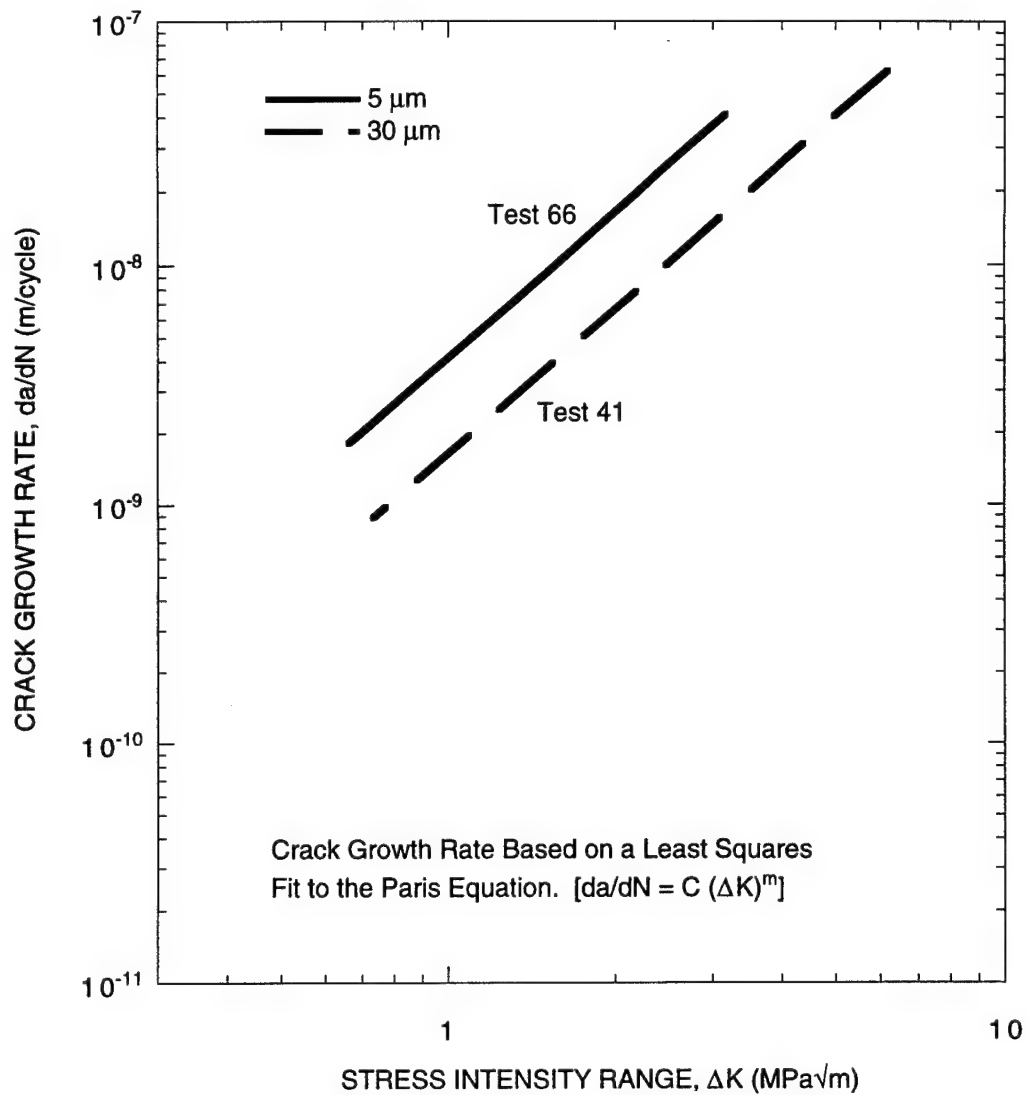
Figure 27. Effect of orientation on the crack growth rate of small cracks in aircraft skin (Concluded).



(a) Comparison of specimens in the as-received condition and in the vertical orientation in the pH 6 environment

CAM-5082-46

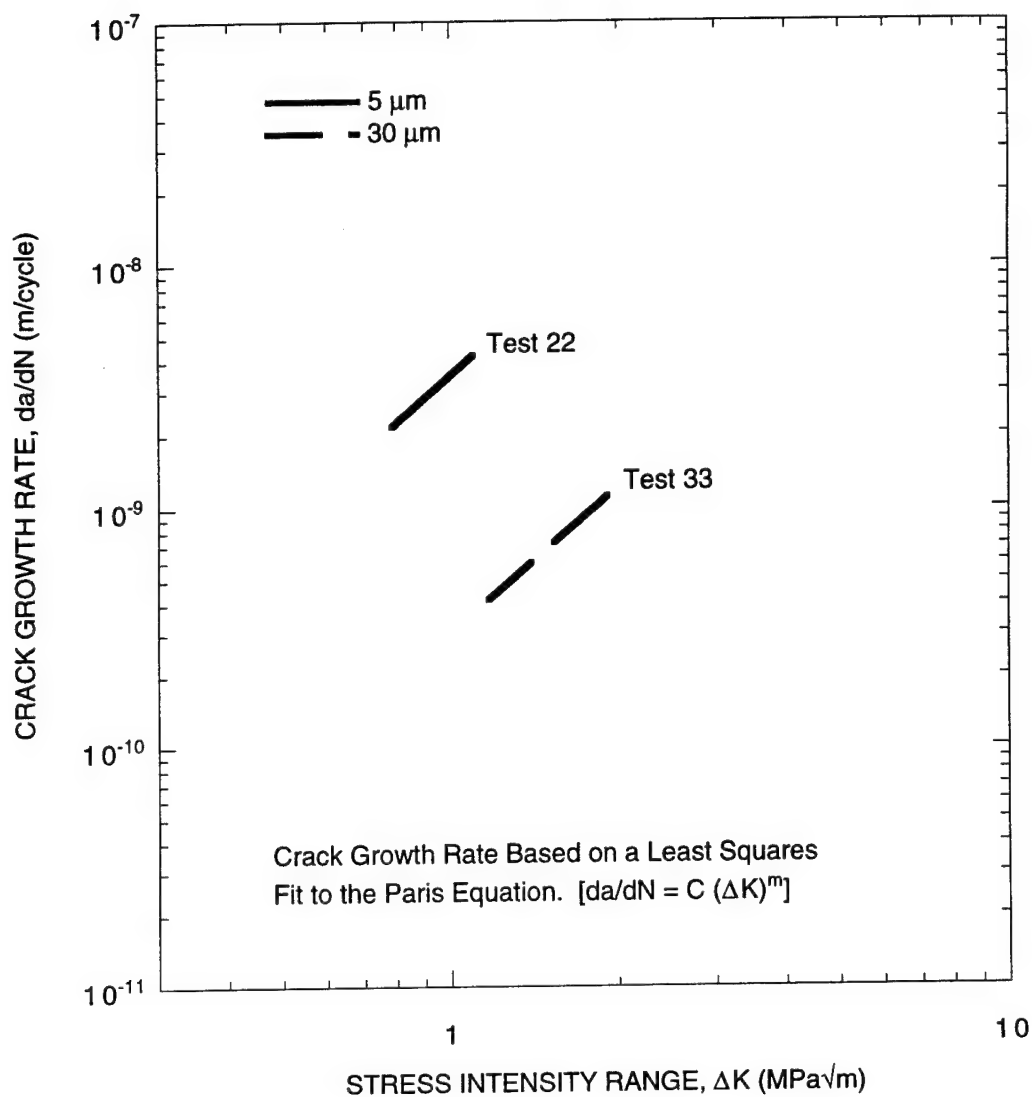
Figure 28. Effect of surface roughness on the crack growth rate of small cracks in aircraft skin.



(b) Comparison of specimens in the as-received condition and in the horizontal orientation in the pH 2 environment

CAM-5082-47

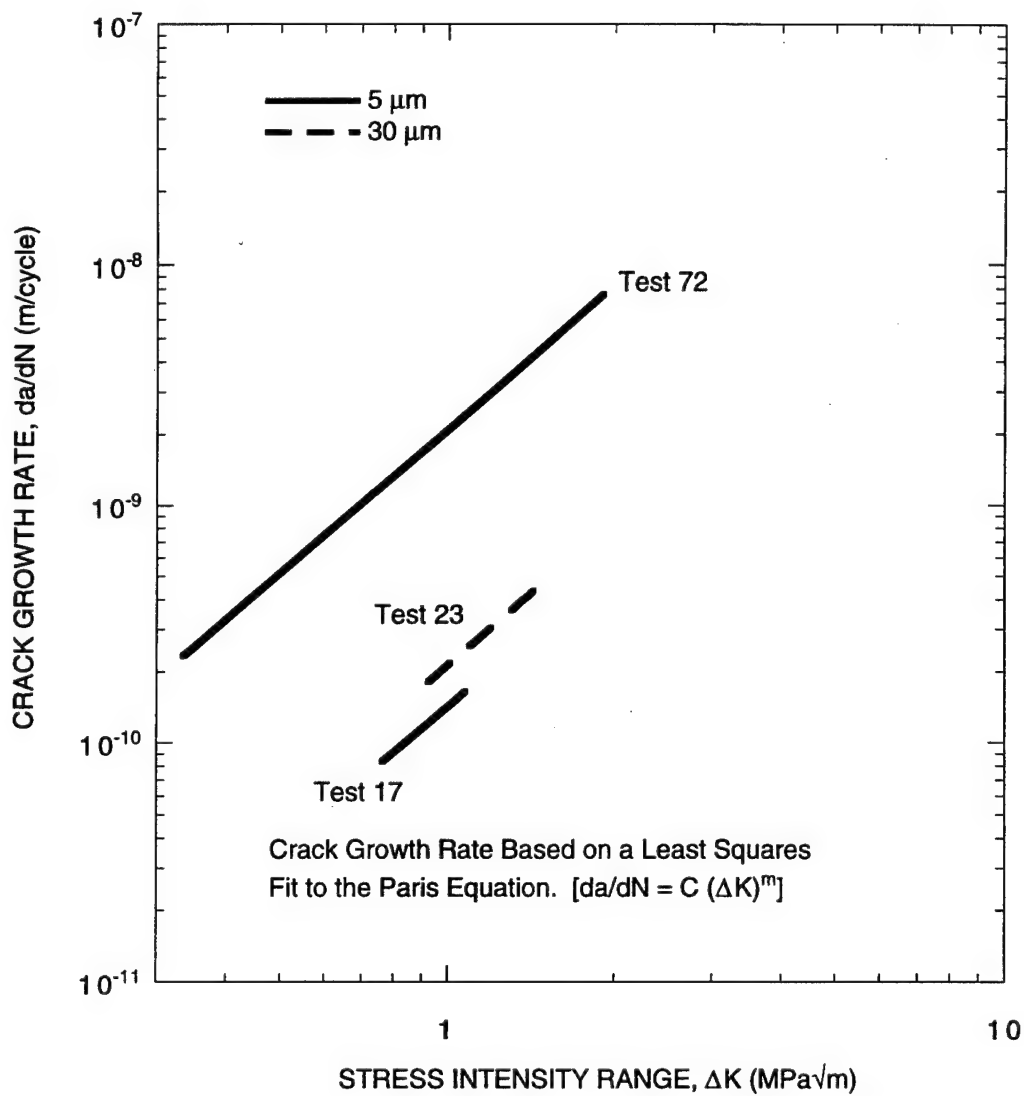
Figure 28. Effect of surface roughness on the crack growth rate of small cracks in aircraft skin (Continued).



(c) Comparison of specimens in the as-received condition and in the vertical orientation in the pH 6 environment

CAM-5082-48

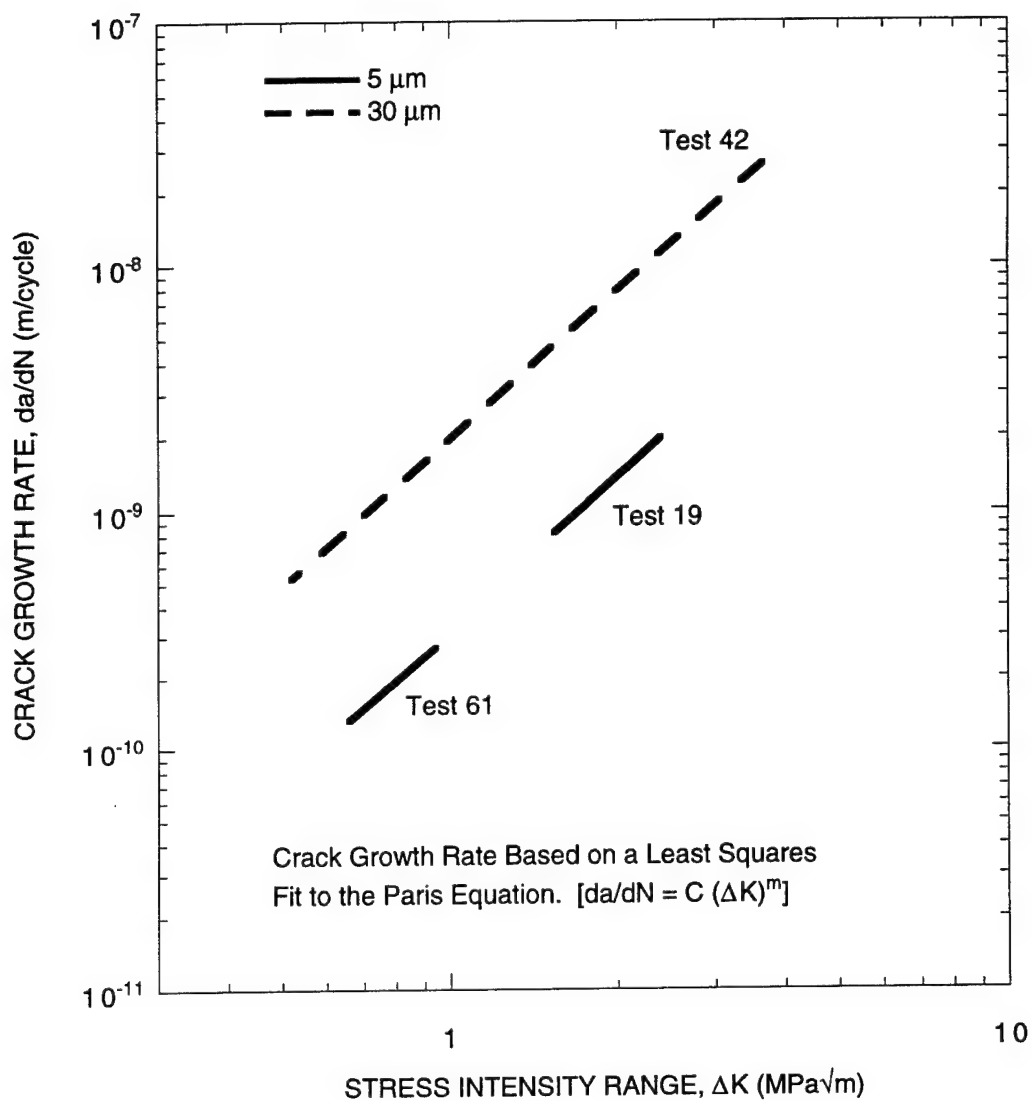
Figure 28. Effect of surface roughness on the crack growth rate of small cracks in aircraft skin (Continued).



(d) Comparison of specimens in the clad-only condition and in the vertical orientation in the pH 6 environment

CAM-5082-49

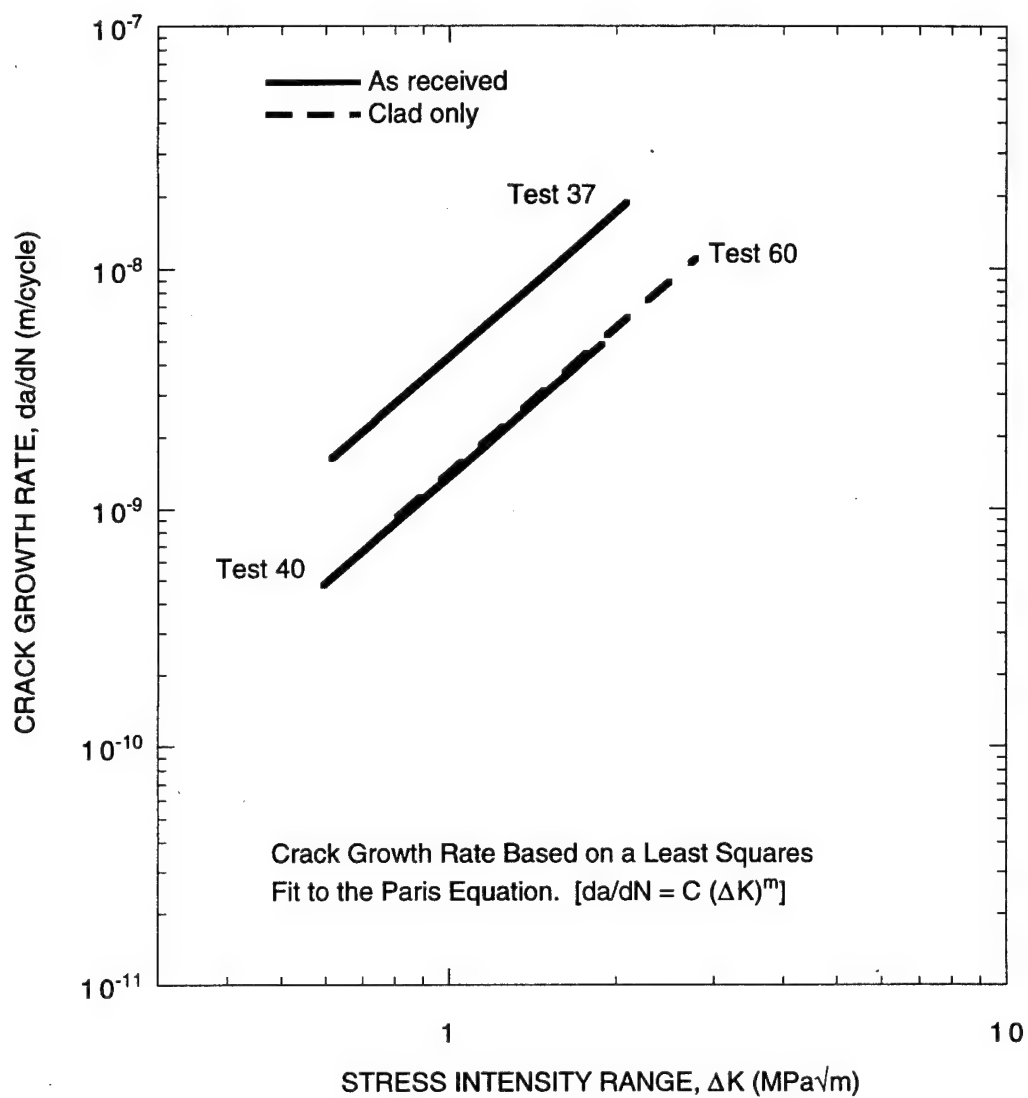
Figure 28. Effect of surface roughness on the crack growth rate of small cracks in aircraft skin (Continued).



(e) Comparison of specimens in the as-received condition and in the horizontal orientation in the pH 6 environment

CAM-5082-50

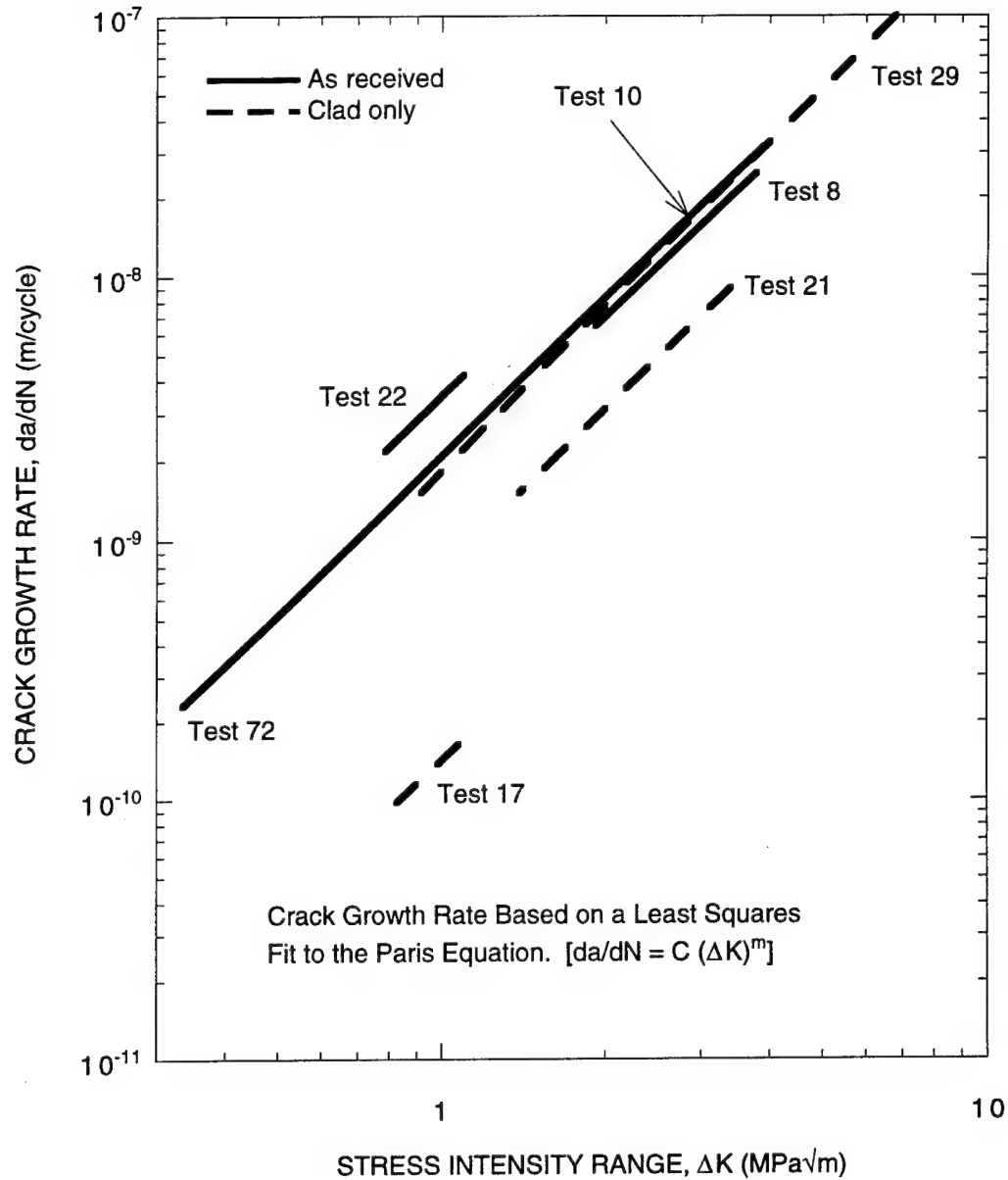
Figure 28. Effect of surface roughness on the crack growth rate of small cracks in aircraft skin (Concluded).



(a) Comparison of specimens in the vertical orientation with a 5 μm polish on the through-thickness surfaces in the pH 2 environment

CAM-5082-51

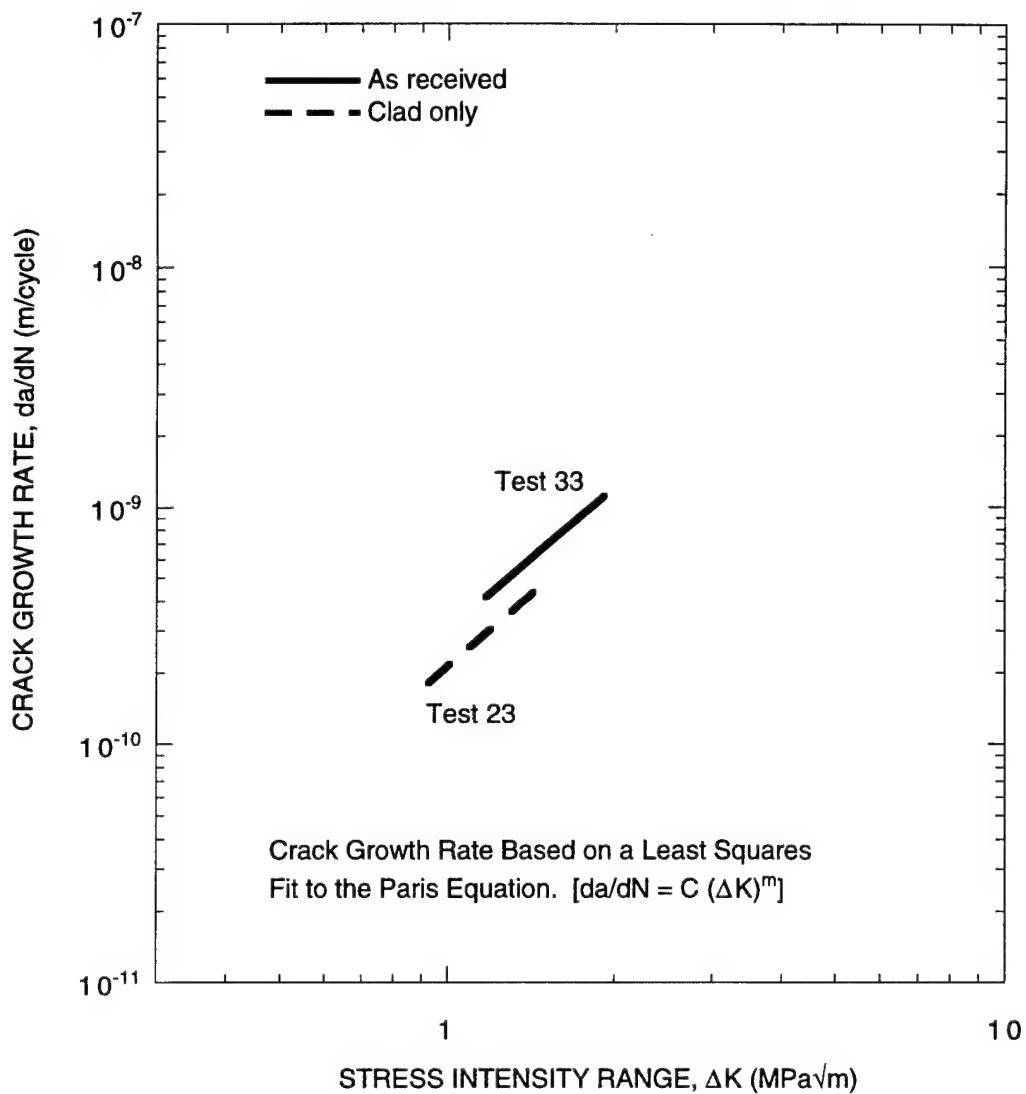
Figure 29. Effect of surface coating on the crack growth rate of small cracks in aircraft skin.



(b) Comparison of specimens in the vertical orientation with a 5 μ m polish on the through-thickness surfaces in the pH 6 environment

CAM-5082-52

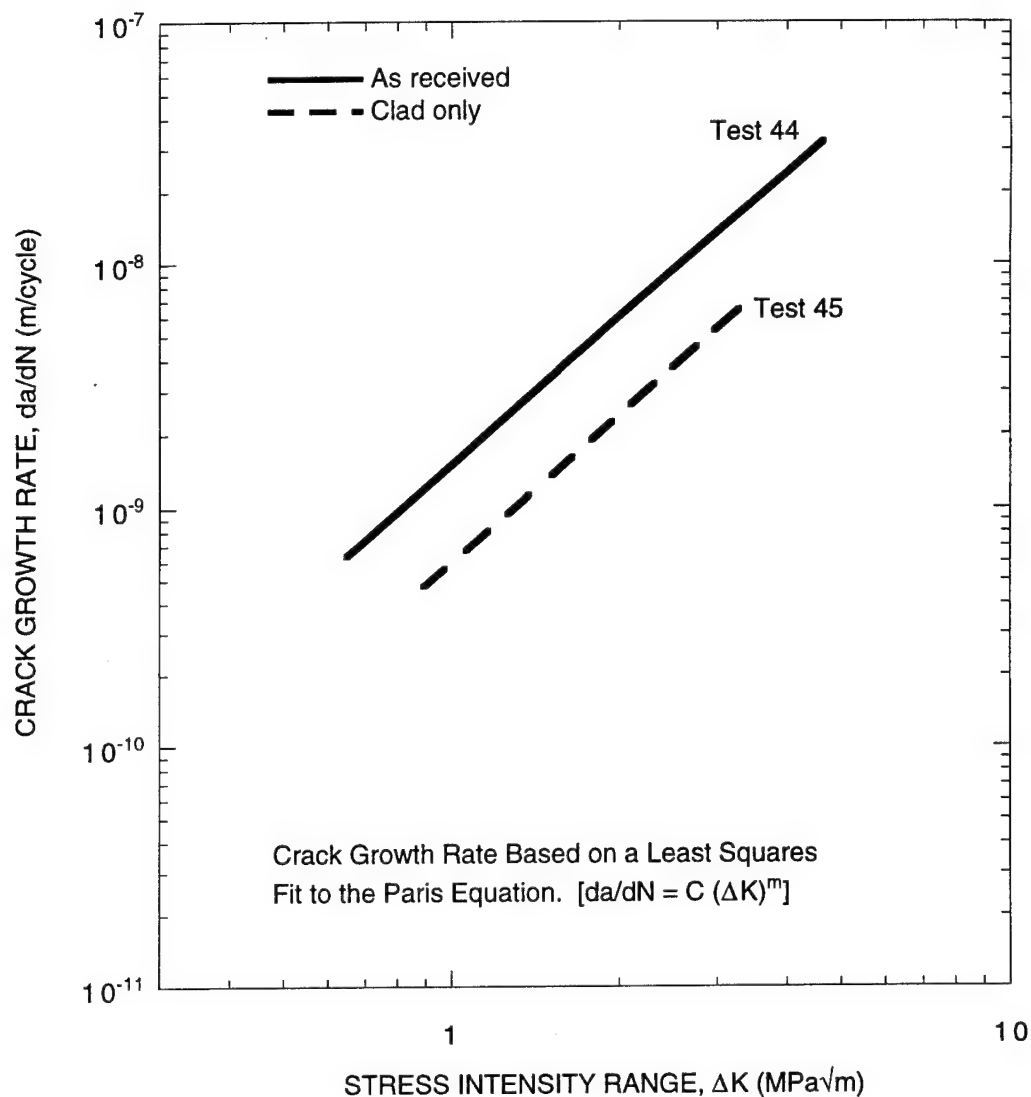
Figure 29. Effect of surface coating on the crack growth rate of small cracks in aircraft skin (Continued).



(c) Comparison of specimens in the vertical orientation with a 30 μm polish on the through-thickness surfaces in the pH 6 environment

CAM-5082-53

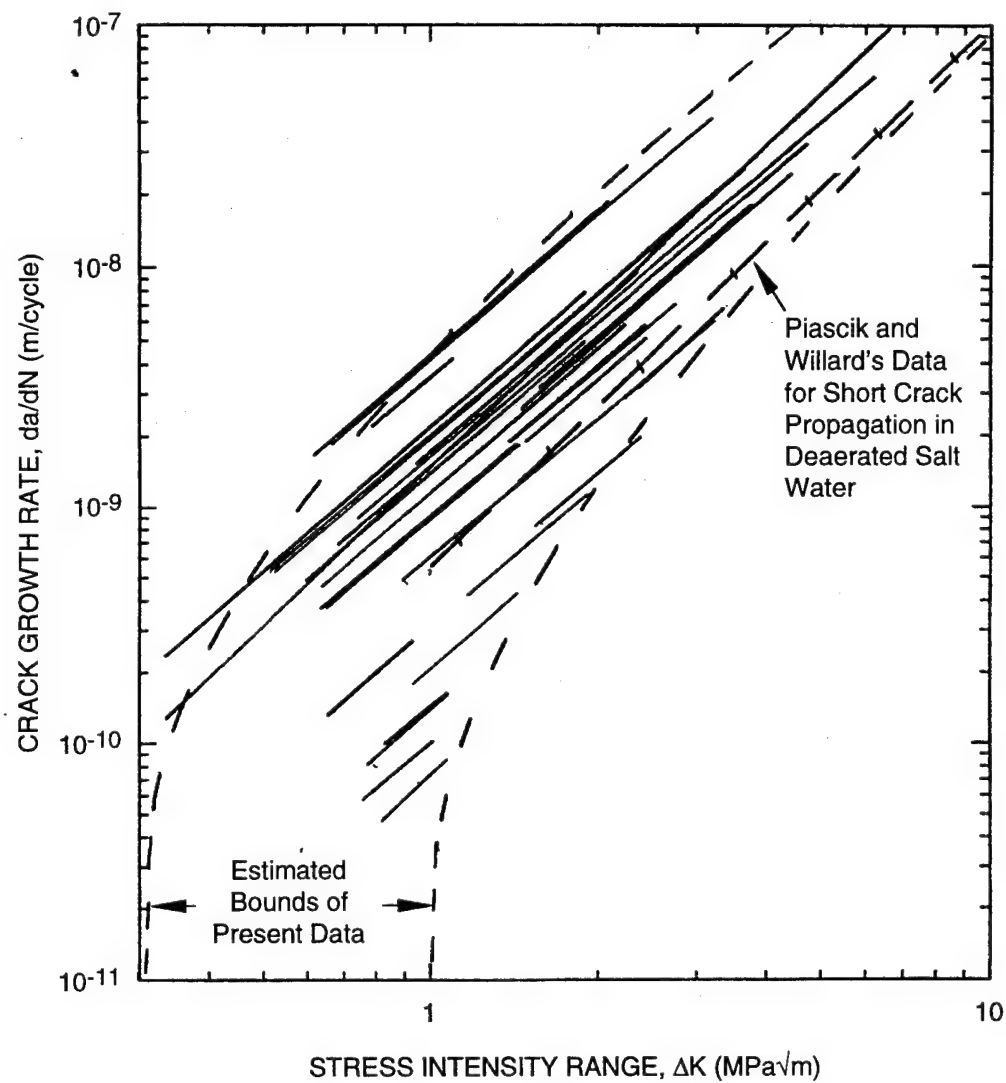
Figure 29. Effect of surface coating on the crack growth rate of small cracks in aircraft skin (Continued).



(d) Comparison of specimens in the horizontal orientation with a 30 μm polish on the through-thickness surfaces in the pH 10 environment

CAM-5082-54

Figure 29. Effect of surface coating on the crack growth rate of small cracks in aircraft skin (Concluded).



CM-5082-55

Figure 30. Crack growth rate trends of all corrosion-fatigue tests performed on aircraft skin material in salt water.

Table 8

**STATISTICAL ANALYSIS OF THE CRACK GROWTH RATE
DETERMINED FROM THE CORROSION-FATIGUE SPECIMENS^a**

		1 Log (pH)	2 Orientation	3 Log (Roughness)	4 Coating	5 Log (Maximum Stress)
B_i	-10.3500	-0.7682	-0.0355	-0.0669	0.3046	0.9287
SE_i	1.2219	0.2729	0.1596	0.3852	0.1652	0.6464
$SE_{da/dN}$	0.3783					
SS_{reg}	1.7683					
SS_{resid}	3.4339					
df	24					
$ t_i $		2.82	0.22	0.17	1.84	1.44
$ t_i > t_{\alpha/2}$ $t_{\alpha/2} = 1.71$		yes	no	no	yes	no
r^2	0.34					
F	2.47					
$F > F_{crit}$ $F_{crit} = 2.62$	no					

^a $\log(da/dN) = B_0 + B_1 X_1 + B_2 X_2 + B_3 X_3 + B_4 X_4 + B_5 X_5$, where da/dN = crack growth rate at $\Delta K = 1 \text{ MPa}\sqrt{\text{m}}$, B_i are coefficients, and X_i are the following independent variables.

$X_1 = \log(\text{pH})$

$X_2 = \text{orientation such that } 0 = \text{horizontal and } 1 = \text{vertical}$

$X_3 = \log(\text{roughness in micrometers})$; note: $30 \mu\text{m finish} = 0.8 \mu\text{m}$, $5 \mu\text{m finish} = 0.3 \mu\text{m}$, $0.5 \mu\text{m finish} = 0.2 \mu\text{m}$, as-machined finish is not included in the analysis

$X_4 = \text{coating such that } 0 = \text{clad only and } 1 = \text{as received}$

$X_5 = \log(\text{maximum stress in MPa})$.

SE_i is the standard error for B_i , $SE_{da/dN}$ is the standard error for da/dN , SS_{reg} is the regression sum of squares, SS_{resid} is the residual sum of squares, and df is the degrees of freedom.

t_i is the t-statistic value for B_i , and $t_{\alpha/2}$ is the t-statistic value for a level of significance of 0.05.

If $|t_i| > t_{\alpha/2}$, then the coefficient is statistically significant to a level of 0.05.

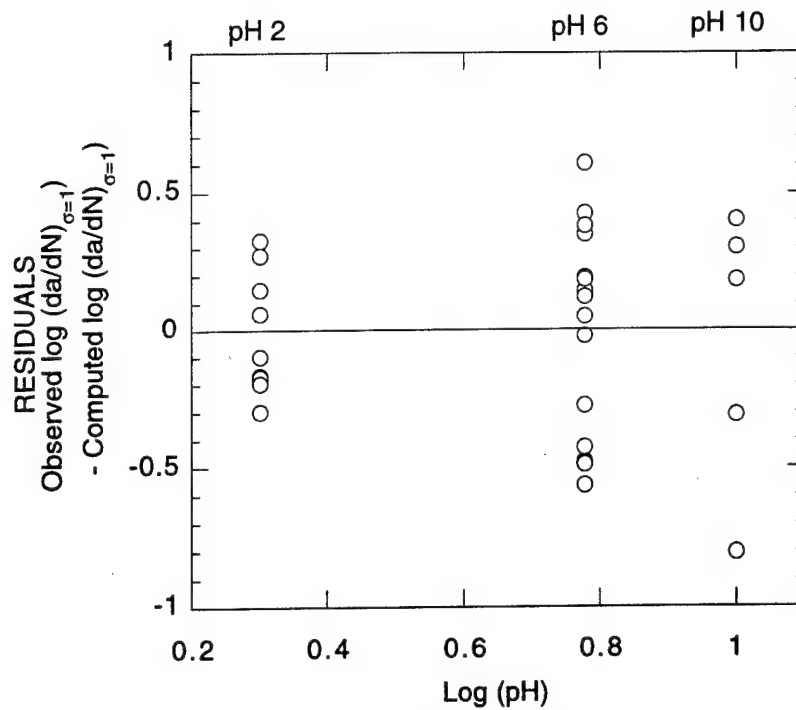
r^2 is the coefficient of determination such that 1 indicates a perfect correlation and 0 indicates that the equation is not helpful in predicting fatigue life.

F determines whether the observed relationship between da/dN and the independent variables occurs by chance. If $F > F_{crit}$, the regression equation is useful for prediction to a level of significance of 0.05.

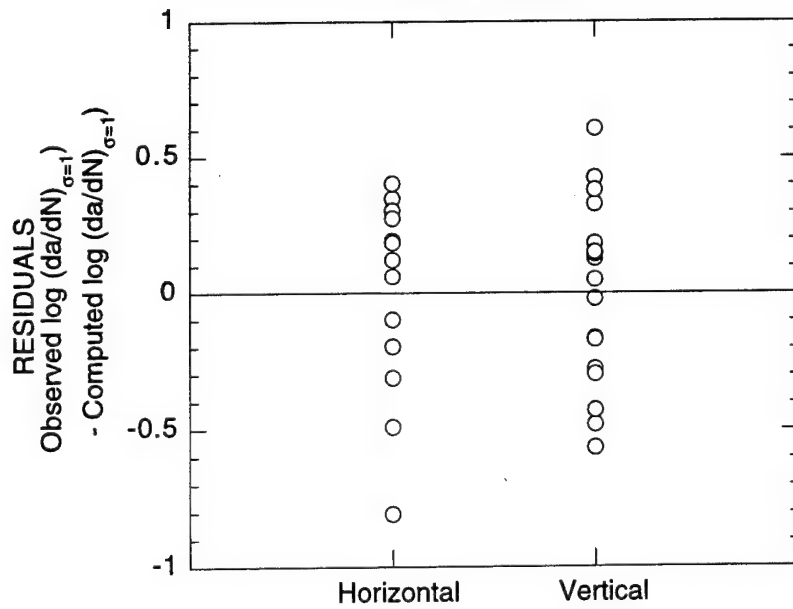
used in the crack propagation analysis does not treat the pH 2 and pH 10 environments as a single class. This approach was taken because the behavior of each environment in the test-by-test examination of the data suggests its suitability and because a better correlation was obtained in this manner.

The correlation shown in table 8 falls slightly below a 0.05 level of significance for the correlation as a whole, indicating that there is considerable scatter in the data and that there is a generally low level of significance to the trends expressed by the correlation. Nevertheless, the level of significance for the observed effect of pH and coating reached the 0.05 level, according to the t-statistic. The effect of stress nearly reached the 0.05 level of significance. The sense of the coefficients for pH, coating, and stress accurately reflect the trends observed in the test-by-test comparison: (1) the crack growth rate increases as the pH decreases, (2) the as received condition produces a higher crack growth rate than the clad only condition, and (3) the crack growth rate is more sensitive to the stress than the fits to the Paris Equation allow. The t-statistic indicates that the level of significance for the effect of orientation and roughness is significantly below the other parameters. The low level of significance of these parameters is consistent with the uncertain trends observed in the test-by-test comparisons. Figure 31 shows plots of the residuals as a function of each independent variable and reveals no apparent biases. This suggests that the assumptions in formulating the analysis have produced evenly distributed errors that are not biased.

Explanations for the observed effects of the test variable on the crack growth rate are as follows. Acceleration of stress corrosion cracking and corrosion fatigue propagation rates of aluminum alloys in acidic salt solutions has often been observed. That acceleration has been attributed by Sedricks et al.²⁵ to more rapid crack tip dissolution resulting from an enhanced cathodic reaction (i.e., hydrogen reduction). The effect of pH has been observed to decline as a crack lengthens due to local acidification of the crack tip from metal ion hydrolysis. In the case of Sedricks et al., the difference between pH 1 and pH 6 salt environments on the crack growth rate of an Al-Zn-Mg alloy disappeared by the time cracks reached a length of 1 mm. In alkaline solutions, the experimental observations are mixed. In 7XXX series alloys, a gradual increase in stress corrosion cracking resistance has been reported by McHardy and Hollingsworth²⁶ from pH 6 to pH 10, which is followed by a rapid increase at higher pH values. On the other hand, de Jong²⁷ reported stress corrosion cracking rates that nearly followed the trends in corrosion product solubility: a minimum in crack growth rate at pH 6-7, where corrosion product solubility is low, and an increase in crack growth at higher and lower pH values, where solubility is high.



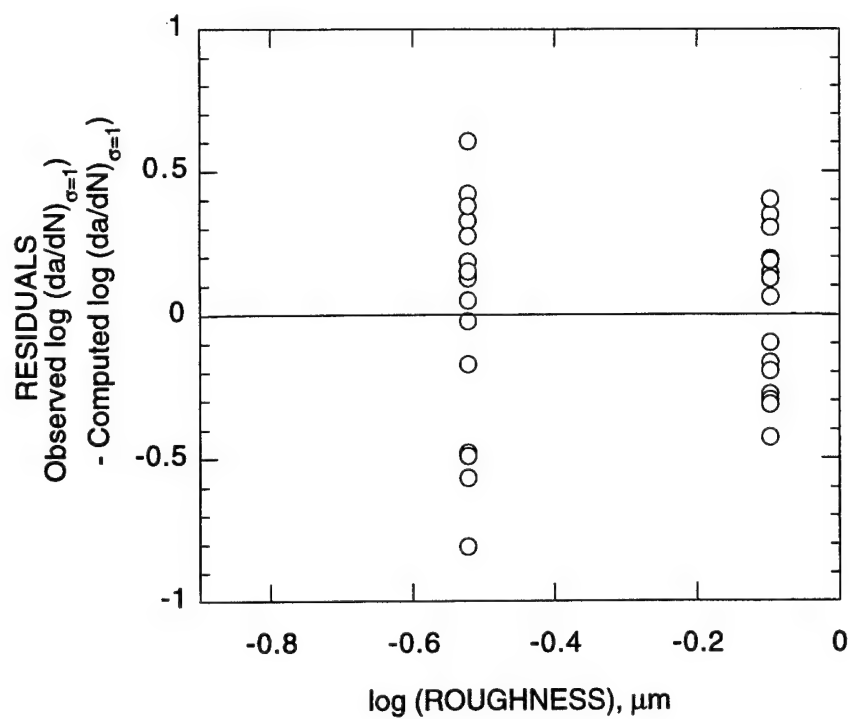
(a) pH residuals



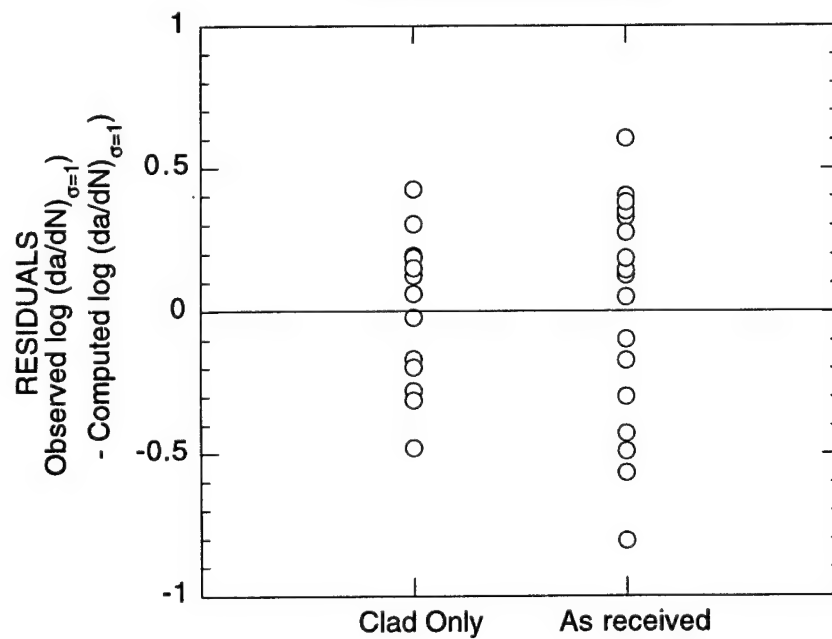
(b) Orientation residuals

CAM-5082-56

Figure 31. Residuals for crack propagation analysis.



(c) Roughness residuals



(d) Coating residuals

CAM-5082-57

Figure 31. Residuals for crack propagation analysis (Concluded).

The present results are consistent with the observed increase in crack growth rate in acidic solutions reported by Sedricks et al. and with the modest reduction in crack growth rate observed by McHardy and Hollingsworth in alkaline solutions. Holroyd²⁸ has indicated that the role of corrosion product solubility has yet to be firmly established.

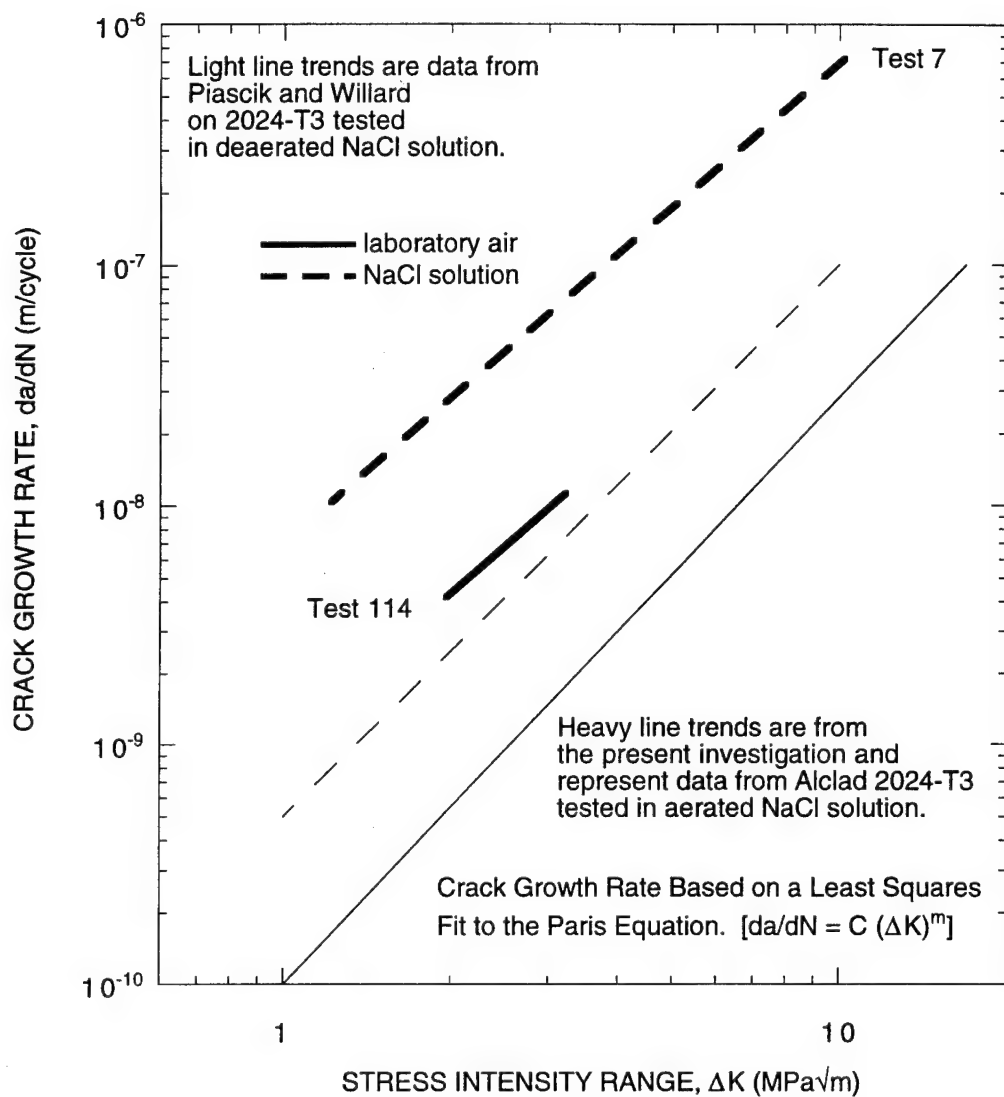
The mixed effect of orientation reflects the lack of any directional microstructural features. As indicated in the discussion on crack nucleation kinetics, the only directional characteristic observed was a surface streak pattern from rolling that might have had a small effect on crack nucleation, but apparently does not have a consistent effect on crack propagation.

The lack of an effect on crack growth rate due to the roughness of the 5- μm and 30- μm surfaces is expected. There is no compelling reason to expect a significant effect on crack propagation from the small differences in roughness of these surfaces (i.e., 0.8- μm and 0.3- μm surface feature heights for the 30- μm and 5- μm finishes, respectively).

The differences in crack growth rate between clad only and as received material might be because the paint layer partially obstructs the crack mouth opening of a corner crack. A crack that nucleates on a corner of the gage length will have half the crack mouth under the paint layer in an as received specimen. This could enhance the development of an occluded (i.e., acidic) environment within the crack and thereby increase the crack propagation rate.

Finally, in figure 30, we compare the range of corrosion fatigue crack growth rates in pH 6 salt water solutions from the present investigation and the result from similar tests reported by Piascik and Willard.⁷ In figure 32, a comparison is made between test results from laboratory air and salt water environments for both investigations. The results of Piascik and Willard and the results from the present study show crack growth rates with a similar dependence on ΔK . However, the results from tests of Piascik and Willard are on the lower bound of the present data. The relatively low crack growth rates in their data could be a result of differences in environment (Piascik and Willard used a deaerated solution, whereas we used an aerated solution) or differences in test material (Piascik and Willard used 2024-T3, whereas our crack growth measurements reflect the crack growth rate in the Alclad layer on 2024-T3).

In figure 32, we also compare the effect of fatigue crack growth rates in air and in salt water solutions. The magnitude of the acceleration in the crack growth rate in the salt water solutions (about a factor of 5) was the same in our investigation and in the investigation of Piascik and Willard. Thus, the crack growth rates in salt water solutions reflect a substantial environmental acceleration.



CAM-5082-58

Figure 32. Comparison of corrosion-fatigue crack growth rates in laboratory air and NaCl solutions.

The appearance of corrosion-fatigue crack damage can generally be divided into two categories: (1) cracks nucleating at constituent particles in the 2024-T3 core material and (2) crystallographic cracks nucleating in the edges of the clad. Cracks in the first category were rarely observed in clad only or as received material; a finding that has been observed by others.^{22,23} Figure 33 shows a crack that nucleated from a pit. In this case, the pit appears to be slightly wider ($\sim 40\ \mu\text{m}$) than it is deep ($\sim 30\ \mu\text{m}$) and has undercut the surface to a small degree. Immediately ahead of the pit are cleavage fracture features. The region in front of the cleavage fracture is surrounded by a region of cleavage interspersed with tear ridges. Eventually, a fracture area in the shape of a parabolic segment develops for which the crack depth ($\sim 300\ \mu\text{m}$) is slightly greater than the width ($\sim 250\ \mu\text{m}$).

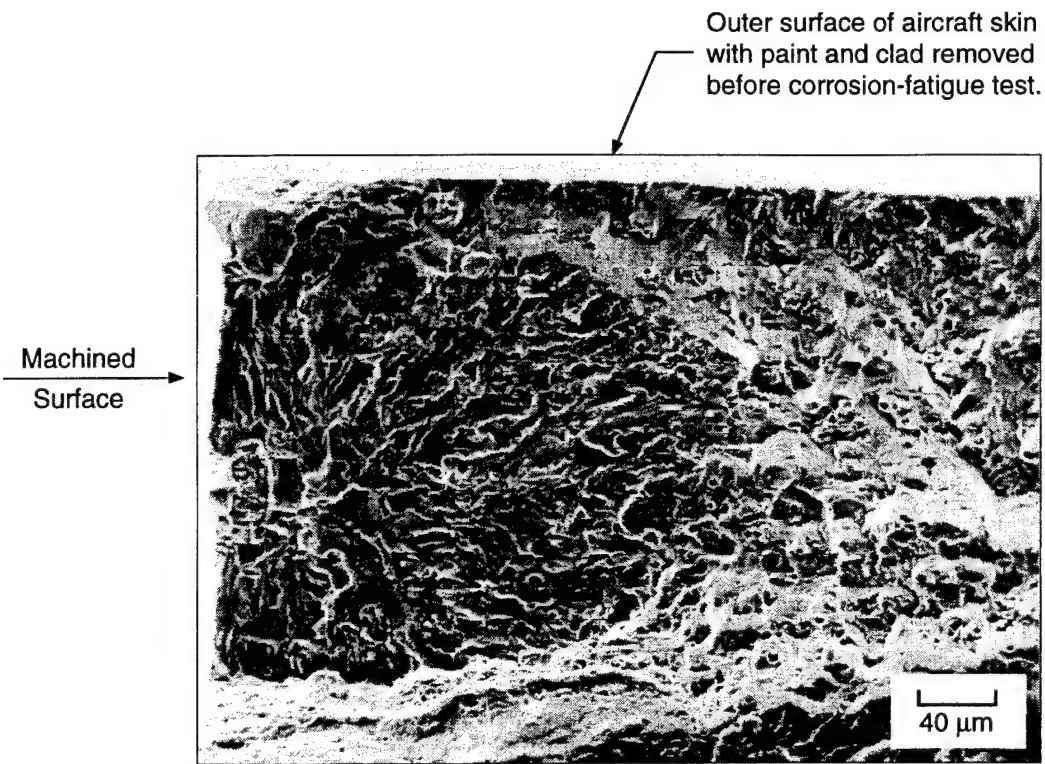
In clad specimens, cracking nucleated in the clad and not in the core material. In some cases, crack nucleation occurred at or near crystallographic pit colonies (see figure 17). Figure 34 shows a crystallographic crack face that appears to have nucleated at a colony of crystallographic pits. Once the crack was about $40\ \mu\text{m}$ deep, the fracture mode changed to ductile ridges separating plateaus that radiate from the nucleation site. The mode of fracture changed once again to large ductile void coalescence when the crack radius reached about $120\ \mu\text{m}$.

The first two fracture modes (commonly called Stage I and Stage II) are often observed in aluminum and aluminum alloys subjected to fatigue loading,²⁹ whether that loading occurs in an aggressive medium or in a vacuum. Exacerbation of this kind of fracture feature by aggressive media has been observed by other investigators,³⁰ as well as by us.

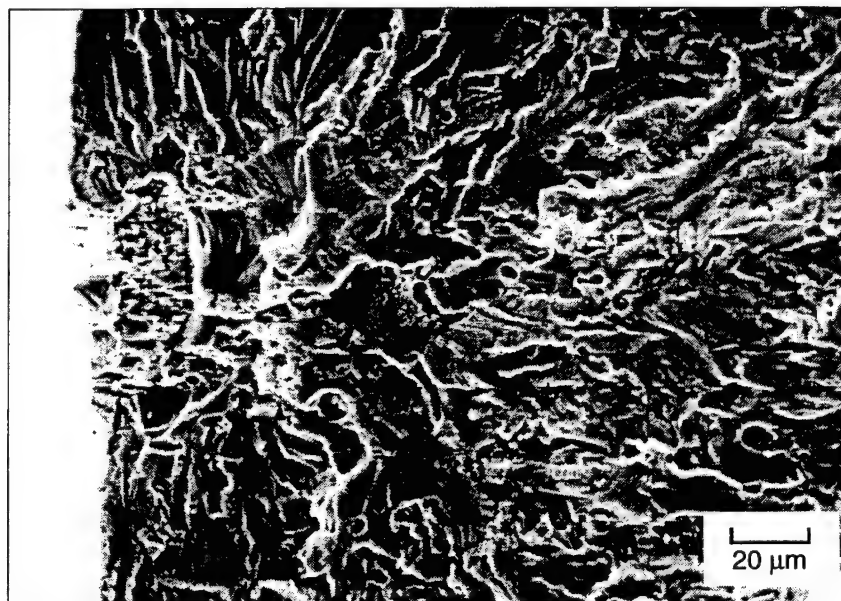
Crack nucleation from crystallographic pits in the clad did not always occur at the largest pit. Figure 35a shows a crack that nucleated next to a colony of crystallographic pits and figure 35b shows several cracks nucleating in different locations within a pit colony. The lack of correlation between crack nucleation sites and geometrical features suggests that the effect of the pitting on crack nucleation in the clad was not to act as a local stress riser, but instead to promote crack nucleation in other ways. Possible reasons for the effect of an aggressive environment on crack nucleation are discussed in the next section.

4.3 HYDROGEN EFFECTS EXPERIMENTS.

In an effort to identify whether hydrogen is essential to the enhancement of the early stages of cracking in Alclad 2024-T3 aluminum, a series of corrosion fatigue experiments was performed



(a) Fracture surface showing corrosion-fatigue crack nucleation at pit

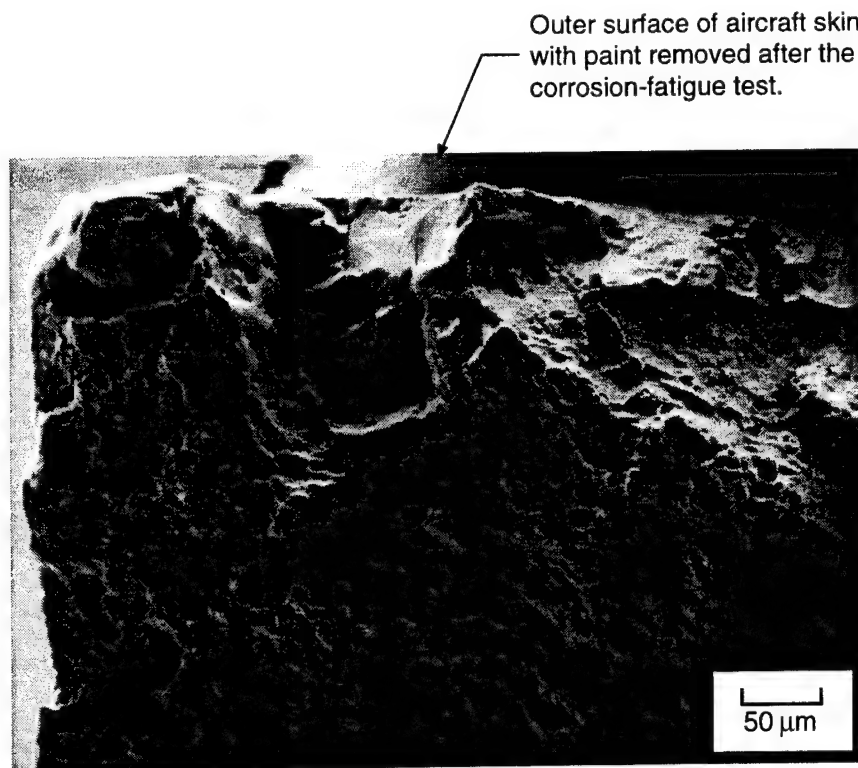


(b) Close-up view of (a)

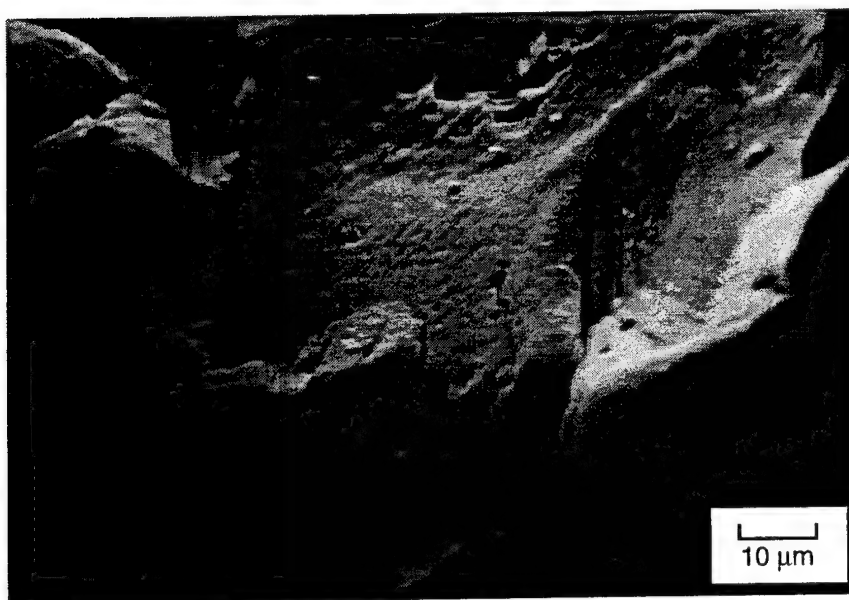
CP-5082-59

Figure 33. Corrosion-fatigue crack nucleation from pit in bare 2024-T3 aluminum.

The fracture surface is from Specimen 3, which was tested in 0.5 M NaCl solution at pH 6. The specimen was in the bare condition and was fatigue loaded with a maximum gross section stress of $0.869 \sigma_y$ for 24,800 cycles.



(a) Fracture surface showing Stage I and Stage II fracture surface around the corrosion-fatigue crack nucleation at the pit

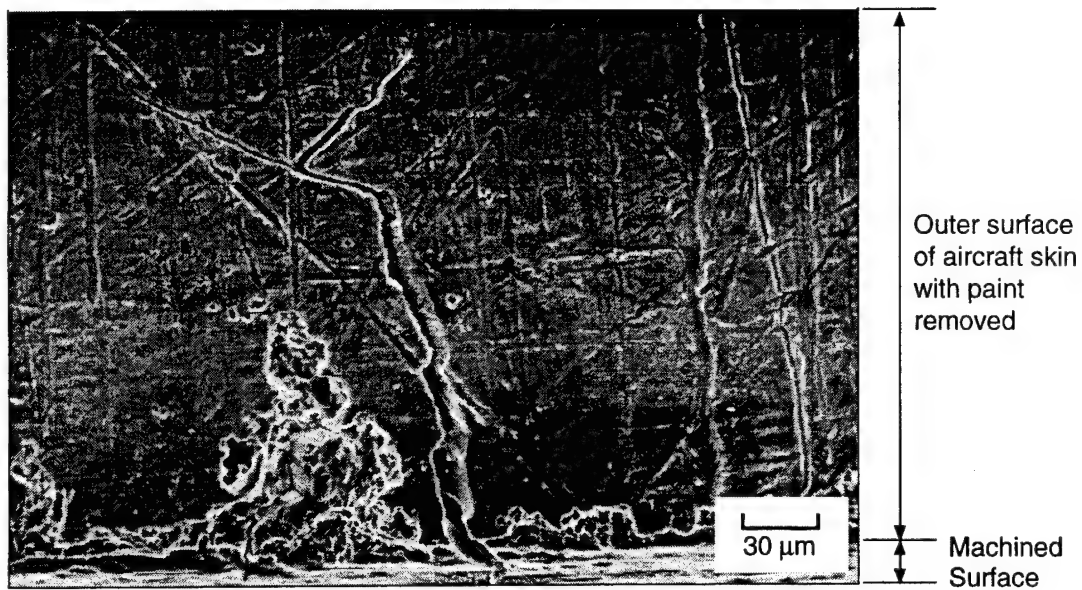


(b) Close-up view of (a) showing pits at the crack initiation site

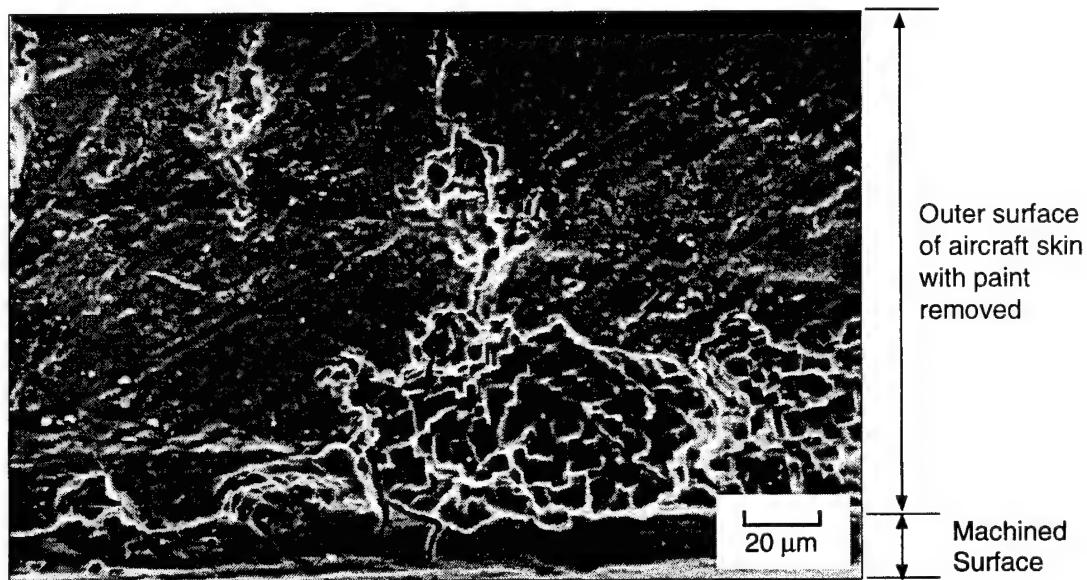
CP-5082-60

Figure 34. Corrosion-fatigue crack nucleation in the cladding of a 2024-T3 aluminum alloy.

The fracture surface is from Specimen 2, which was tested in 0.5 M NaCl solution at pH 6. The specimen was in the as-received condition and was fatigue loaded with a maximum gross section stress of $0.958 \sigma_y$ for 28,600 cycles.



(a) Crack nucleation adjacent to crystallographic pit colony



(b) Multiple cracks nucleating within a crystallographic pit colony

CP-5082-61

Figure 35. Corrosion-fatigue crack nucleation in the clad layer of Alclad 2024-T3 aircraft skin.

Cracks nucleated from the edges of Specimen 2, which was tested in 0.5 M NaCl solution at pH 6. The specimen was in the as-received condition and was fatigue loaded with a maximum gross section stress of $0.958 \sigma_y$ for 28,600 cycles.

under conditions that were expected to introduce hydrogen into, and in some cases remove hydrogen from, Alclad 2024-T3. These tests were run in a similar manner to that described above except for the following:

- Prior to fatigue testing, test specimens were exposed to either 0.5 M NaCl solution for days, 0.5 M NaCl solution for three days followed by storage in vacuum for three days, or long-term storage (many months) in laboratory air. The first environment was to introduce high levels of hydrogen, the second environment was to remove hydrogen, and the third environment was to achieve an intermediate level of hydrogen.
- The tests were conducted in laboratory air and were initiated within 15 minutes of the completion of the pretest environment exposure. The change in hydrogen concentration within the specimens was estimated to be minimal using this test procedure. For example, we estimated, based on the lattice diffusion data of Ishikawa and McLellan,³¹ that the average hydrogen content in the Alclad layer of the specimens exposed to the NaCl solution for three days could have dropped no more than about 15% for the average length of the fatigue tests that were conducted (i.e., about 4.5 hours).
- All tests were fatigued until final fracture so that fracture surfaces could be easily examined. Crack populations along the gage lengths were not measured.

Table 9 lists the test conditions examined in this phase of the investigation. Figure 36 compares the cycles to failure for the three pretest environments examined. On average, specimens that were exposed to the salt water environment had the lowest number of cycles to failure (~38,000 cycles). The average fatigue life increased to about 81,000 cycles when the salt water environment exposure was followed by a vacuum exposure. The highest average number of cycles to failure were produced (~135,000) when the sole pretreatment was a long-term exposure to laboratory air.

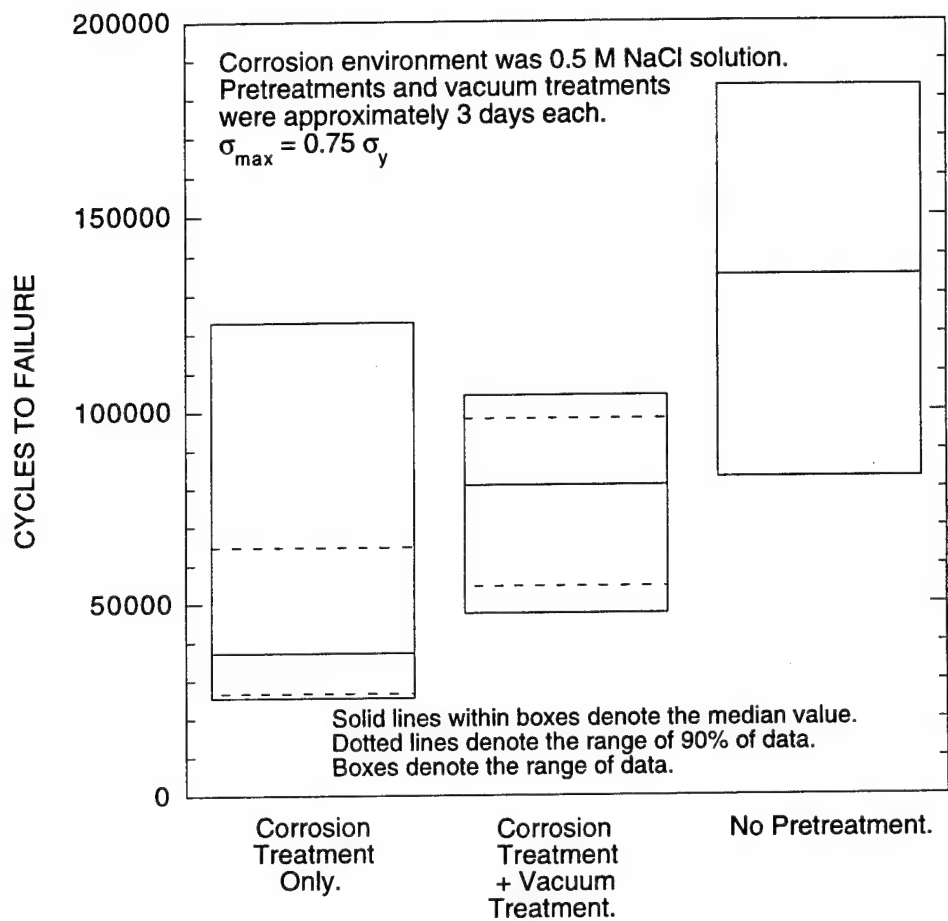
These results indicate that the vacuum treatment produced a partial recovery in the fatigue resistance that was lost as a result of the salt water environment exposure. The amount of recovery is an indication of the extent to which hydrogen appears to have played a role in the nucleation and growth of fatigue cracking. However, the fatigue life of the vacuum-treated specimens was less than the fatigue life of the specimens stored in laboratory air. Based on the kinetics of hydrogen diffusion in aluminum, we expect the specimens stored in laboratory air to have a hydrogen content equal to or greater than that of specimens stored in vacuum. This result suggests that the salt water environment had a detrimental effect on fatigue life, probably as a result of pitting, in addition to the effect of hydrogen. Pitting damage to the clad and the core layers was evident, with an appearance similar to that shown in figures 17, 18, and 19.

Table 9

**CORROSION-FATIGUE TESTS CONDUCTED IN AIR AFTER
VARIOUS PRETREATMENTS^a**

Test Number	Condition of Skin Surface	Surface Condition of Edge of Sheet	Pretest Environment	pH of Pretest Environment	Orientation	Number of Cycles
85	As received	Machined	0.5 M NaCl	6	V	39,600
87	Clad only	Machined	0.5 M NaCl	6	V	75,460
89	Clad only	Machined	0.5 M NaCl	6	V	52,040
91	As received	Machined	0.5 M NaCl	6	V	25,580
92	As received	Machined	0.5 M NaCl + Vacuum	6	V	47,630
93	Clad only	Machined	0.5 M NaCl	6	V	26,800
95	Clad only	Machined	0.5 M NaCl	10	V	122,880
96	Clad only	Machined	0.5 M NaCl + Vacuum	10	V	98,180
97	Clad only	Machined	0.5 M NaCl	10	V	25,960
98	Clad only	Machined	0.5 M NaCl + Vacuum	10	V	104,180
99	Clad only	Machined	0.5 M NaCl	6	V	64,800
100	Clad only	Machined	0.5 M NaCl	6	V	64,040
101	As received	Machined	0.5 M NaCl	6	V	37,300
102	As received	Machined	0.5 M NaCl	6	V	97,390
103	As received	Machined	Air	-	V	169,780
104	Clad only	Machined	0.5 M NaCl	6	H	28,030
105	Clad only	5 μ m polish	0.5 M NaCl	6	H	54,620
106	Clad only	5 μ m polish	Air	-	H	183,150
114	Clad only	Machined	Air	-	V	109,240

^a All tests run at a maximum stress of $0.75 \sigma_y$ in air.



CAM-5082-62

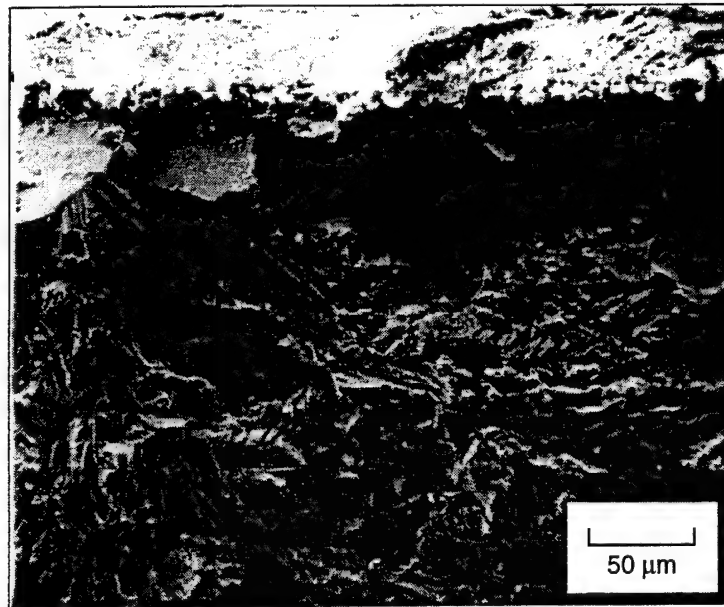
Figure 36. Cycles to failure for tests conducted in air after various pretreatments.

Figure 37 shows SEM micrographs of the fracture surfaces of the clad. Specimens stored in laboratory air prior to fatigue testing exhibited extensive regions of crystallographic cracking along much of the clad (figure 37a). Prefatigue exposures to salt water also produced regions of crystallographic cracking that were frequently most prevalent near crystallographic pit colonies (figure 37b). After the vacuum treatment, crystallographic cracking persisted but appeared to be less widespread (figure 37c). In some cases, crystallographic cracks in the clad did not appear to nucleate the cracks that lead to final fracture. Instead, the cracks leading to final fracture appeared to nucleate from shallow pits in the core material that formed, presumably, at constituent particles.

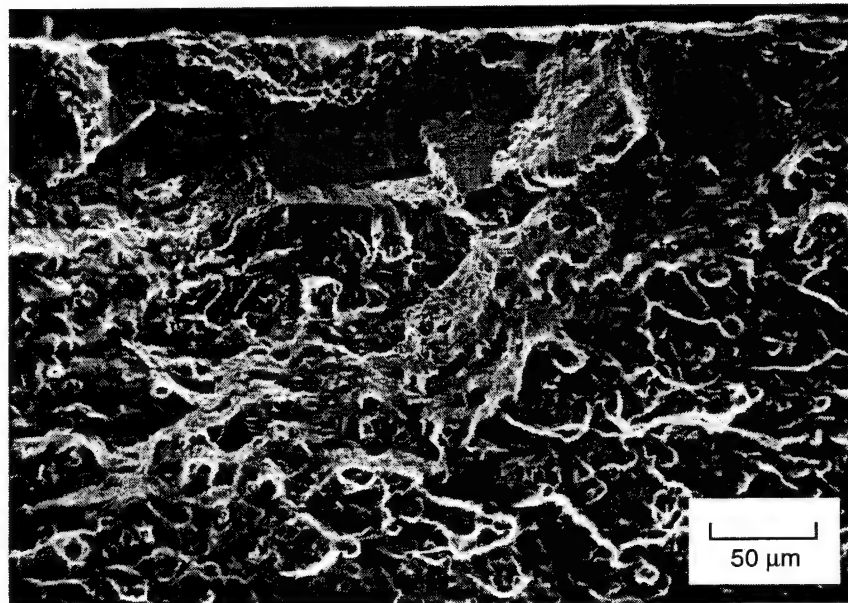
These observations are somewhat ambiguous in that they do not clearly show that crystallographic cracking was promoted by environmental treatments that were designed to vary the hydrogen content of the aluminum. It appears that the test conditions produced a situation where two competing mechanisms for crack nucleation were at work: crack nucleation in the clad due to hydrogen effects and crack nucleation in the core material as a result of pitting at constituent particles. Further experiments are needed to produce conditions that isolate these two mechanisms and determine their sensitivity to the environment, stress, and material condition.

Environmentally assisted cracking of aluminum alloys in salt water environments has often been ascribed to the detrimental effects of hydrogen, especially for high strength alloys of the 7XXX-series. The mechanism for hydrogen embrittlement in such alloys, while still under debate, is often associated with the effects of matrix precipitates through their influence on slip planarity or with grain boundary precipitates through their influence on local hydrogen concentration resulting from trapping.³² Hydrogen effects are enhanced by microstructures that have strengthening precipitates that permit planar slip (e.g., coherent precipitates) so that hydrogen transport from dislocation atmospheres is enhanced. However, it should be noted that hydrogen-induced cracking of 2XXX-series alloys has been rarely observed and requires high levels of dissolved hydrogen to induce an effect.¹⁸

Hydrogen cracking in pure aluminum has been reported in at least two cases. Bond et al.³³ induced cracking in high purity aluminum, transmission electron microscope specimens by injecting small amounts of hydrogen into the microscope. The hydrogen in the microscope column enhanced cracking and dislocation activity, which suggests that embrittlement was actually a result of hydrogen enhanced localized plasticity (known as the HELP mechanism).



(a) No pretreatment; stored in laboratory air (Specimen 103)

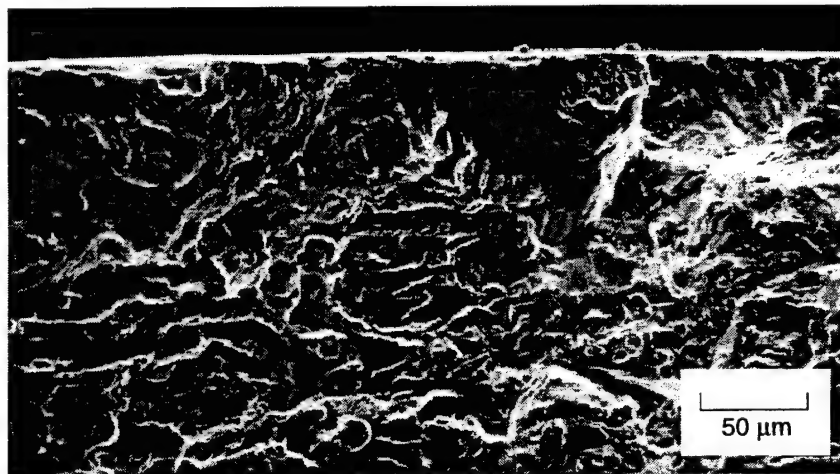


(b) Soaked in 0.5 M NaCl solution for three days (Specimen 89)

CP-5082-63

Figure 37. Fracture surfaces of corrosion-fatigue specimens tested in laboratory air after exposure to various pretest environments.

All fatigue tests were performed at a maximum stress of $0.75 \sigma_y$. Additional details of the test conditions are given in table 9.



(c) Soaked in 0.5 M NaCl solution for three days followed by storage in vacuum for three days (Specimen 100)

CP-5082-64

Figure 37. Fracture surfaces of corrosion-fatigue specimens tested in laboratory air after exposure to various pretest environments (Concluded).

All fatigue tests were performed at a maximum stress of $0.75 \sigma_y$. Additional details of the test conditions are given in table 9.

Tong et al.^{34,35} observed that hydrogen usually increased the rate of corrosion fatigue cracking in pure aluminum single crystals in Mode II and in mixed Mode I/Mode II loading. Sustained cracking was restricted to the close packed crystallographic planes and directions. In most cases, crack growth rates were substantially higher (by as much as a factor of 100) in water-vapor saturated air when compared with the dry air results. Exceptions to this trend were observed in specific situations when the crystallographic orientation was favorable for the aqueous environment to promote secondary microcracks that effectively blunt the primary crack tip.

Using an ion microprobe, Tong et al. determined that local deformation substantially increased the amount of hydrogen in aluminum single crystals immersed in various aqueous environments over that possible by diffusion alone. The high hydrogen contents were found near fatigue fracture surfaces and were attributed to transport enhanced by dislocation sweeping. For example, they found that pure aluminum fracture surfaces fatigued in water-vapor saturated air exhibited a hydrogen content of 6.02 ppm compared with 0.58 ppm for dry air with a relative humidity of less than 20%. Furthermore, they used an ion microprobe to show that hydrogen could promote plastic deformation by reducing the atomic binding energy of aluminum. The magnitude of this reduction was measured to be 11% for an average hydrogen content of 7.5 ppm. The mechanical weakening effect of hydrogen was confirmed through measurements showing that the critical resolved shear stress of aluminum was reduced by hydrogen absorbed from aqueous solutions or moist air when compared with aluminum stored in dry air. For example, the critical resolved shear stress was 1.96 and 1.65 MPa for aluminum with hydrogen levels adjusted to 0.58 and 4.43 ppm, respectively.

The work of Tong et al. and Bond et al. are especially relevant to our study because they identify credible mechanisms involved in the overall process of hydrogen-enhanced nucleation and growth of fatigue cracks in the pure aluminum Alclad layer on 2024-T3 skin exposed to common aqueous environments. Their experiments with pure aluminum show that

- Aqueous environments and moist air can produce high levels of hydrogen in the lattice, especially when effective diffusion rates are enhanced by dislocation sweeping from local deformation
- Once in the lattice, hydrogen significantly reduces the critical resolved shear stress
- The reduction in shear resistance is accompanied by a reduction in the atomic bonding energy in aluminum as a result of dissolved hydrogen
- Hydrogen in aluminum can increase the crack growth rate substantially under static or fatigue loads.

Section 5

SUMMARY AND CONCLUSIONS

5.1 COMPARISON OF CORROSION-FATIGUE DAMAGE PRODUCED IN-SERVICE VERSUS IN THE LABORATORY.

- Much of the corrosion damage we observed on the exterior surface of the fuselage skin of a retired Boeing 737 aircraft consisted of shallow, flat bottomed pits. The size and geometry of these pits indicate that the Alclad layer on the 2024-T3 aluminum skin acted as a sacrificial anode, as intended, and limited the corrosive attack on the underlying skin.
- Much of the corrosion damage for Alclad 2024-T3 aircraft skin samples exposed to NaCl solutions in the laboratory was in the form of crystallographic pit colonies that formed on exposed surfaces of the clad. An acidic environment (pH 2) increased pitting at constituent particles in the core material, in addition to the crystallographic pits in the clad.
- We were unable to compare the characteristics of cracks produced in the laboratory with in-service cracks, because the fuselage panels available to us exhibited no cracks. We will seek to characterize corrosion-fatigue cracks in retired aircraft in the continuation of this program.

5.2 CORROSION-FATIGUE CRACK NUCLEATION.

- More crack nucleation sites were produced in pH 2 and pH 10 solutions of 0.5 M NaCl than in the pH 6 environment. This trend could be a result of the low solubility of corrosion products in pH 6 solutions, which enables an effective protective layer to form that retards the corrosion process.
- Crack nucleation in the Alclad layer was observed to have a weak dependence on material orientation; the horizontal orientation had a lower crack nucleation rate. There were no indications of microstructure directionality, but traces of a rolling pattern on the surface of the sheet were visible. This pattern might be responsible for the orientation dependence.
- Crack nucleation was greater on surfaces of higher roughness. However, no association between specific surface scratches and crack nucleation sites was observed. Possibly, high surface roughness accelerates crack nucleation by promoting hydrogen ingress, which in turn enhances cracking susceptibility.
- Crack nucleation in bare material (i.e., clad and paint removed) was slower than crack nucleation in clad material. The mechanisms of crack nucleation were substantially different in these two cases: in bare material, cracks nucleated at constituent particles, whereas in clad material, cracks usually nucleated at or near

crystallographic pit colonies. Low pH tended to promote crack nucleation at constituent particles in clad material.

- Crack nucleation near crystallographic pits in the clad did not always occur at the largest pit. The lack of correlation between crack nucleation sites and geometrical features suggests that the main effect of the pit is not to act as a local stress riser. Instead, the accelerated corrosion processes associated with a pit may encourage crack nucleation by producing a high, local, hydrogen concentration in the clad on nearby crack-favorable crystallographic planes.

5.3 CORROSION-FATIGUE CRACK PROPAGATION.

- The low pH environment produced a slightly higher crack growth rate than did the pH 6 or pH 10 environments. Similar observations by other investigators indicate enhanced cathodic reactions in acidic solutions as the cause of faster crack growth rate.
- Specimen orientation and surface roughness had no effect on crack propagation rate. This is probably due to the lack of substantial microstructural directionality and the reduced proximity of crack propagation processes to exterior surface features, respectively.
- The crack propagation rate was slightly higher in skin material in the as received condition (i.e., with painted surfaces). This could be due to the tendency of the paint to limit fluid flow from the mouth of a crack and to develop an occluded (i.e., acidic) environment within.

The corrosion-fatigue experiments on Alclad 2024-T3 skin material suggest two competing mechanisms for crack nucleation: crack nucleation in the clad due to hydrogen effects and crack nucleation in the core material as a result of pitting at constituent particles. In the clad material, hydrogen has been shown by several investigators to enhance cracking by enhancing localized plasticity. Pitting at constituent particles is believed to form local stress risers that lead to crack formation. The mechanism that dominates in any given situation depends on environment (e.g., pH), the presence or absence of a clad layer and, perhaps, variables not within the scope of this investigation such as material composition and heat treatment.

Section 6

REFERENCES

1. Y. Kondo, "Prediction of Fatigue Crack Initiation Life Based on Pit Growth," *Corrosion*, **45**(1), 7-11 (1989) .
2. L. Hagn, "Lifetime Prediction of Parts in Corrosion Environments," in *Corrosion in Power Generating Equipment*, Plenum Press (1983).
3. O. Buck and R. Rajan, "Evaluation of a Crack-Tip-Opening Displacement Model Under Stress-Corrosion Conditions," in *Modeling Environmental Effects on Crack Growth Processes*, R. H. Jones and W. W. Gerberich, Eds., The Metallurgical Society, Warrendale, PA (1986), p. 209.
4. M. Müller, "Theoretical Considerations on Corrosion Fatigue Crack Initiation," *Metall. Trans.*, **13A**, 649-655 (April 1982).
5. G. S. Chen, M. Gao, D. G. Harlow, and R. P. Wei, "Corrosion and Corrosion Fatigue on Airframe Aluminum Alloys," *Proceedings of the FAA/NASA International Symposium on Advanced Structural Integrity Methods for Airframe Durability and Damage Tolerance*, C. E. Harris, Ed., Langley Research Center, Hampton, VA, NASA Conf. Publ. 3274 (1994), pp. 157-173.
6. J. C. Newman, Jr. and I. S. Raju, "Stress Intensity Factor Equations for Cracks in Three-Dimensional Finite Bodies," NASA Technical Memorandum 83200 (1981) pp. 1-49, as quoted in *Stress Intensity Factors Handbook*, Vol. 2, Y. Murakami, Ed., Pergamon Press (1990).
7. R. S. Piascik and S. A. Willard, "The Growth of Small Corrosion Fatigue Cracks in Alloy 2024," NASA Technical Memorandum 107755, NASA Langley Research Center, Hampton, VA (April 1993).
8. Kaleidagraph™ Reference Guide, 3rd Edition, Synergy Software, Reading, PA.
9. R. H. Brown, "Aluminum Alloy Laminates: Alclad and Clad Aluminum Alloy Products," in *Composite Engineering Laminates*, A. G. H. Dietz, Ed., MIT Press, Cambridge, MA (1969), pp. 227-239.
10. E. H. Hollingsworth and H. Y. Hunsicker, "Corrosion of Aluminum and Aluminum Alloys," in *Metals Handbook, Volume 13, Corrosion*, ASM International, Metals Park, OH (1987), pp. 583-608.
11. P. Gimenez, J. J. Rameau, and M. C. Reboul, "Experimental pH Potential Diagram of Aluminum for Sea Water," *Corrosion*, **37**(12), 673-682 (1981).
12. R. C. Newman, "Local Chemistry Considerations in the Tunneling Corrosion of Aluminum," *Corrosion Science*, **37**(3), 527-533 (1995).

13. L. L. Shreir, Ed., *Corrosion, Volume 1, Metal/Environment Reactions*, Second Edition, Newnes-Butterworths, London (1976), pp. 1-206.
14. M. R. Bothwell, "Galvanic Relationships between Aluminum Alloys and Magnesium Alloys, I. Galvanic Couples," *J. Electro. Soc.*, **106**(12), 1014-1018 (1959).
15. M. R. Bothwell, "Galvanic Relationships between Aluminum Alloys and Magnesium Alloys, II. Aluminum Claddings on Magnesium," *J. Electro. Soc.*, **106**(12), 1019-1021 (1959).
16. R. Ambat and E. S. Dwarakadasa, "The Influence of pH on the Corrosion of Medium Strength Aerospace Alloys 8090, 2091, and 2014," *Corrosion Science*, **33**(5), 681-690 (1992).
17. *Microsoft® Excel Function Reference*, Version 3.0, Microsoft Corp., Redmond, WA (1991) pp. 138-141.
18. F. A. McClintock and A. L. Argon, *Mechanical Behavior of Materials*, Addison-Wesley, Reading, MA, (1966) p. 589.
19. E. Deltombe, C. Vanleugenhaghe, and M. Pourbaix, "Aluminium - Section 5.2" in *Atlas of Electrochemical Equilibria in Aqueous Solutions*, M. Pourbaix, Ed., NACE, Houston, TX (1974).
20. D. A. Hardwick, M. Taheri, A. W. Thompson, and I. M. Bernstein, "Hydrogen Embrittlement in a 2000-Series Aluminum Alloy," *Metall. Trans.*, **13A**, 235-239 (1982).
21. S. W. Ciaraldi, Ph.D. Thesis, University of Illinois at Urbana-Champaign (1980) as cited in Reference 17.
22. J. Chaudhuri, Y. M. Tan, V. Gondhalekar, and K. M. Patni, "Comparison of Corrosion Fatigue Properties of Pre-corroded 6013 Bare and 2024 Bare Aluminum Alloy Sheet Materials," *J. Mater. Engr. Perform.*, **3**, 371-377 (1994).
23. J. Chaudhuri, Y. M. Tan, K. M. Patni, and A. Eftekhari, "Comparison of Corrosion Fatigue Properties of 6013 Bare, Alclad 2024, and 2024 Bare Aluminum Alloy Sheet Materials," *J. Mater. Engr. Perform.*, **1**, 91-96 (1992).
24. P. J. E. Forsyth, "Fatigue Damage and Crack Growth in Aluminium Alloys," *Acta Metall.*, **11**, 703-715 (1963).
25. A. J. Sedricks, J. A. S. Green, and D. L. Novak, "Comparison of the Corrosion and Stress-Corrosion Behavior of a Ternary Al-Zn-Mg Alloy," *Metall. Trans.*, **1**, 1815-1819 (1970).
26. J. McHardy and E. H. Hollingsworth, U. S. Navy Contract Report NOW 65-0327f (1966), as cited in Reference 28.
27. H. F. de Jong, "Influence of Loading Direction and Environment on the SCC Susceptibility of Aluminium 7075-T651," *Brit. Corros. J.*, **15**, 118-122 (1980).
28. N. J. H. Holroyd, "Environment-Induced Cracking of High-Strength Aluminum Alloys," in *Environmentally Induced Cracking of Metals*, R. P. Gangloff and M. B. Ives, Eds., NACE-10, National Association of Corrosion Engineers, Houston, TX (1990), pp. 311-345.

29. Metals Handbook, *Fractography and Atlas of Fractographs*, Vol. 9, Eighth Edition, American Society for Metals, Metals Park, OH (1974), pp. 68-70.
30. R. P. Gangloff, "Corrosion Fatigue Crack Propagation in Metals," in *Environmentally Induced Cracking of Metals*, R. P. Gangloff and M. B. Ives, Eds., NACE-10, National Association of Corrosion Engineers, Houston, TX (1990) pp. 55-109 cited the following: A. Niegel, H.-J. Gudladt, V. Gerold, J. de Physique, Colloque C5 49 (1988) pp. 659-663; H. -J. Gudladt, A. Niegel, P. Liang, Proc. Mater. Res. Soc. 122 (Boston, MA:MRS, 1988) pp. 405-409; and P. Liang, H. -J. Gudladt, V. Gerold, Low Cycle Fatigue and Elastic Plastic Behavior of Materials, K. -T. Rie, Ed. (London, United Kingdom, Elsevier Applied Science, 1987), pp. 687-692.
31. T. Ishikawa and R. B. McLellan, "The Diffusivity of Hydrogen in Aluminum," *Acta Metall.*, **34**(6), 1091-1095 (1986).
32. T. D. Burleigh, "The Postulated Mechanisms for Stress Corrosion Cracking of Aluminum Alloys," *Corrosion*, **47**(2), 89-98 (1991).
33. G. M. Bond, I. M. Robertson, and H. K. Birnbaum, "Effects of Hydrogen on Deformation and Fracture Processes in High-Purity Aluminum," *Acta Metall.*, **36**(8), 2193-2197 (1988).
34. Z-X Tong, S. Lin, and C-M Hsiao, "The Influence of Hydrogen on Atomic Binding Energy, Critical Slip Shear Stress, and Fatigue Crack Propagation Rate of Aluminum Single Crystals," *Metall. Trans.*, **20A**, 921-924 (1989).
35. Z-X Tong, S. Lin, and C-M Hsiao, "The Influence of Water Vapor on the Fatigue Crack Propagation Kinetics in Pure Aluminum Single Crystals," *Metall. Trans.*, **20A**, 925-933 (1989).

Appendix
CRACK SIZE DISTRIBUTIONS

The distributions of crack sizes for the tests used in the analysis of crack growth rate are compiled in this appendix. The data are shown with the least squares fit of equation 7. A detailed description of the analysis procedure is given in sections 3.3 and 3.4.

$y = m1 \cdot \exp(28600 \cdot m0^2 \cdot 22177 \dots)$		
	Value	Error
m1	1.3968e-07	1.5765e-07
m2	1.3992e-09	2.0498e-10
Chisq	6.0547e-08	NA
R	0.90414	NA

The solid line is a least squares fit of the integrated form of the Paris Law to the data.

$m1 = a_{\text{initial}}$

$m2 = C$

where $da/dN = C (\Delta K)^2$.

a is in meters and ΔK is in $\text{MPa}\sqrt{\text{m}}$.

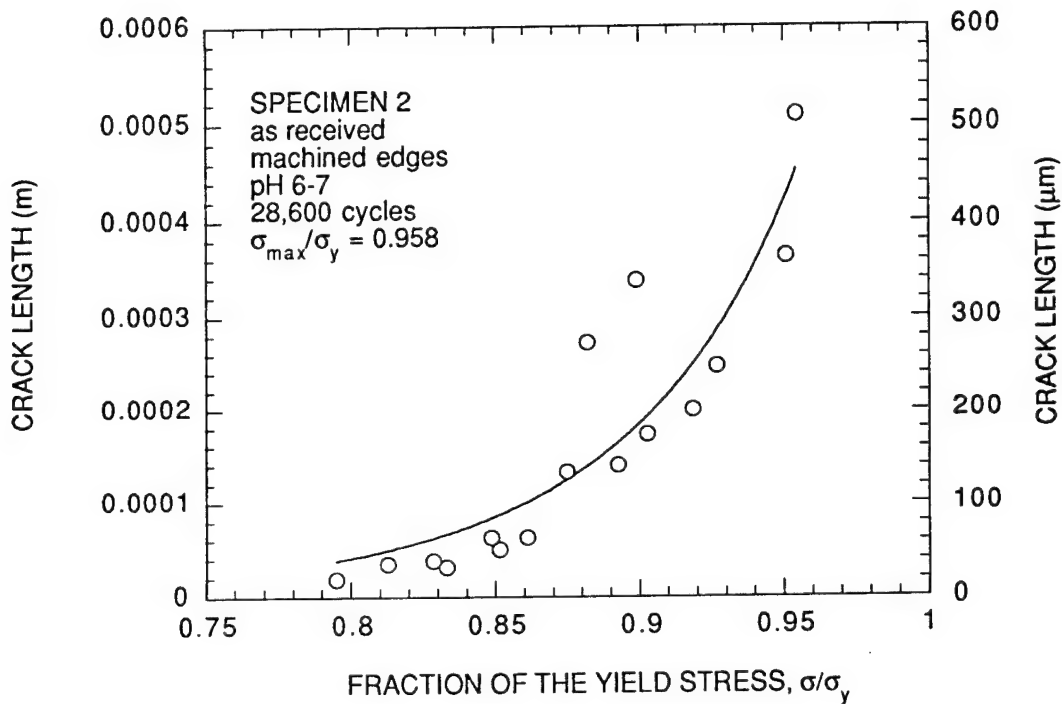


Figure A-1. Crack length data measurements and the least squares fit for Test 2.

$y = m1 \cdot \exp(19650 \cdot m0^2 \cdot 22177 \dots)$		
	Value	Error
m1	1.6813e-07	1.0346e-07
m2	1.6608e-09	1.6648e-10
Chisq	2.8448e-09	NA
R	0.9359	NA

The solid line is a least squares fit of the integrated form of the Paris Law to the data.

$m1 = a_{\text{initial}}$

$m2 = C$

where $da/dN = C (\Delta K)^2$.

a is in meters and ΔK is in $\text{MPa}\sqrt{\text{m}}$.

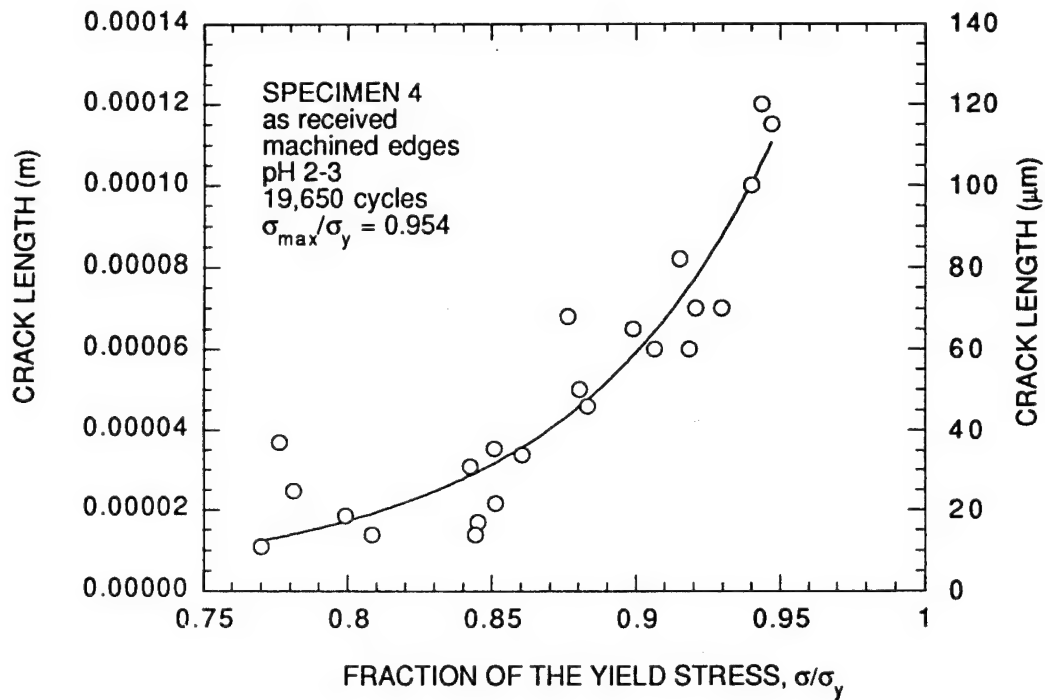


Figure A-2. Crack length data measurements and the least squares fit for Test 4.

y = m1*exp(160810*m0^ 2*2217...		
	Value	Error
m1	4.879e-07	4.7509e-07
m2	7.2705e-10	1.512e-10
Chisq	4.9877e-10	NA
R	0.89845	NA

The solid line is a least squares fit of the integrated form of the Paris Law to the data.

m1 = a_{initial}

m2 = C

where $da/dN = C (\Delta K)^2$.

a is in meters and ΔK is in $\text{MPa}\sqrt{\text{m}}$.

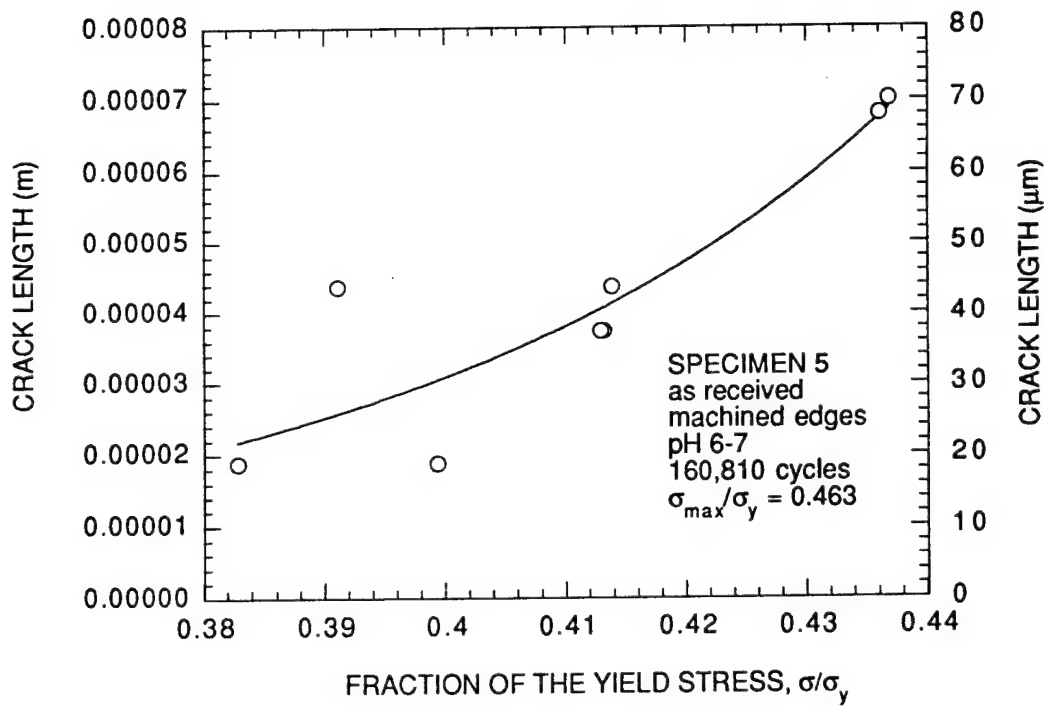


Figure A-3. Crack length data measurements and the least squares fit for Test 5.

y = m1*exp(24660*m0^ 2*22177...		
	Value	Error
m1	6.4825e-19	2.1444e-18
m2	6.9607e-09	6.6659e-10
Chisq	1.7091e-09	NA
R	0.99555	NA

The solid line is a least squares fit of the integrated form of the Paris Law to the data.

$m1 = a_{\text{initial}}$

$m2 = C$

where $da/dN = C (\Delta K)^2$.

a is in meters and ΔK is in MPa $\sqrt{\text{m}}$.

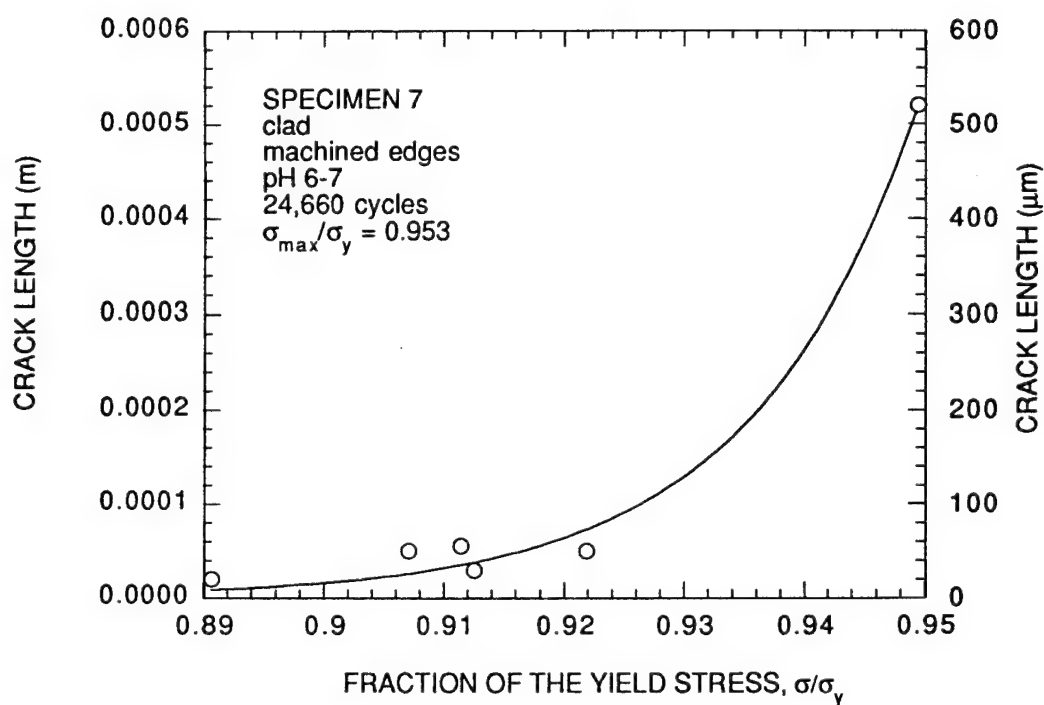


Figure A-4. Crack length data measurements and the least squares fit for Test 7.

y = m1*exp(26330*m0^ 2*22177...		
	Value	Error
m1	1.27e-08	2.2281e-08
m2	1.7317e-09	3.6034e-10
Chisq	4.9515e-10	NA
R	0.91363	NA

The solid line is a least squares fit of the integrated form of the Paris Law to the data.

$m1 = a_{\text{initial}}$

$m2 = C$

where $da/dN = C (\Delta K)^2$.

a is in meters and ΔK is in $\text{MPa}\sqrt{\text{m}}$.

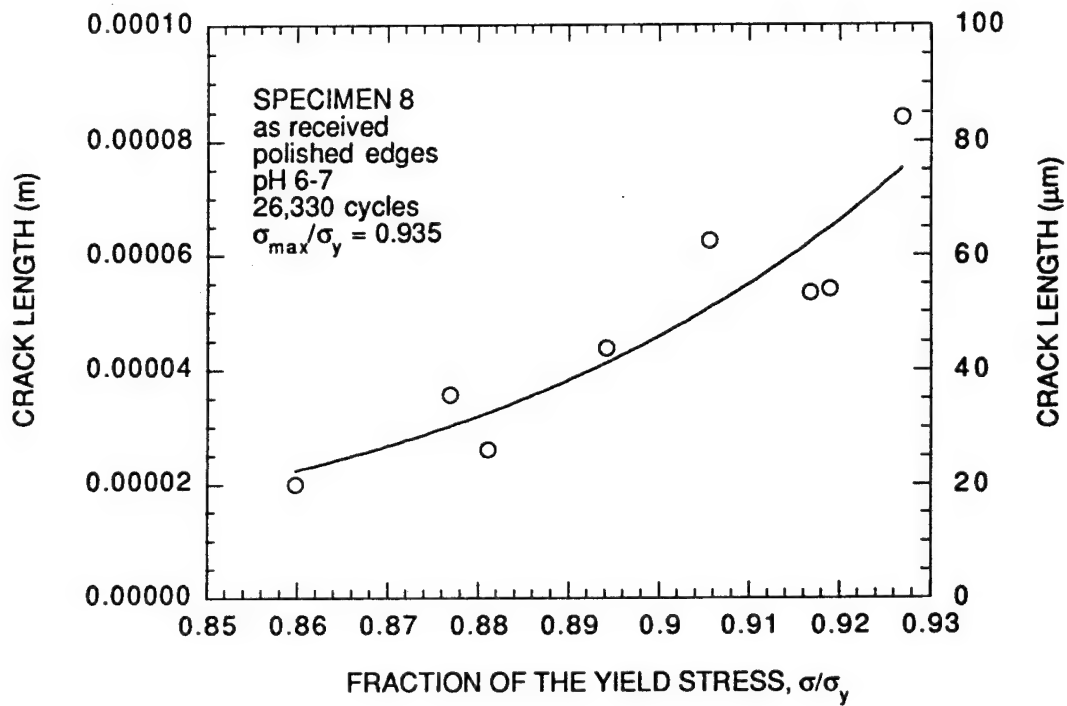


Figure A-5. Crack length data measurements and the least squares fit for Test 8.

$y = m1 \cdot \exp(20000 \cdot m0^2 \cdot 22177 \dots)$		
	Value	Error
m1	5.1258e-08	1.815e-07
m2	2.0586e-09	1.0189e-09
Chisq	2.3211e-09	NA
R	0.79694	NA

The solid line is a least squares fit of the integrated form of the Paris Law to the data.

$m1 = a_{\text{initial}}$

$m2 = C$

where $da/dN = C (\Delta K)^2$.

a is in meters and ΔK is in $\text{MPa}\sqrt{\text{m}}$.

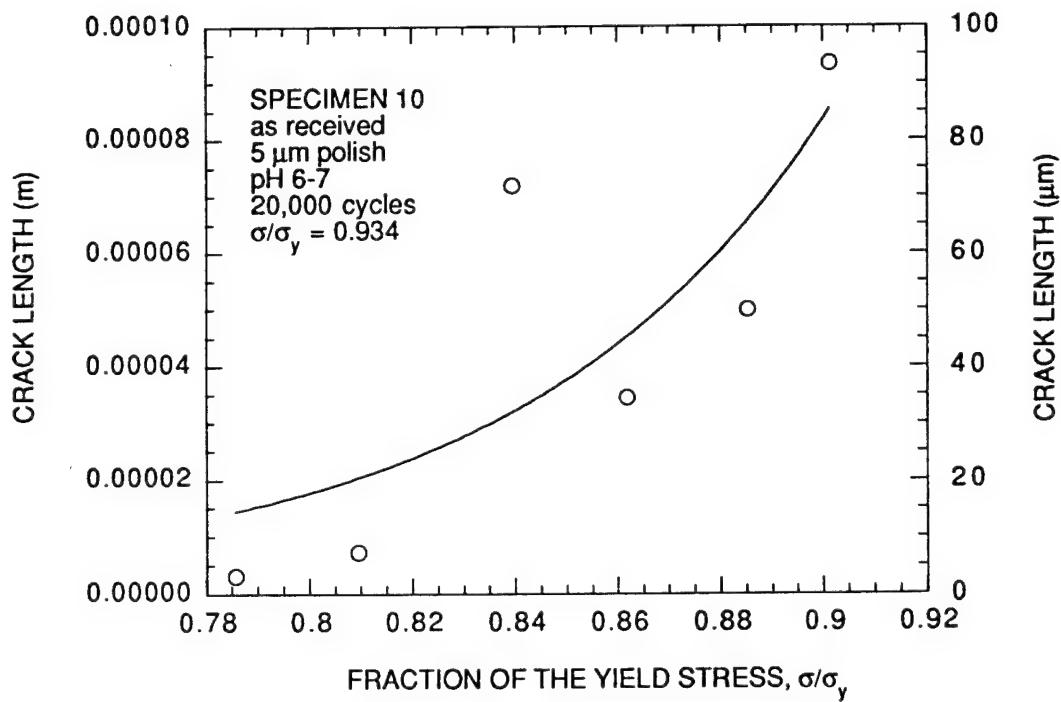


Figure A-6. Crack length data measurements and the least squares fit for Test 10.

$y = m1 \cdot \exp(9570 \cdot m0^2 \cdot 221779 \dots)$		
	Value	Error
m1	1.0624e-06	1.6994e-06
m2	2.6902e-09	9.3075e-10
Chisq	6.1084e-09	NA
R	0.80787	NA

The solid line is a least squares fit of the integrated form of the Paris Law to the data.

$m1 = a_{\text{initial}}$

$m2 = C$

where $da/dN = C (\Delta K)^2$.

a is in meters and ΔK is in $\text{MPa}\sqrt{\text{m}}$.

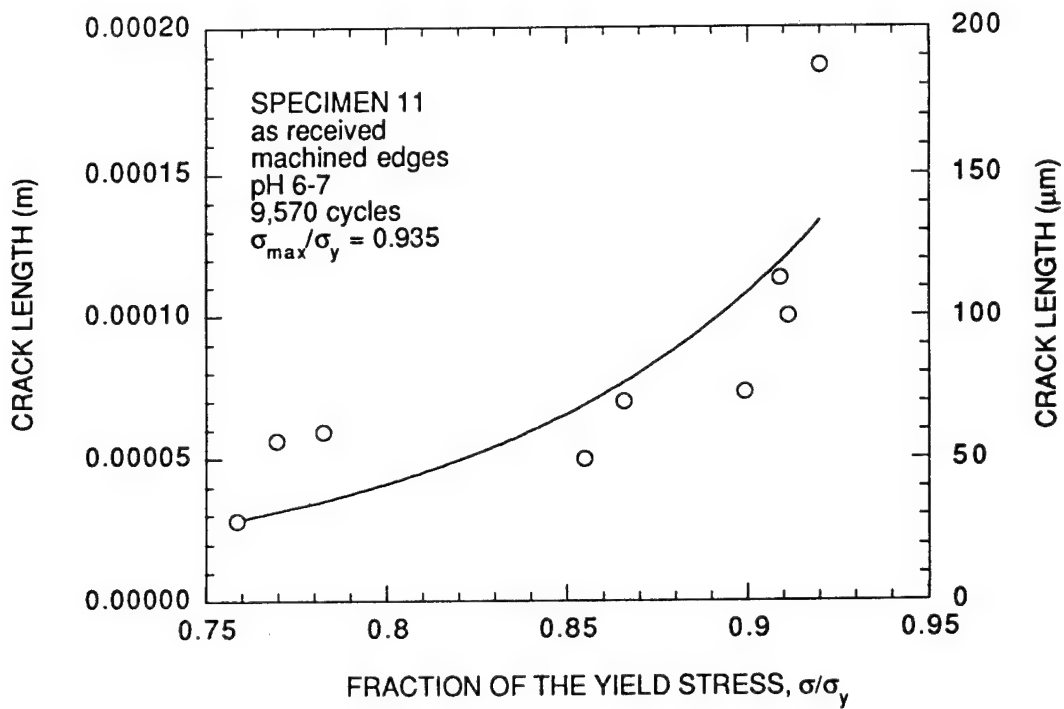


Figure A-7. Crack length data measurements and the least squares fit for Test 11.

y = m1*exp(20000*m0^ 2*22177...		
	Value	Error
m1	4.8716e-07	6.7344e-07
m2	1.078e-09	3.8323e-10
Chisq	1.3504e-10	NA
R	0.80329	NA

The solid line is a least squares fit of the integrated form of the Paris Law to the data.

$m1 = a_{\text{initial}}$

$m2 = C$

where $da/dN = C (\Delta K)^2$.

a is in meters and ΔK is in $\text{MPa}\sqrt{\text{m}}$.

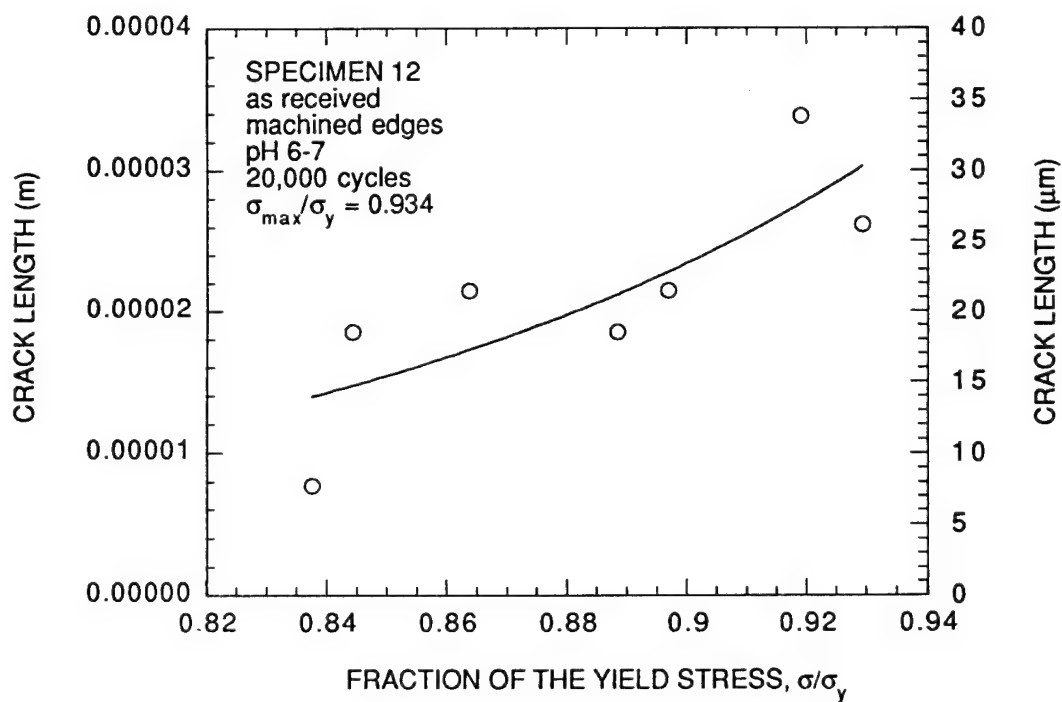


Figure A-8. Crack length data measurements and the least squares fit for Test 12.

$y = m1 \cdot \exp(16580 \cdot m0^2 \cdot 22177 \dots)$		
	Value	Error
m1	9.0341e-07	5.9993e-07
m2	1.4999e-09	2.1112e-10
Chisq	1.0889e-08	NA
R	0.84855	NA

The solid line is a least squares fit of the integrated form of the Paris Law to the data.

$m1 = a_{\text{initial}}$

$m2 = C$

where $da/dN = C (\Delta K)^2$.

a is in meters and ΔK is in $\text{MPa}\sqrt{\text{m}}$.

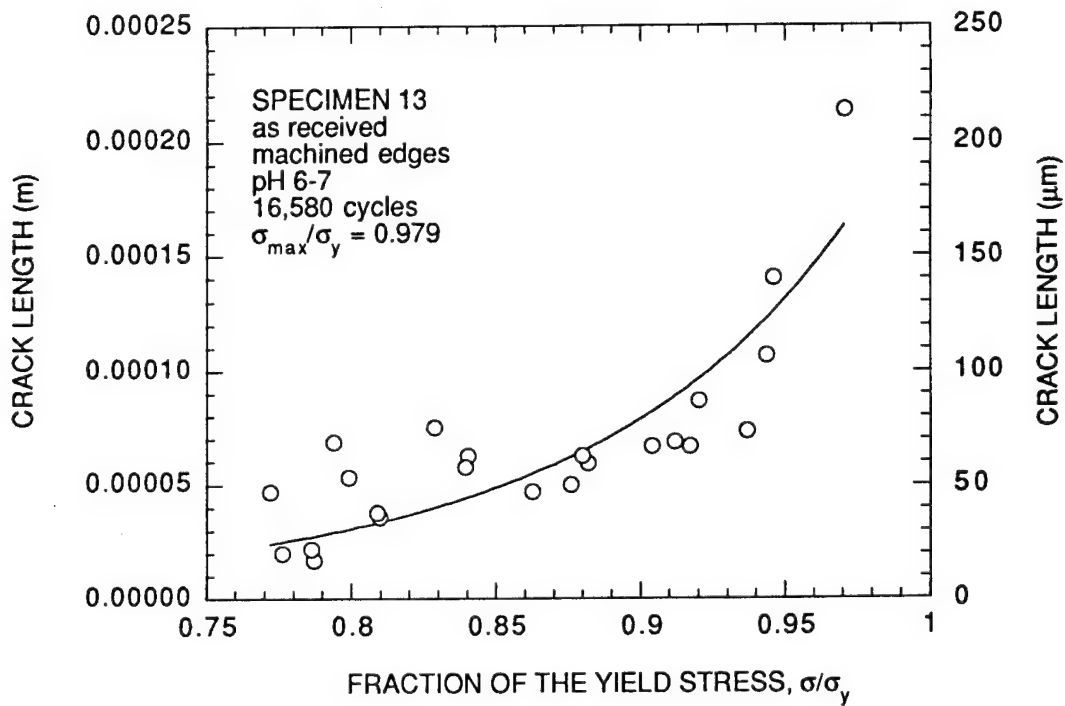


Figure A-9. Crack length data measurements and the least squares fit for Test 13.

$y = m1 \cdot \exp(264380 \cdot m0^{\wedge} 2 \cdot 2217 \dots)$		
	Value	Error
m1	6.9549e-07	9.9547e-07
m2	3.6726e-10	1.0443e-10
Chisq	9.9005e-09	NA
R	0.82114	NA

The solid line is a least squares fit of the integrated form of the Paris Law to the data.

$m1 = a_{\text{initial}}$

$m2 = C$

where $da/dN = C (\Delta K)^2$.

a is in meters and ΔK is in $\text{MPa}\sqrt{\text{m}}$.

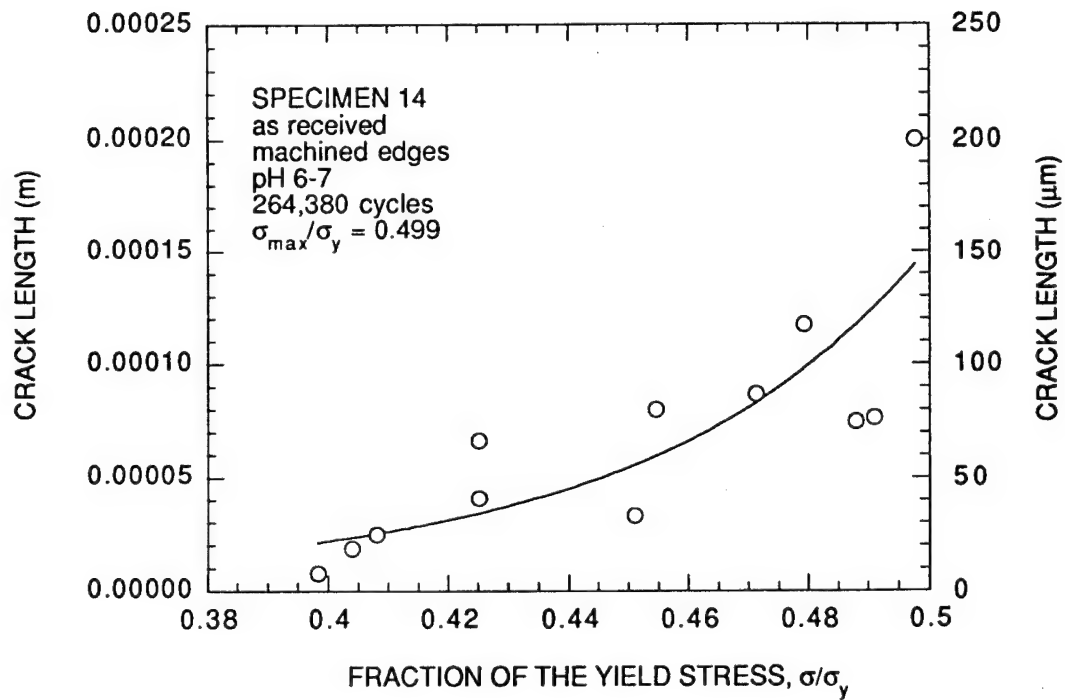


Figure A-10. Crack length data measurements and the least squares fit for Test 14.

y = m1*exp(150000*m0^ 2*2217...		
	Value	Error
m1	3.3474e-09	7.534e-09
m2	1.5924e-09	3.0399e-10
Chisq	4.2235e-08	NA
R	0.93694	NA

The solid line is a least squares fit of the integrated form of the Paris Law to the data.

m1 = a_{initial}

m2 = C

where $da/dN = C (\Delta K)^2$.

a is in meters and ΔK is in MPa $\sqrt{\text{m}}$.

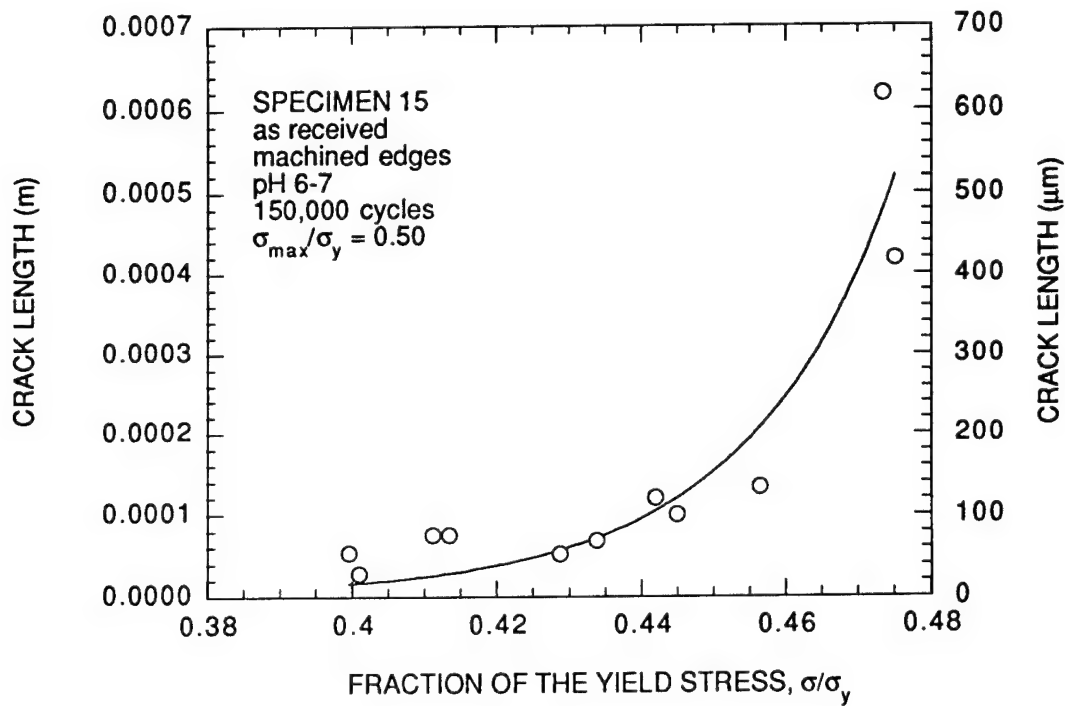


Figure A-11. Crack length data measurements and the least squares fit for Test 15.

y = m1*exp(30000*m0^ 2*22177...		
	Value	Error
m1	4.2223e-05	2.0523e-05
m2	4.308e-10	1.5799e-10
Chisq	2.9526e-09	NA
R	0.82581	NA

The solid line is a least squares fit of the integrated form of the Paris Law to the data.

m1 = a_{initial}

m2 = C

where $da/dN = C (\Delta K)^2$.

a is in meters and ΔK is in MPa $\sqrt{\text{m}}$.

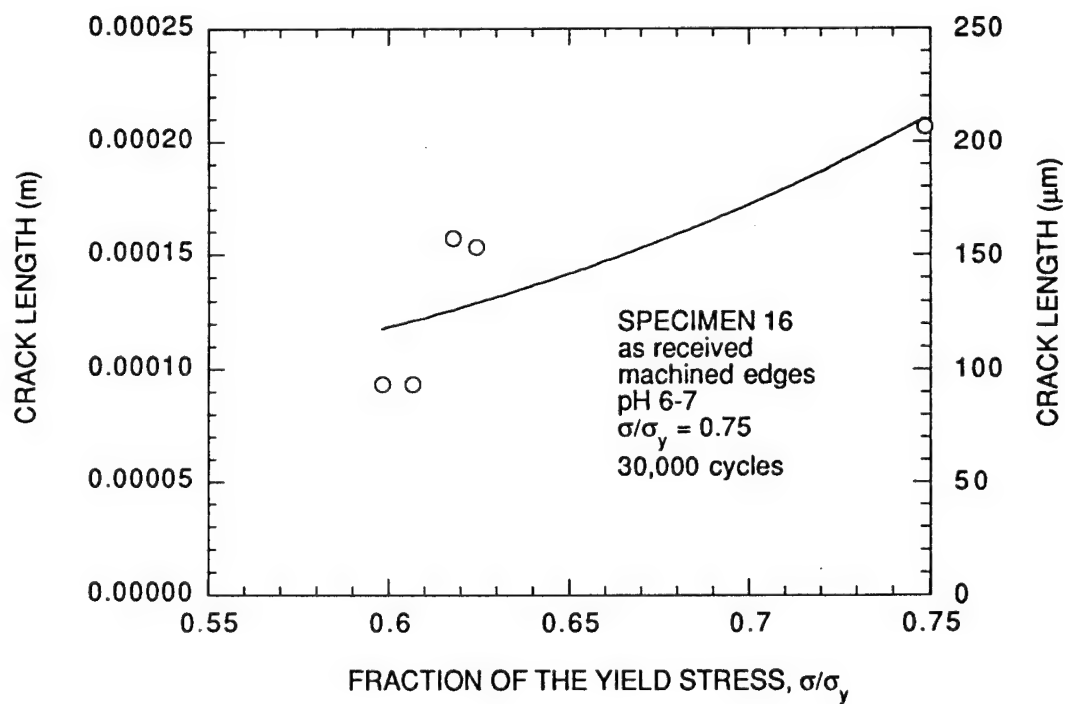


Figure A-12. Crack length data measurements and the least squares fit for Test 16.

y = m1*exp(150000*m0^ 2*2217...		
	Value	Error
m1	7.0292e-06	6.1453e-06
m2	1.4138e-10	1.2432e-10
Chisq	1.5458e-10	NA
R	0.4165	NA

The solid line is a least squares fit of the integrated form of the Paris Law to the data.

$m1 = a_{\text{initial}}$

$m2 = C$

where $da/dN = C (\Delta K)^2$.

a is in meters and ΔK is in $\text{MPa}\sqrt{\text{m}}$.

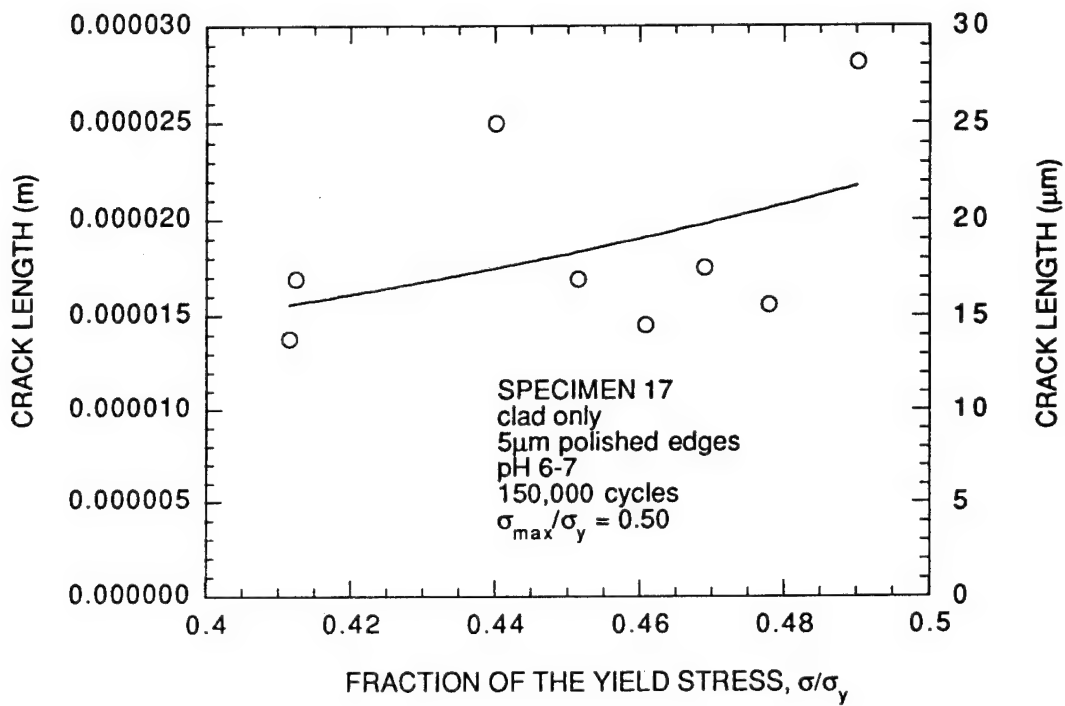


Figure A-13. Crack length data measurements and the least squares fit for Test 17.

$y = m1 \cdot \exp(30000 \cdot m0^2 \cdot 22177 \dots)$		
	Value	Error
m1	1.2848e-05	7.8078e-06
m2	3.4077e-10	1.858e-10
Chisq	1.3062e-09	NA
R	0.44823	NA

The solid line is a least squares fit of the integrated form of the Paris Law to the data.

$m1 = a_{\text{initial}}$

$m2 = C$

where $da/dN = C (\Delta K)^2$.

a is in meters and ΔK is in MPa $\sqrt{\text{m}}$.

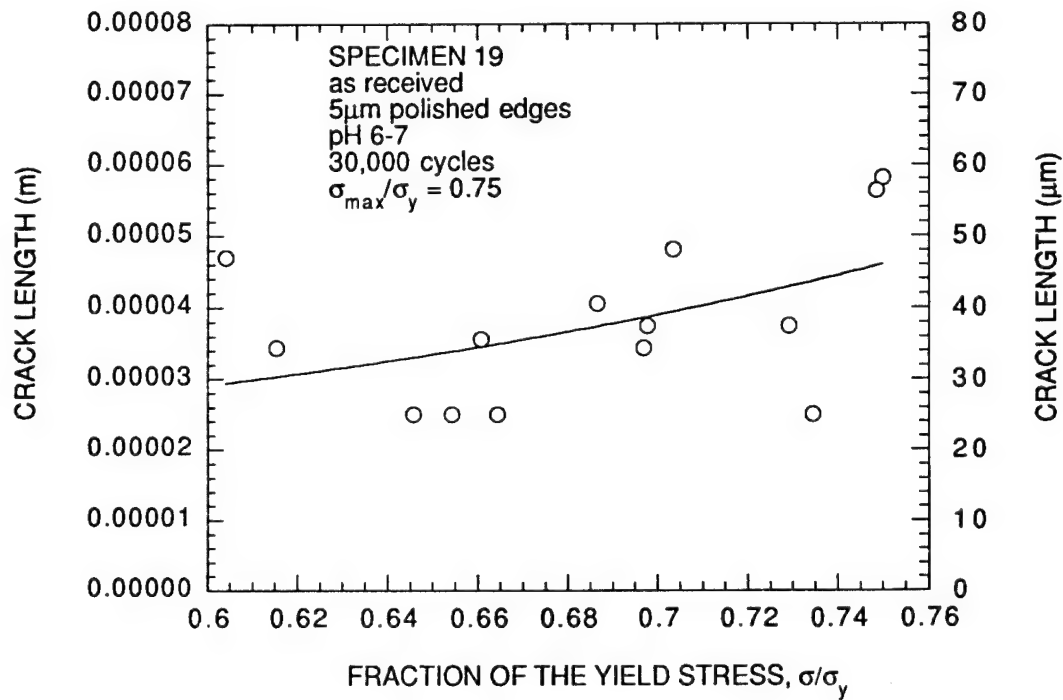


Figure A-14. Crack length data measurements and the least squares fit for Test 19.

$y = m1 \cdot \exp(20000 \cdot m0 \cdot x^{2.22177...})$		
	Value	Error
m1	1.7409e-06	7.6909e-07
m2	7.7316e-10	1.1184e-10
Chisq	1.0502e-09	NA
R	0.86866	NA

The solid line is a least squares fit of the integrated form of the Paris Law to the data.

$m1 = a_{\text{initial}}$

$m2 = C$

where $da/dN = C (\Delta K)^2$.

a is in meters and ΔK is in $\text{MPa}\sqrt{\text{m}}$.

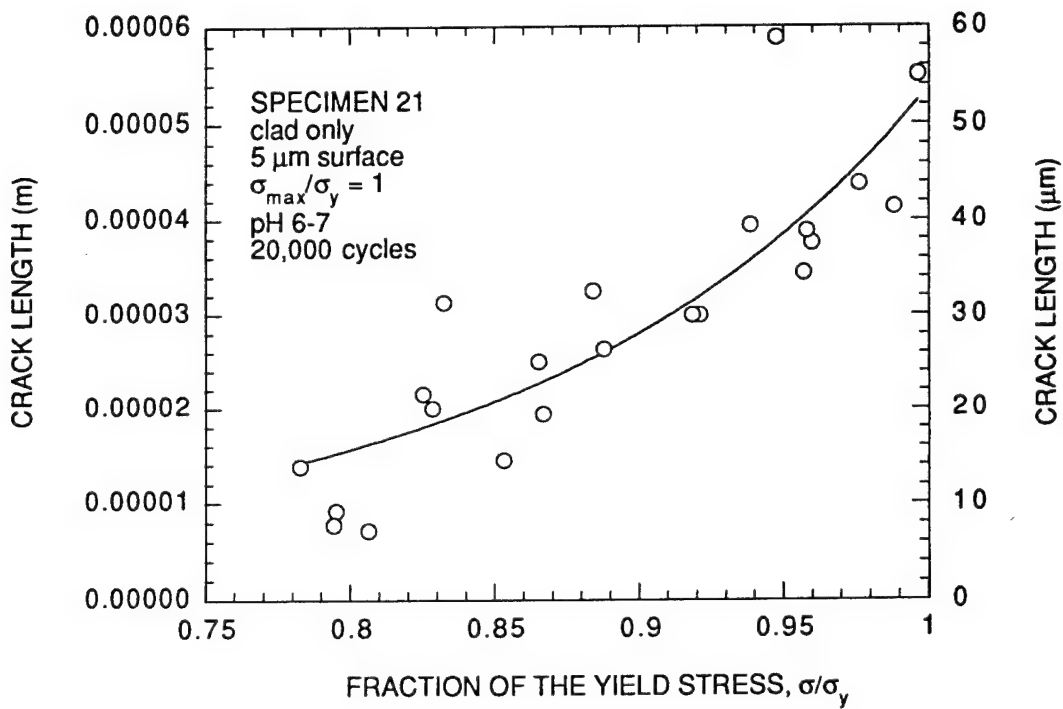


Figure A-15. Crack length data measurements and the least squares fit for Test 21.

$y = m1 \cdot \exp(10440 \cdot m0^2 \cdot 22177 \dots)$		
	Value	Error
m1	3.0838e-06	4.7525e-06
m2	3.466e-09	2.9676e-09
Chisq	7.466e-10	NA
R	0.29388	NA

The solid line is a least squares fit of the integrated form of the Paris Law to the data.

$m1 = a_{\text{initial}}$

$m2 = C$

where $da/dN = C (\Delta K)^2$.

a is in meters and ΔK is in $\text{MPa}\sqrt{\text{m}}$.

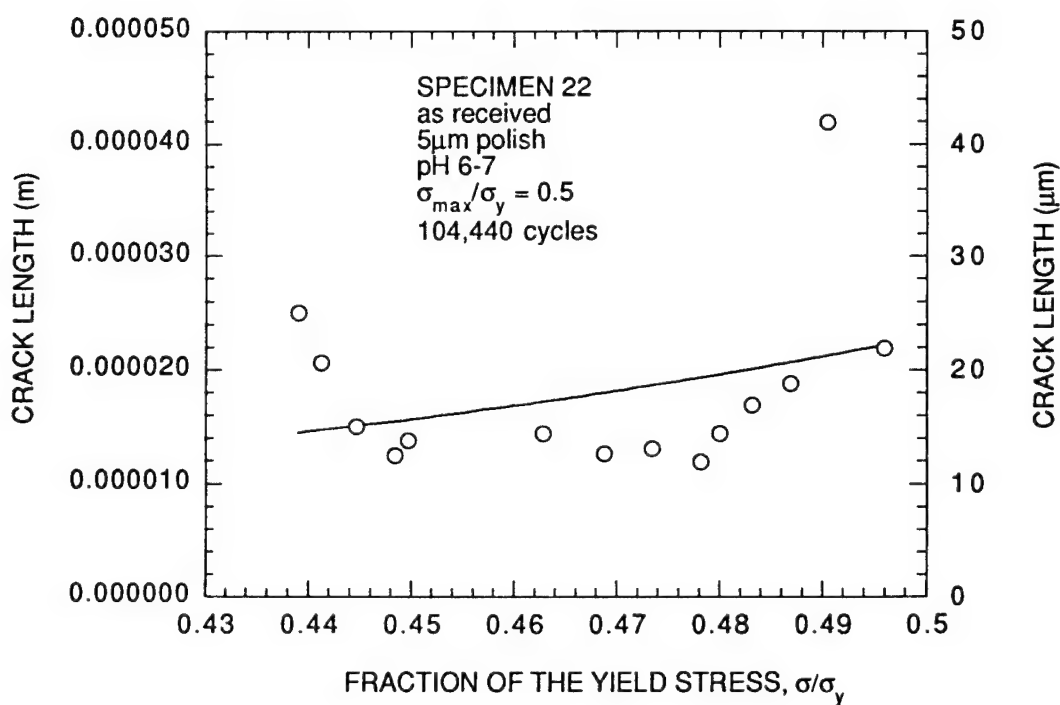


Figure A-16. Crack length data measurements and the least squares fit for Test 22.

$y = m1 \cdot \exp(150000 \cdot m0^2 \cdot 2217 \dots)$		
	Value	Error
m1	6.8963e-06	2.8143e-06
m2	2.1091e-10	5.6453e-11
Chisq	2.0424e-10	NA
R	0.77561	NA

The solid line is a least squares fit of the integrated form of the Paris Law to the data.

$m1 = a_{\text{initial}}$

$m2 = C$

where $da/dN = C (\Delta K)^2$.

a is in meters and ΔK is in $\text{MPa}\sqrt{\text{m}}$.

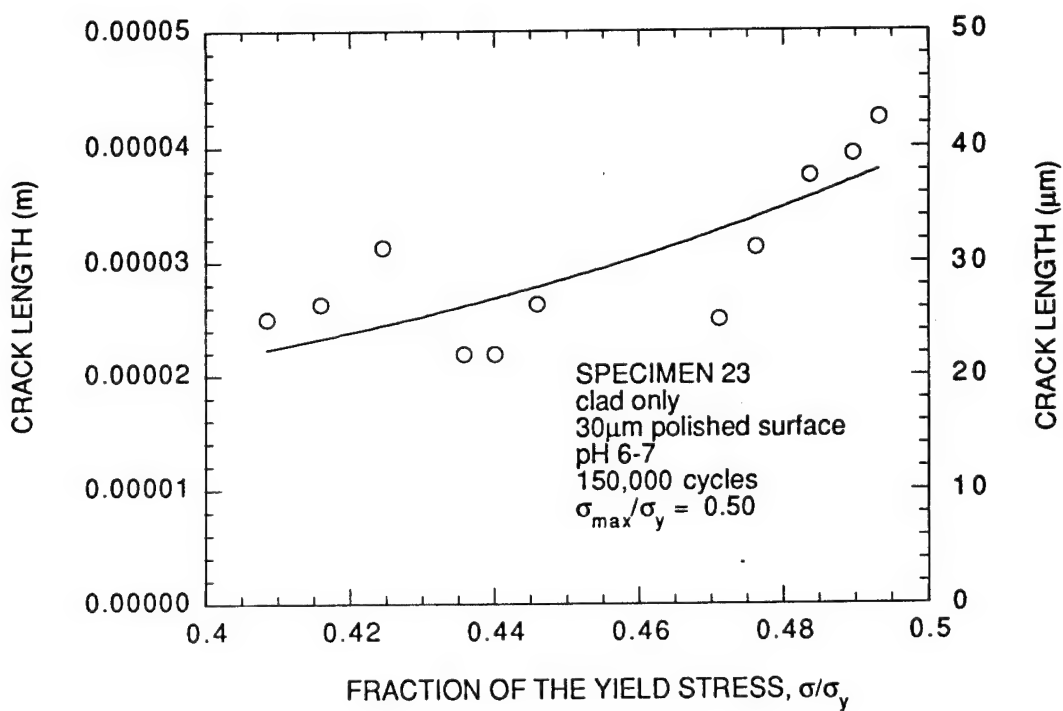


Figure A-17. Crack length data measurements and the least squares fit for Test 23.

$y = m1 \cdot \exp(150000 \cdot m0^2 \cdot 2217 \dots)$		
	Value	Error
m1	1.8952e-06	9.1039e-07
m2	3.0634e-10	6.6396e-11
Chisq	2.6441e-10	NA
R	0.77657	NA

The solid line is a least squares fit of the integrated form of the Paris Law to the data.

$m1 = a_{\text{initial}}$

$m2 = C$

where $da/dN = C (\Delta K)^2$.

a is in meters and ΔK is in $\text{MPa}\sqrt{\text{m}}$.

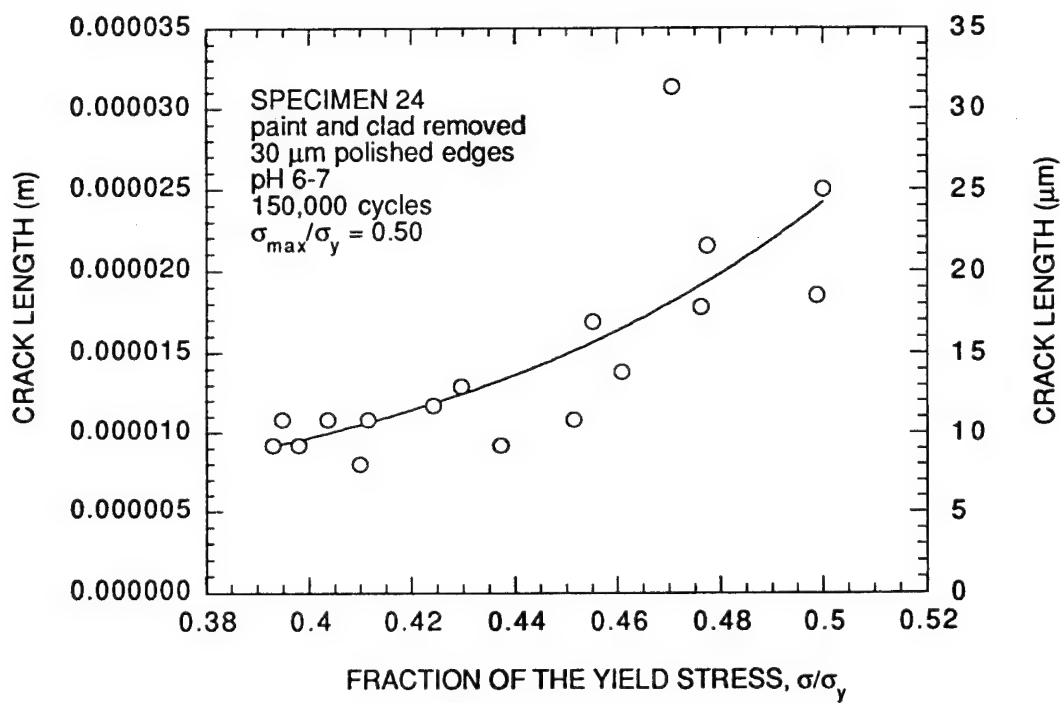


Figure A-18. Crack length data measurements and the least squares fit for Test 24.

$y = m1 \cdot \exp(20000 \cdot m0^2 \cdot 22177 \dots)$		
	Value	Error
m1	1.5737e-08	3.2812e-08
m2	2.1568e-09	4.8616e-10
Chisq	1.9397e-08	NA
R	0.87576	NA

The solid line is a least squares fit of the integrated form of the Paris Law to the data.

$m1 = a_{\text{initial}}$

$m2 = C$

where $da/dN = C (\Delta K)^2$.

a is in meters and ΔK is in $\text{MPa}\sqrt{\text{m}}$.

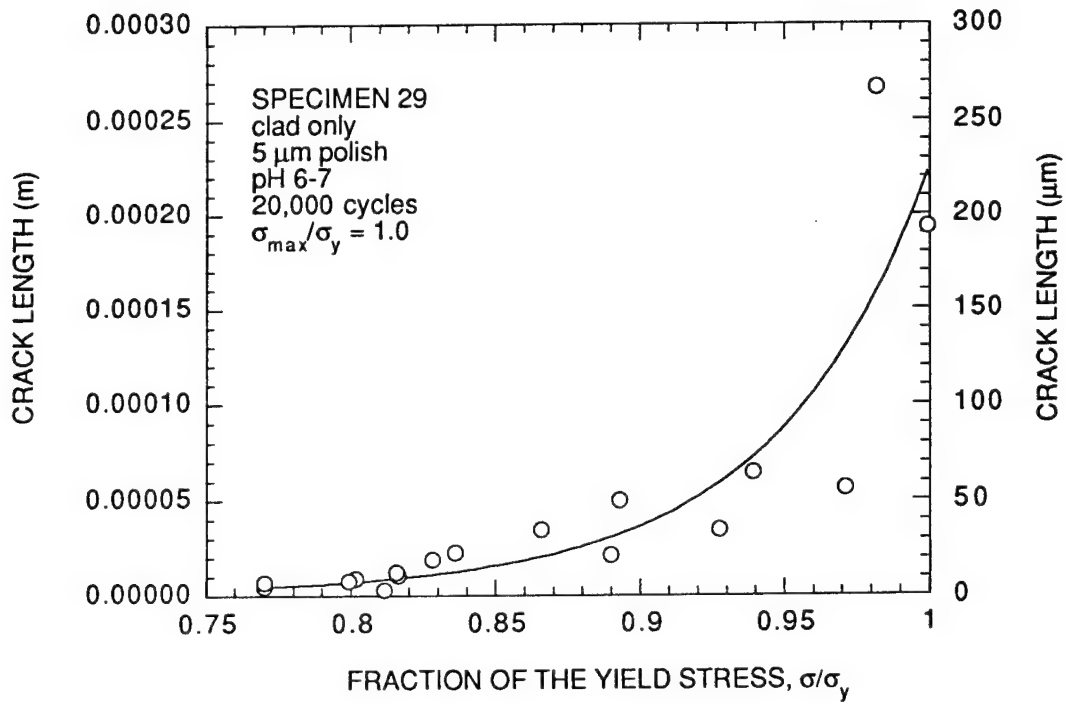


Figure A-19. Crack length data measurements and the least squares fit for Test 29.

$y = m1 \cdot \exp(105025 \cdot m0^2 \cdot 2217 \dots)$		
	Value	Error
m1	1.3523e-07	1.507e-07
m2	1.1254e-09	2.0649e-10
Chisq	2.4652e-09	NA
R	0.87409	NA

The solid line is a least squares fit of the integrated form of the Paris Law to the data.

$m1 = a_{\text{initial}}$

$m2 = C$

where $da/dN = C (\Delta K)^2$.

a is in meters and ΔK is in $\text{MPa}\sqrt{\text{m}}$.

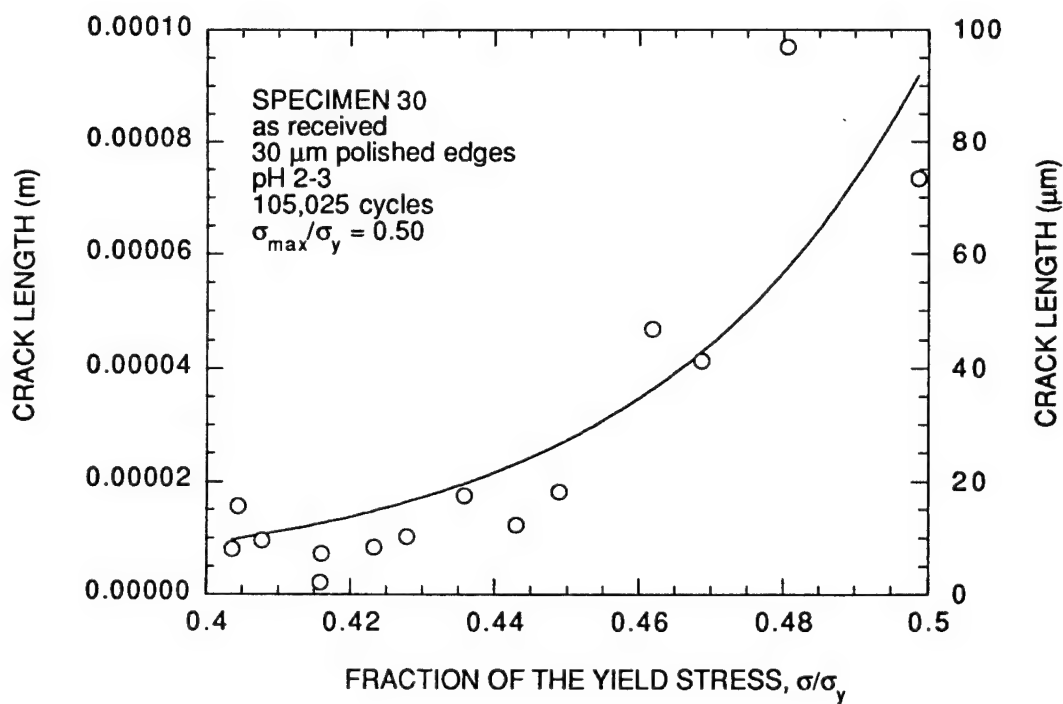


Figure A-20. Crack length data measurements and the least squares fit for Test 30.

$y = m1 \cdot \exp(24790 \cdot m0^{2 \cdot 22177...})$		
	Value	Error
m1	7.1881e-07	5.7633e-07
m2	1.379e-09	2.8021e-10
Chisq	1.1838e-09	NA
R	0.83651	NA

The solid line is a least squares fit of the integrated form of the Paris Law to the data.

$m1 = a_{\text{initial}}$

$m2 = C$

where $da/dN = C (\Delta K)^2$.

a is in meters and ΔK is in $\text{MPa}\sqrt{\text{m}}$.

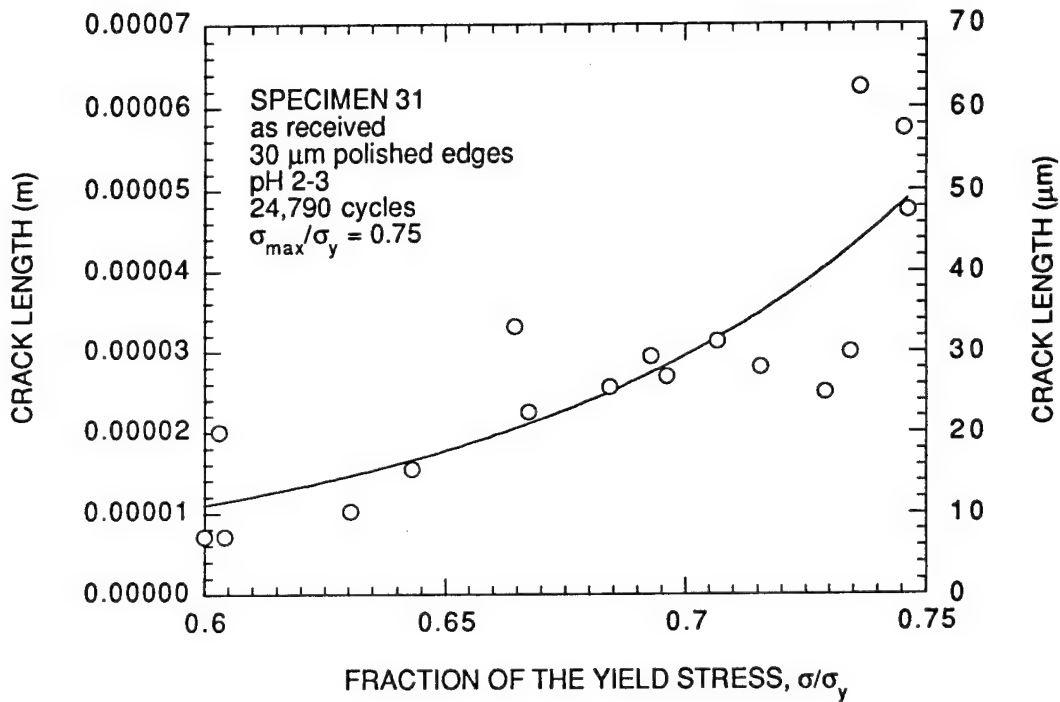


Figure A-21. Crack length data measurements and the least squares fit for Test 31.

$y = m1 \cdot \exp(80880 \cdot m0^2 \cdot 22177 \dots)$		
	Value	Error
m1	1.7359e-05	1.0492e-05
m2	3.0043e-10	1.5133e-10
Chisq	1.2698e-09	NA
R	0.58163	NA

The solid line is a least squares fit of the integrated form of the Paris Law to the data.

$m1 = a_{\text{initial}}$

$m2 = C$

where $da/dN = C (\Delta K)^2$.

a is in meters and ΔK is in $\text{MPa}\sqrt{\text{m}}$.

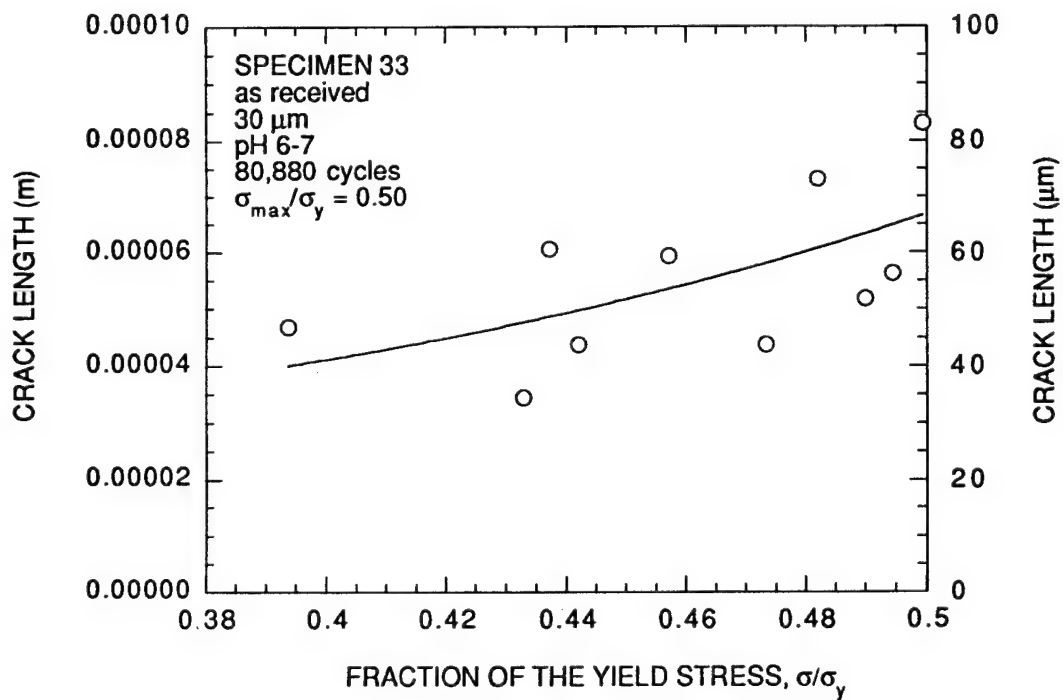


Figure A-22. Crack length data measurements and the least squares fit for Test 33.

$y = m1 \cdot \exp(30000 \cdot m0^2 \cdot 22177 \dots)$		
	Value	Error
m1	2.1271e-06	2.1917e-06
m2	9.2183e-10	3.049e-10
Chisq	3.5979e-09	NA
R	0.61043	NA

The solid line is a least squares fit of the integrated form of the Paris Law to the data.

$m1 = a_{\text{initial}}$

$m2 = C$

where $da/dN = C (\Delta K)^2$.

a is in meters and ΔK is in $\text{MPa}\sqrt{\text{m}}$.

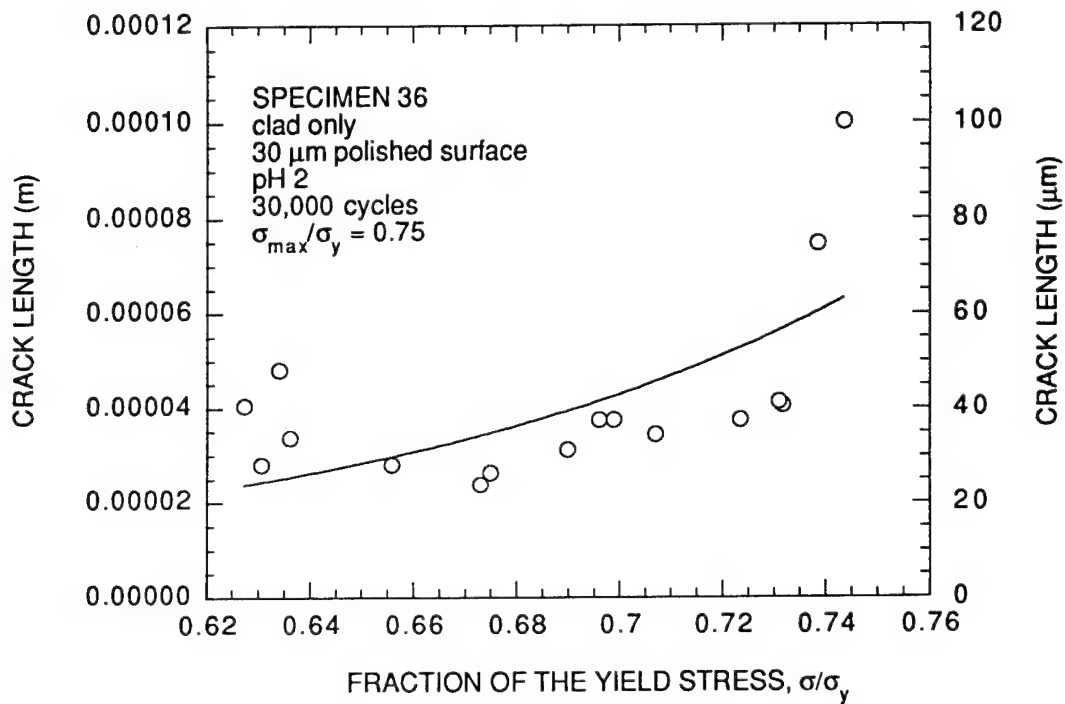


Figure A-23. Crack length data measurements and the least squares fit for Test 36.

$y = m1 \cdot \exp(28600 \cdot m0^2 \cdot 22177 \dots)$		
	Value	Error
m1	9.6813e-08	1.0663e-07
m2	4.2623e-09	7.3356e-10
Chisq	1.4905e-09	NA
R	0.90727	NA

The solid line is a least squares fit of the integrated form of the Paris Law to the data.

$m1 = a_{\text{initial}}$

$m2 = C$

where $da/dN = C (\Delta K)^2$.

a is in meters and ΔK is in $\text{MPa}\sqrt{\text{m}}$.

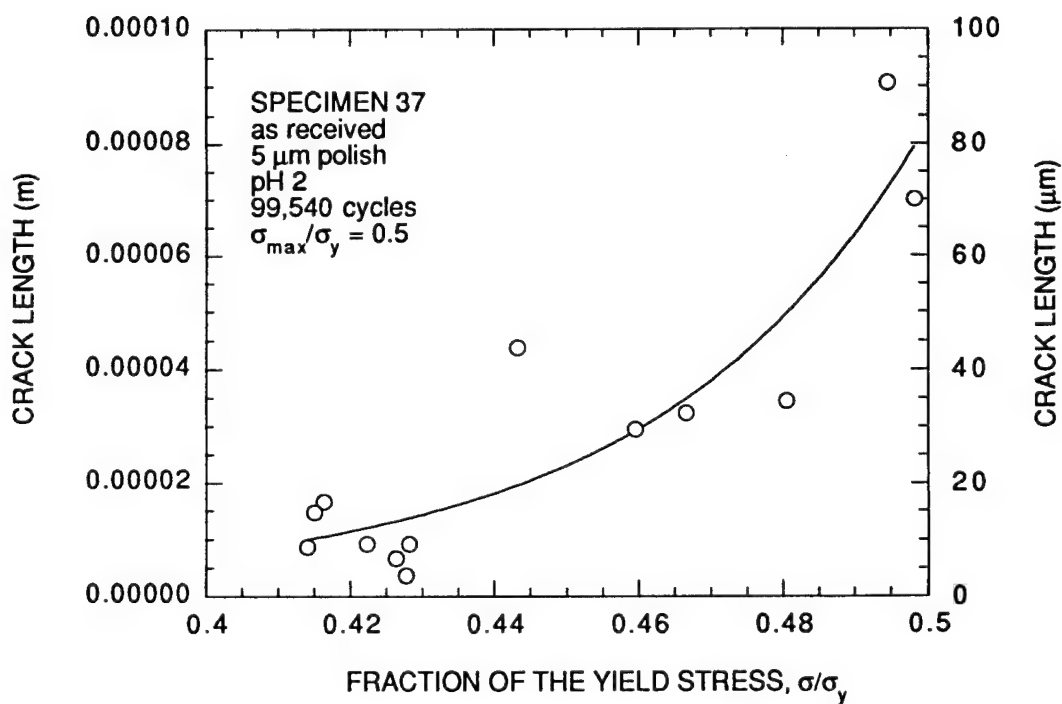


Figure A-24. Crack length data measurements and the least squares fit for Test 37.

y = m1*exp(94310*m0^ 2*22177...		
	Value	Error
m1	3.7912e-07	3.5108e-07
m2	8.8967e-10	1.9183e-10
Chisq	2.7854e-10	NA
R	0.86568	NA

The solid line is a least squares fit of the integrated form of the Paris Law to the data.
 $m1 = a_{\text{initial}}$
 $m2 = C$
 where $da/dN = C (\Delta K)^2$.
 a is in meters and ΔK is in $\text{MPa}\sqrt{\text{m}}$.

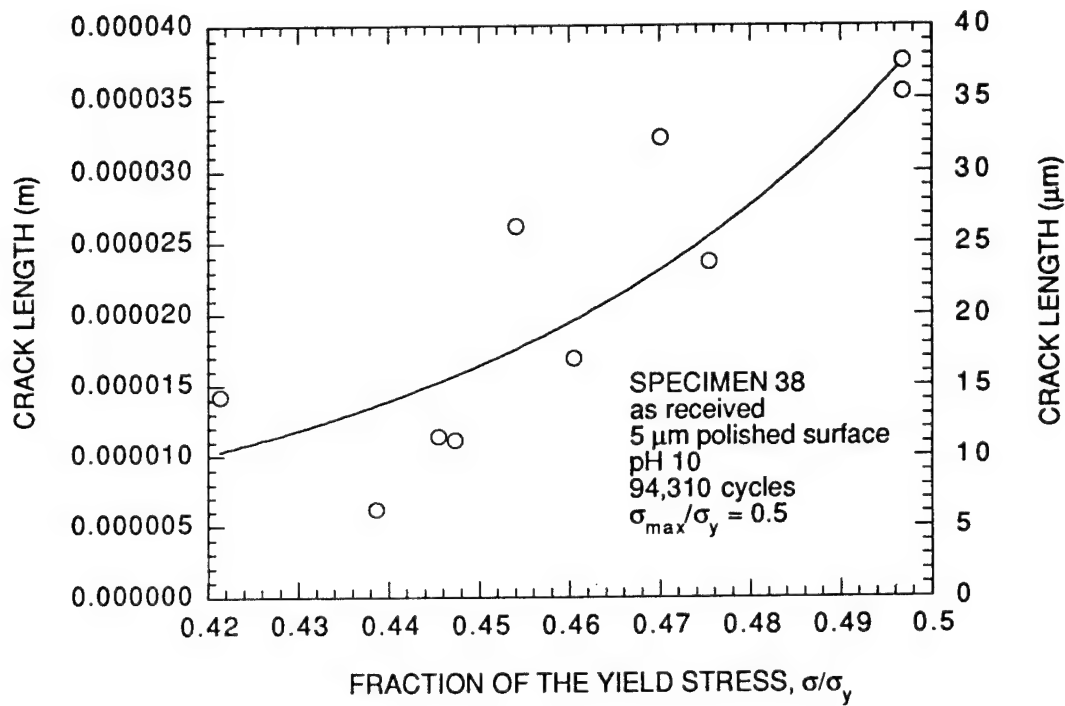


Figure A-25. Crack length data measurements and the least squares fit for Test 38.

$y = m1 \cdot \exp(80060 \cdot m0^{\wedge} 2 \cdot 22177 \dots)$		
	Value	Error
m1	1.6635e-07	1.5816e-07
m2	1.3493e-09	2.2751e-10
Chisq	1.0191e-09	NA
R	0.91649	NA

The solid line is a least squares fit of the integrated form of the Paris Law to the data.

$m1 = a_{\text{initial}}$

$m2 = C$

where $da/dN = C (\Delta K)^2$.

a is in meters and ΔK is in $\text{MPa}\sqrt{\text{m}}$.

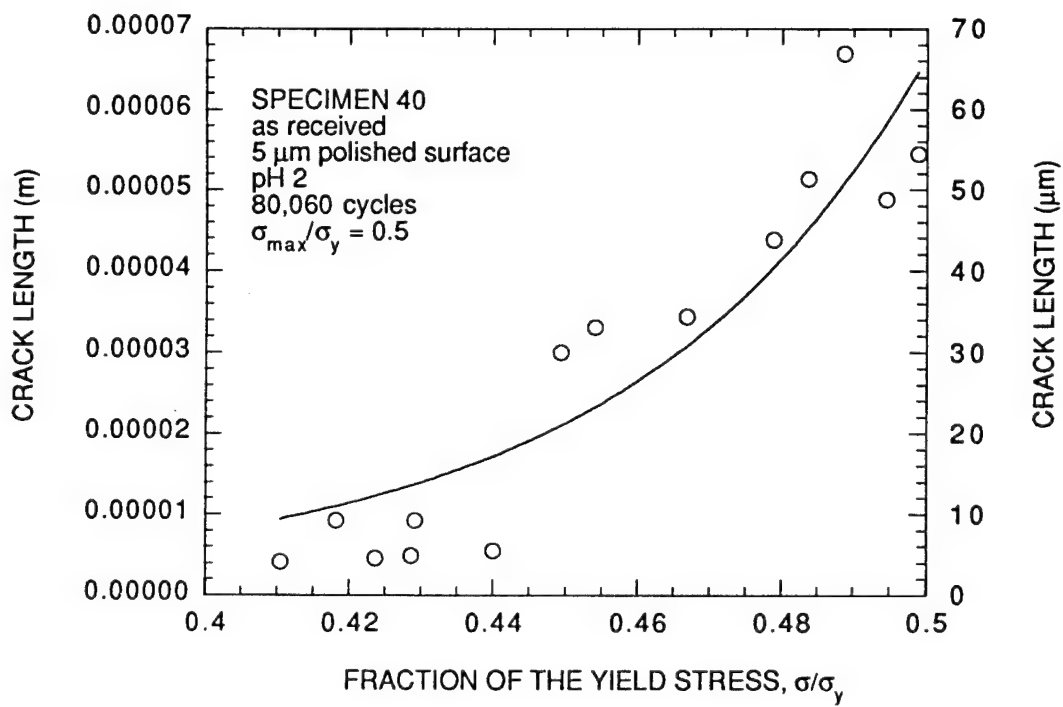


Figure A-26. Crack length data measurements and the least squares fit for Test 40.

$y = m1 \cdot \exp(150000 \cdot m0^{\wedge} 2^{2217} \dots)$		
	Value	Error
m1	1.5181e-09	9.2361e-09
m2	1.6249e-09	7.7589e-10
Chisq	5.9746e-07	NA
R	0.73461	NA

The solid line is a least squares fit of the integrated form of the Paris Law to the data.

$m1 = a_{\text{initial}}$

$m2 = C$

where $da/dN = C (\Delta K)^2$.

a is in meters and ΔK is in $\text{MPa}\sqrt{\text{m}}$.

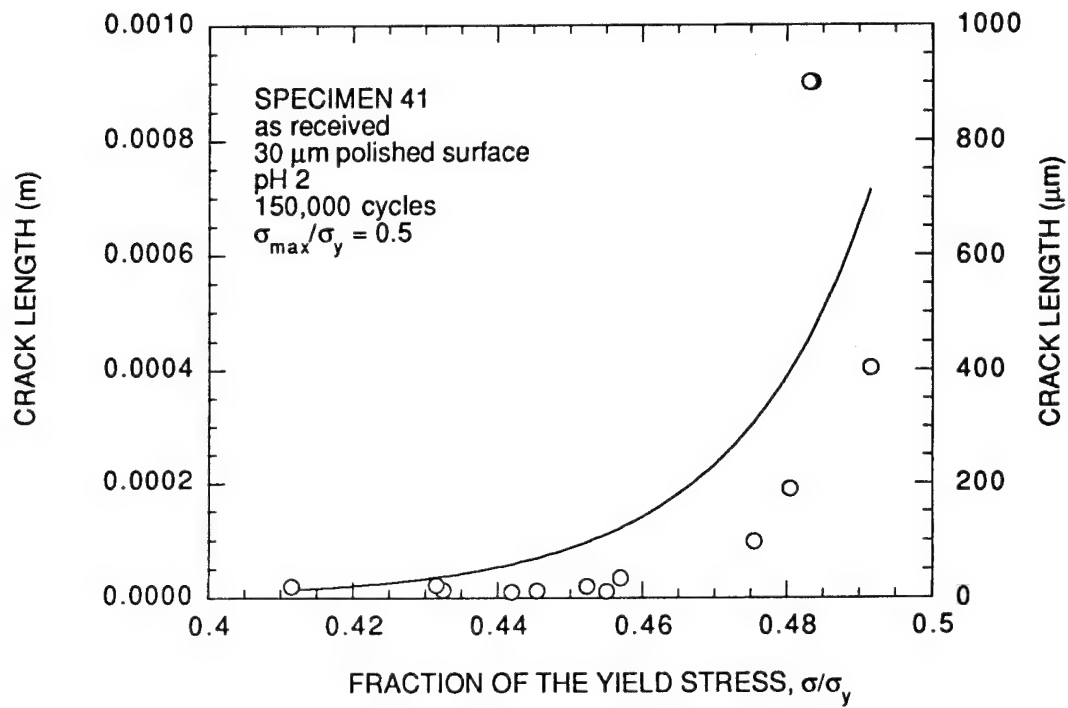


Figure A-27. Crack length data measurements and the least squares fit for Test 41.

$y = m1 \cdot \exp(125160 \cdot m0^{\wedge} 2 \cdot 2217 \dots)$		
	Value	Error
m1	4.6683e-10	2.1577e-09
m2	1.953e-09	7.002e-10
Chisq	6.4384e-08	NA
R	0.71801	NA

The solid line is a least squares fit of the integrated form of the Paris Law to the data.

$m1 = a_{\text{initial}}$

$m2 = C$

where $da/dN = C (\Delta K)^2$.

a is in meters and ΔK is in $\text{MPa}\sqrt{\text{m}}$.

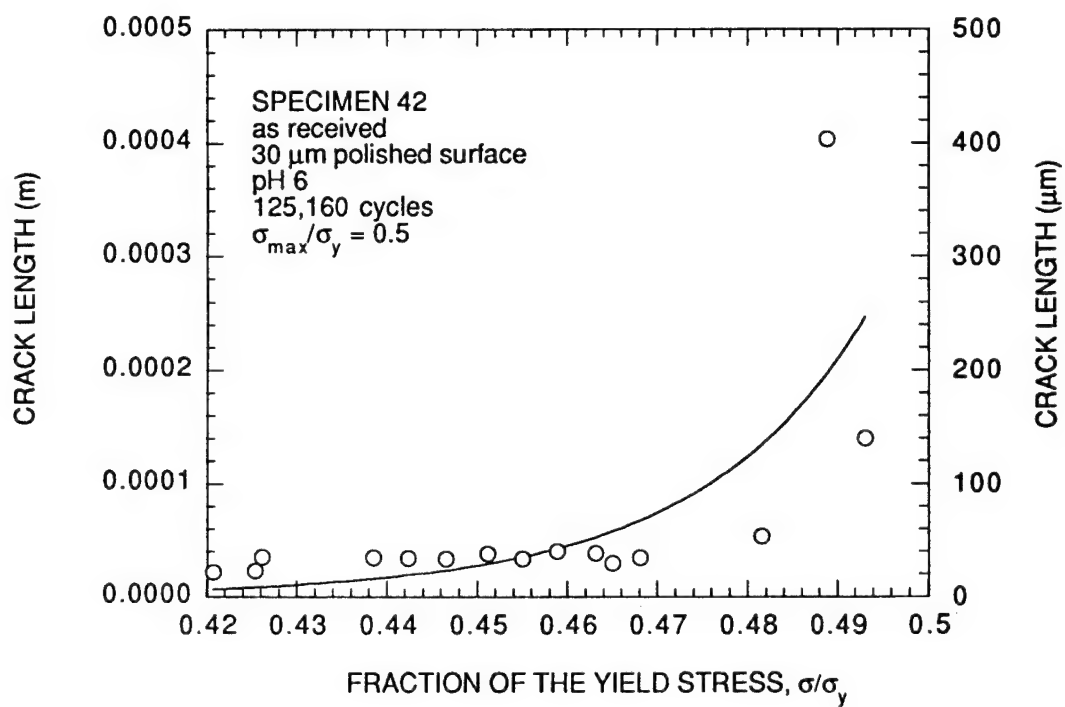


Figure A-28. Crack length data measurements and the least squares fit for Test 42.

y = m1*exp(150000*m0^ 2*2217...		
	Value	Error
m1	2.2383e-09	2.6621e-09
m2	1.4902e-09	1.4788e-10
Chisq	2.2755e-09	NA
R	0.99313	NA

The solid line is a least squares fit of the integrated form of the Paris Law to the data.

$m1 = a_{\text{initial}}$

$m2 = C$

where $da/dN = C (\Delta K)^2$.

a is in meters and ΔK is in $\text{MPa}\sqrt{\text{m}}$.

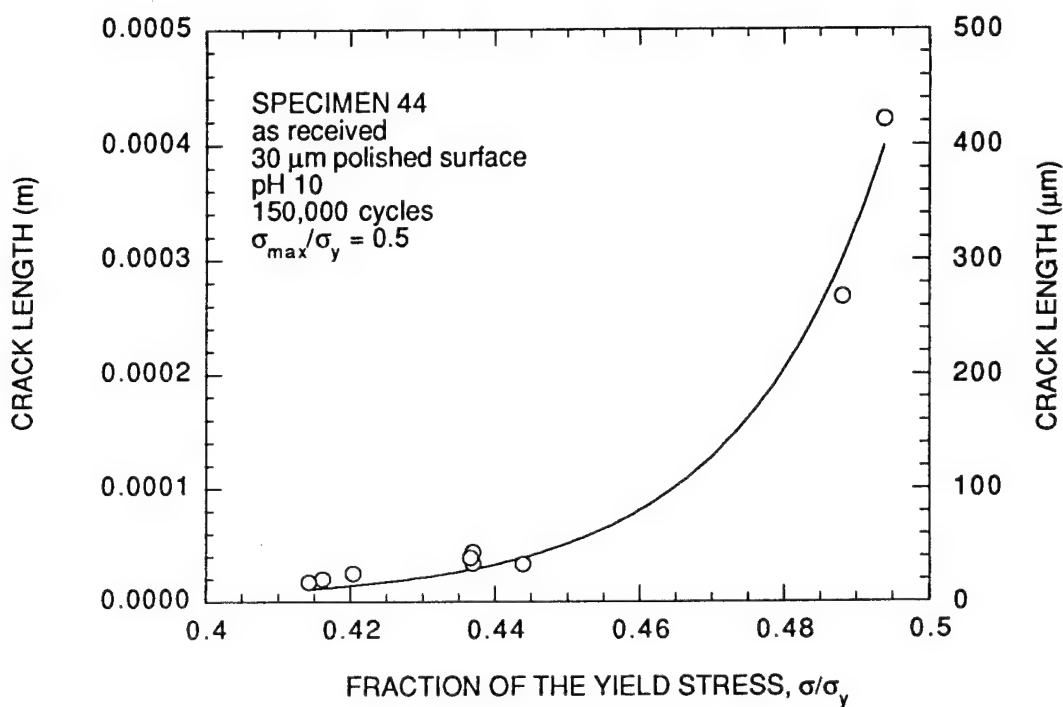


Figure A-29. Crack length data measurements and the least squares fit for Test 44.

$y = m1 \cdot \exp(150000 \cdot m0^2 \cdot 2217 \dots)$		
	Value	Error
m1	4.4553e-07	2.8948e-07
m2	5.8961e-10	8.4785e-11
Chisq	3.0123e-10	NA
R	0.92616	NA

The solid line is a least squares fit of the integrated form of the Paris Law to the data.

$m1 = a_{\text{initial}}$

$m2 = C$

where $da/dN = C (\Delta K)^2$.

a is in meters and ΔK is in $\text{MPa}\sqrt{\text{m}}$.

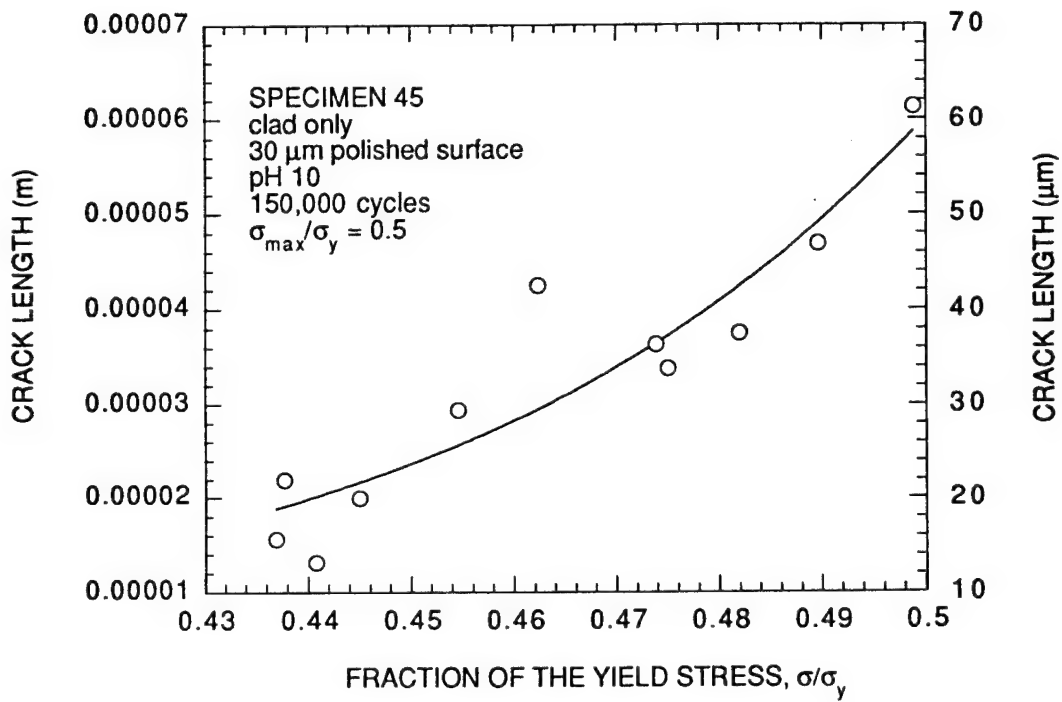


Figure A-30. Crack length data measurements and the least squares fit for Test 45.

y = m1*exp(30000*m0^ 2*22177...		
	Value	Error
m1	2.1149e-06	1.3897e-06
m2	8.4088e-10	1.9031e-10
Chisq	5.2675e-10	NA
R	0.8185	NA

The solid line is a least squares fit of the integrated form of the Paris Law to the data.

$m1 = a_{\text{initial}}$

$m2 = C$

where $da/dN = C (\Delta K)^2$.

a is in meters and ΔK is in $\text{MPa}\sqrt{\text{m}}$.

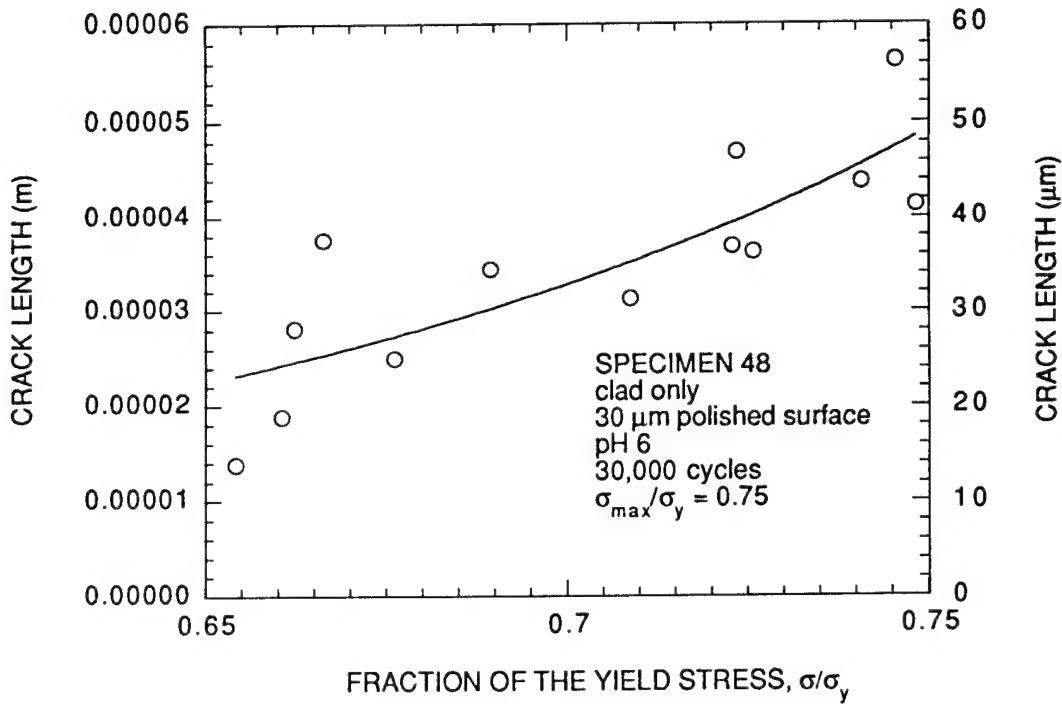


Figure A-31. Crack length data measurements and the least squares fit for Test 48.

$y = m1 \cdot \exp(30000 \cdot m0^2 \cdot 22177 \dots)$		
	Value	Error
m1	1.997e-05	1.0535e-05
m2	2.0777e-10	1.6002e-10
Chisq	4.6572e-10	NA
R	0.39698	NA

The solid line is a least squares fit of the integrated form of the Paris Law to the data.

$m1 = a_{\text{initial}}$

$m2 = C$

where $da/dN = C (\Delta K)^2$.

a is in meters and ΔK is in $\text{MPa}\sqrt{\text{m}}$.

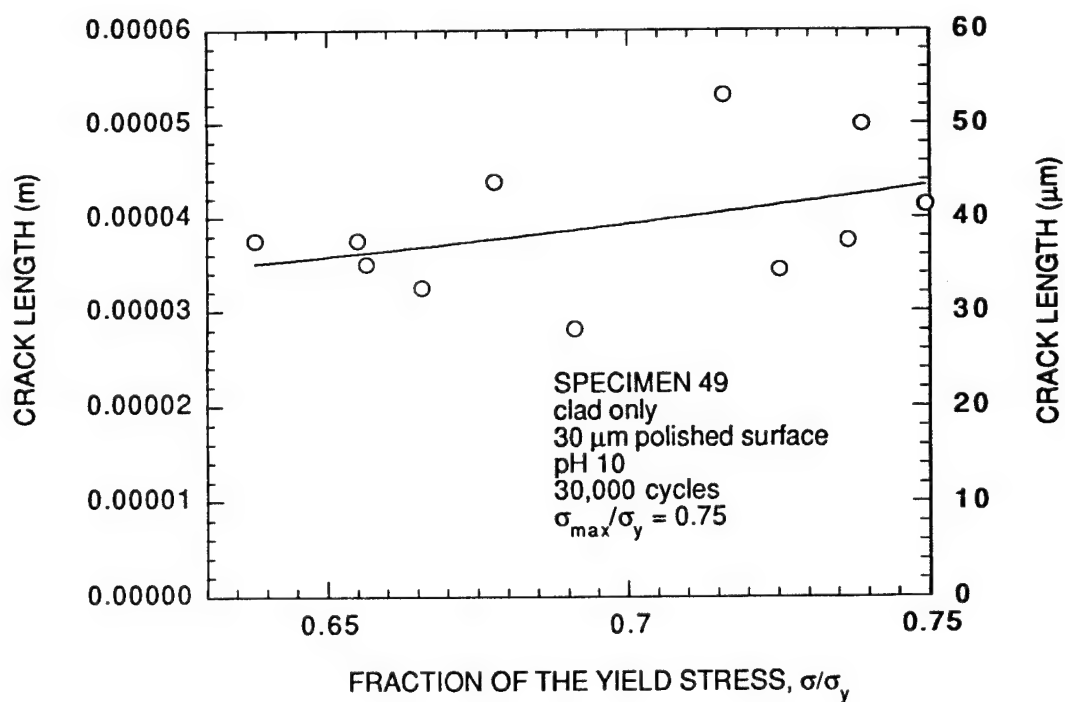


Figure A-32. Crack length data measurements and the least squares fit for Test 49.

y = m1*exp(20000*m0^ 2*22177...		
	Value	Error
m1	3.8523e-07	3.7279e-07
m2	1.2214e-09	2.3689e-10
Chisq	4.8821e-09	NA
R	0.77451	NA

The solid line is a least squares fit of the integrated form of the Paris Law to the data.

$m1 = a_{\text{initial}}$

$m2 = C$

where $da/dN = C (\Delta K)^2$.

a is in meters and ΔK is in $\text{MPa}\sqrt{\text{m}}$.

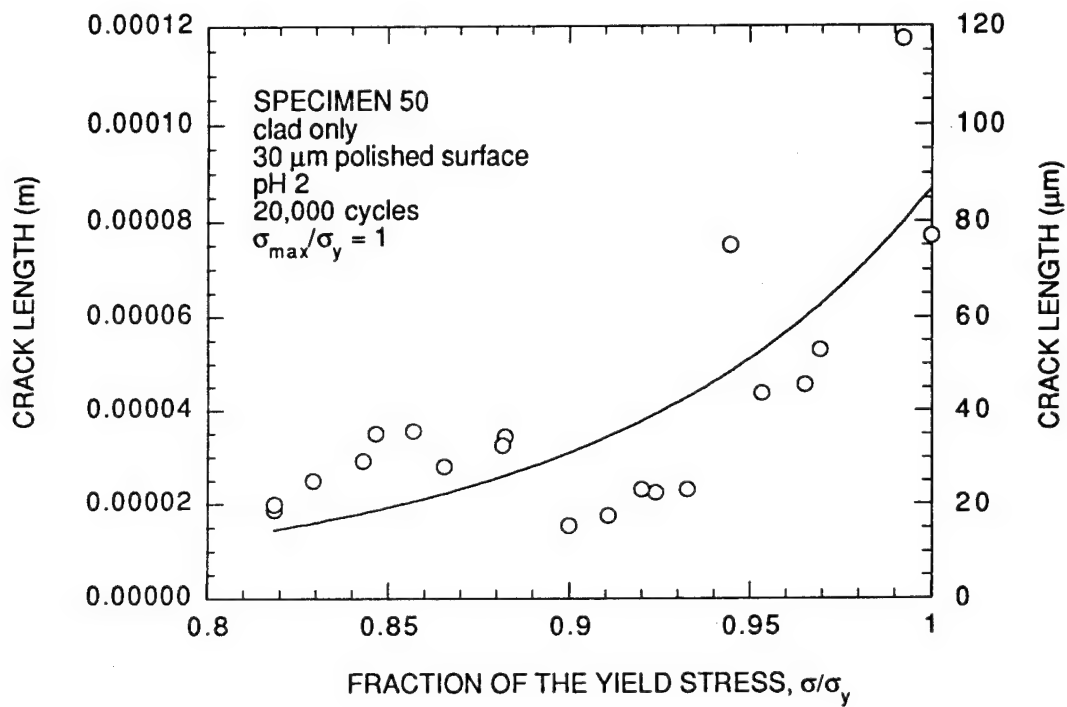


Figure A-33. Crack length data measurements and the least squares fit for Test 50.

y = m1*exp(20000*m0^ 2*22177...		
	Value	Error
m1	2.3484e-07	1.5504e-07
m2	1.2889e-09	1.6184e-10
Chisq	1.126e-09	NA
R	0.9065	NA

The solid line is a least squares fit of the integrated form of the Paris Law to the data.

$m1 = a_{\text{initial}}$

$m2 = C$

where $da/dN = C (\Delta K)^2$.

a is in meters and ΔK is in $\text{MPa}\sqrt{\text{m}}$.

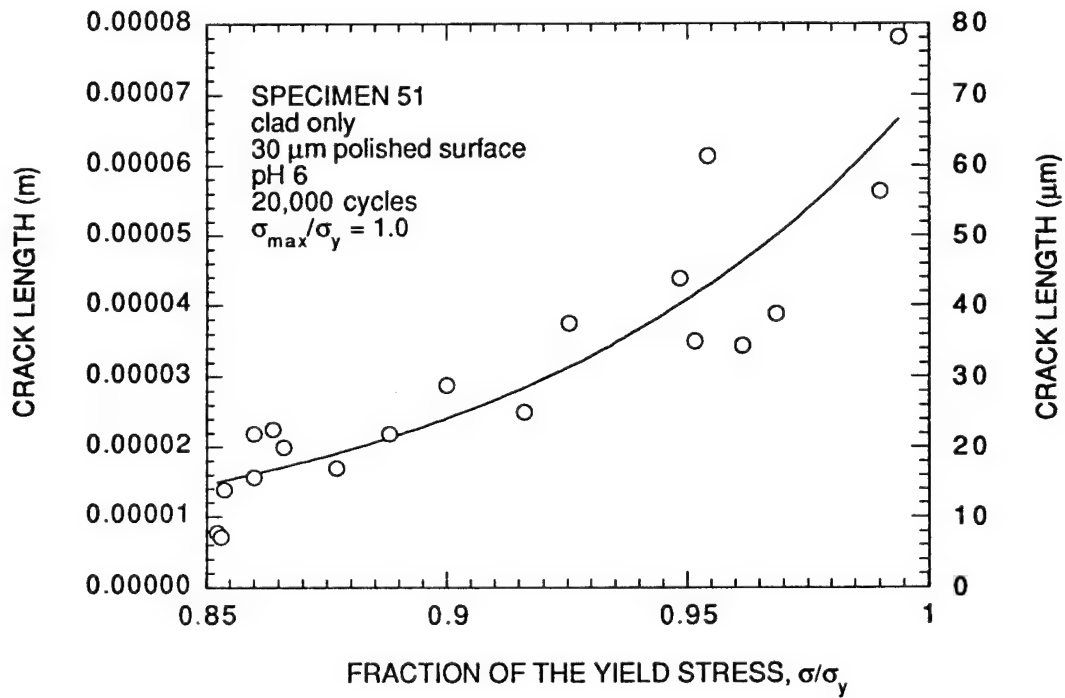


Figure A-34. Crack length data measurements and the least squares fit for Test 51.

$y = m1 \cdot \exp(30000 \cdot m0^2 \cdot 22177 \dots)$		
	Value	Error
m1	1.3716e-06	9.0632e-07
m2	9.7049e-10	1.9563e-10
Chisq	6.7757e-10	NA
R	0.79944	NA

The solid line is a least squares fit of the integrated form of the Paris Law to the data.

$m1 = a_{\text{initial}}$

$m2 = C$

where $da/dN = C (\Delta K)^2$.

a is in meters and ΔK is in $\text{MPa}\sqrt{\text{m}}$.

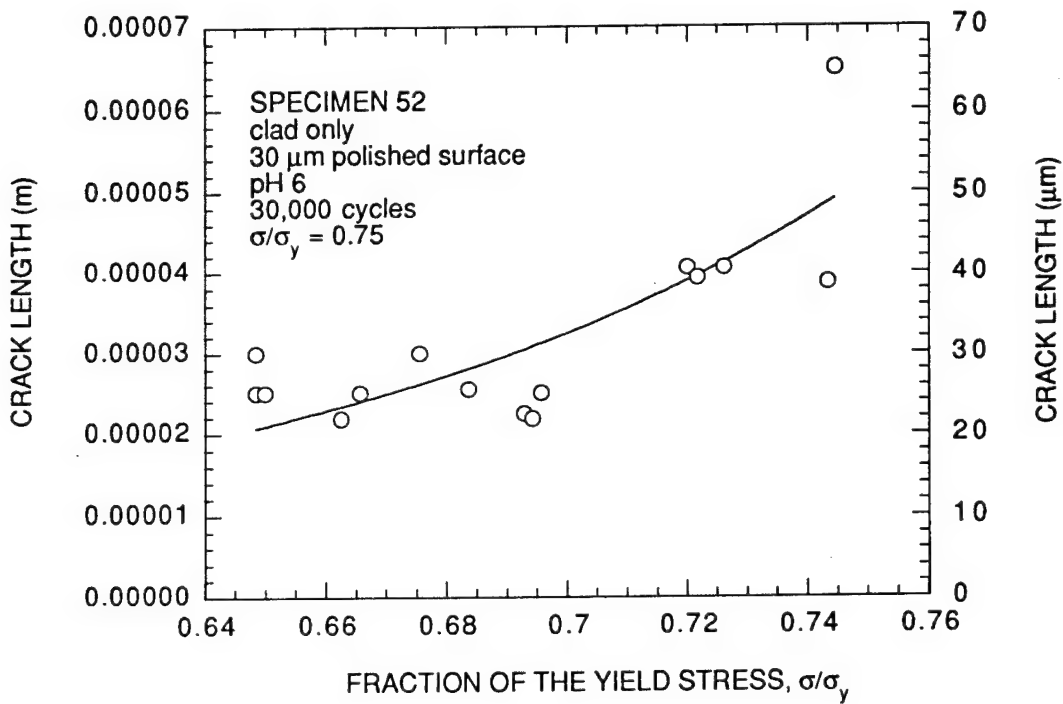


Figure A-35. Crack length data measurements and the least squares fit for Test 52.

y = m1*exp(30000*m0^ 2*22177...		
	Value	Error
m1	9.1005e-08	1.3584e-07
m2	1.6965e-09	4.1693e-10
Chisq	1.5693e-09	NA
R	0.79874	NA

The solid line is a least squares fit of the integrated form of the Paris Law to the data.

$m1 = a_{\text{initial}}$

$m2 = C$

where $da/dN = C (\Delta K)^2$.

a is in meters and ΔK is in $\text{MPa}\sqrt{\text{m}}$.

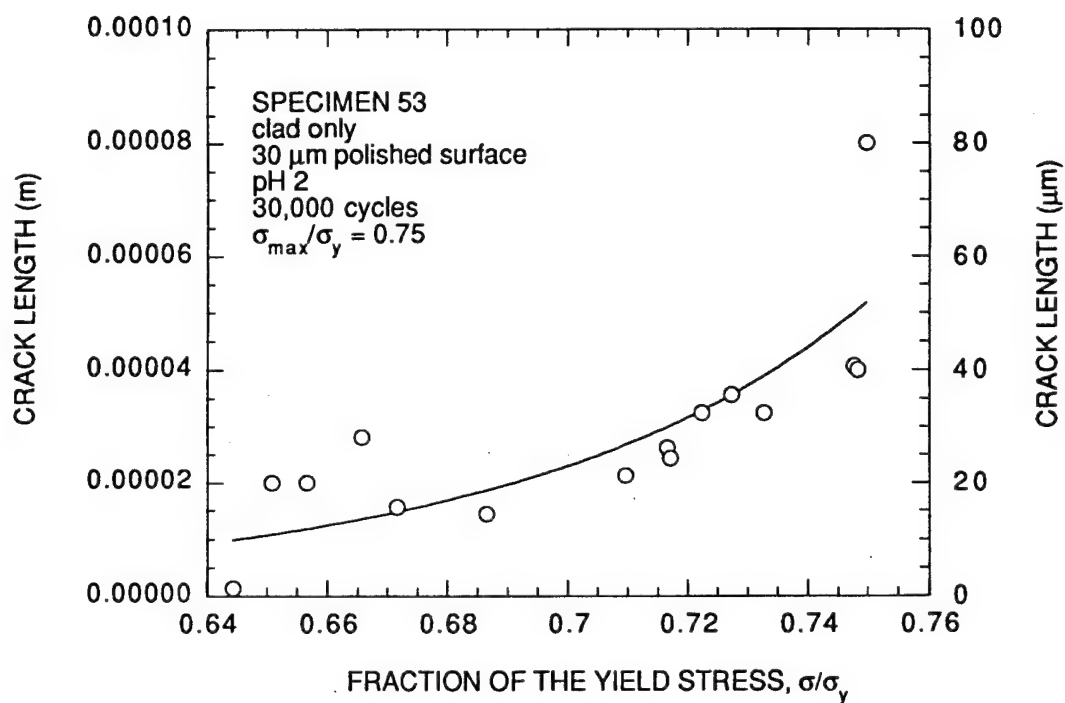


Figure A-36. Crack length data measurements and the least squares fit for Test 53.

y = m1*exp(97290*m0^ 2*22177...		
	Value	Error
m1	7.4308e-08	1.6686e-07
m2	1.4069e-09	4.4268e-10
Chisq	1.0904e-08	NA
R	0.77723	NA

The solid line is a least squares fit of the integrated form of the Paris Law to the data.

$m1 = a_{\text{initial}}$

$m2 = C$

where $da/dN = C (\Delta K)^2$.

a is in meters and ΔK is in $\text{MPa}\sqrt{\text{m}}$.

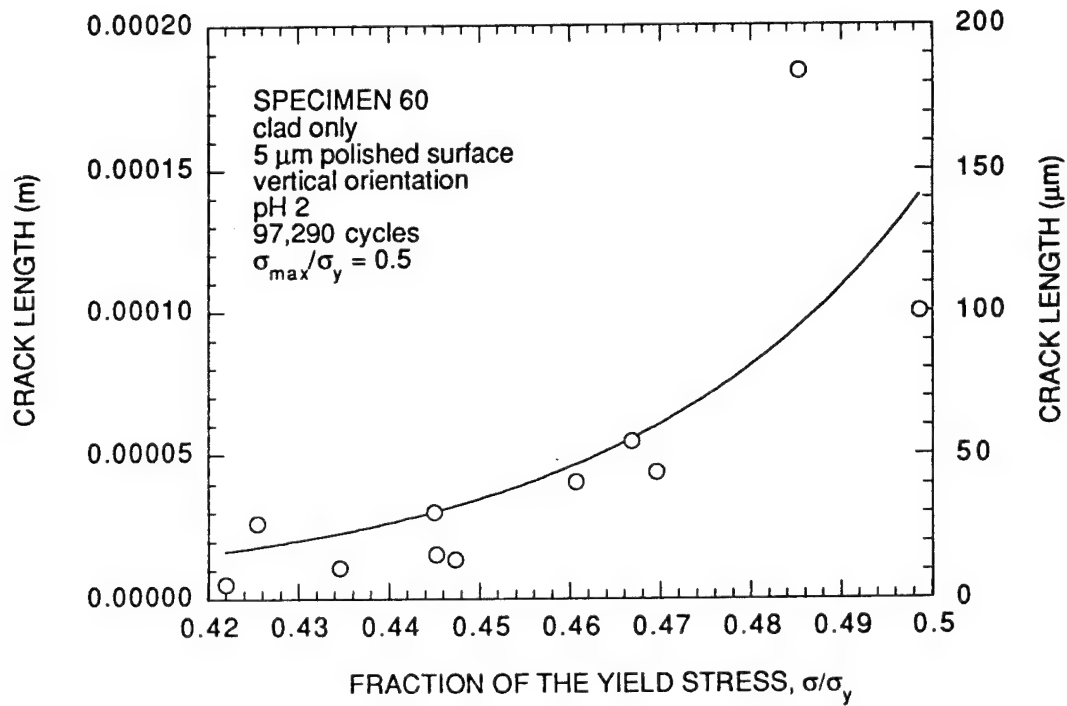


Figure A-37. Crack length data measurements and the least squares fit for Test 60.

$y = m1 \cdot \exp(150000 \cdot m0^{\wedge} 2 \cdot 2217 \dots)$		
	Value	Error
m1	1.3346e-06	2.4749e-06
m2	3.0126e-10	2.4385e-10
Chisq	2.0081e-10	NA
R	0.42223	NA

The solid line is a least squares fit of the integrated form of the Paris Law to the data.

$m1 = a_{\text{initial}}$

$m2 = C$

where $da/dN = C (\Delta K)^2$.

a is in meters and ΔK is in $\text{MPa}\sqrt{\text{m}}$.

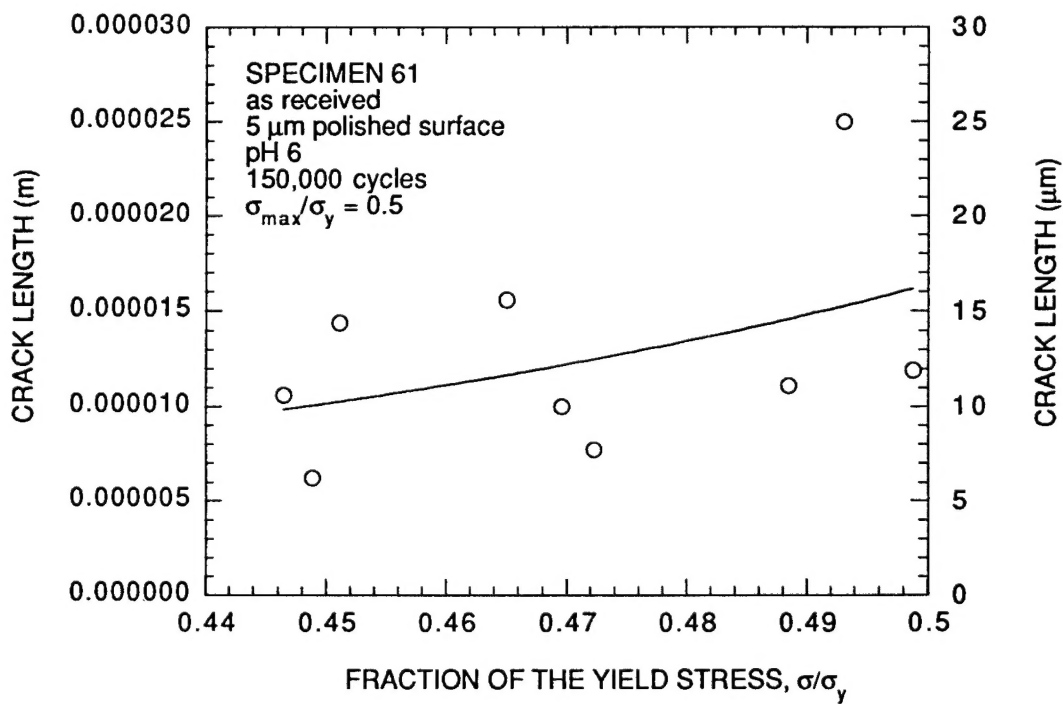


Figure A-38. Crack length data measurements and the least squares fit for Test 61.

$y = m1 \cdot \exp(74500 \cdot m0^2 \cdot 22177 \dots)$		
	Value	Error
m1	1.2336e-11	3.627e-11
m2	4.0941e-09	7.4575e-10
Chisq	7.3958e-09	NA
R	0.8921	NA

The solid line is a least squares fit of the integrated form of the Paris Law to the data.
 $m1 = a_{\text{initial}}$
 $m2 = C$
 where $da/dN = C (\Delta K)^2$.
 a is in meters and ΔK is in $\text{MPa}\sqrt{\text{m}}$.

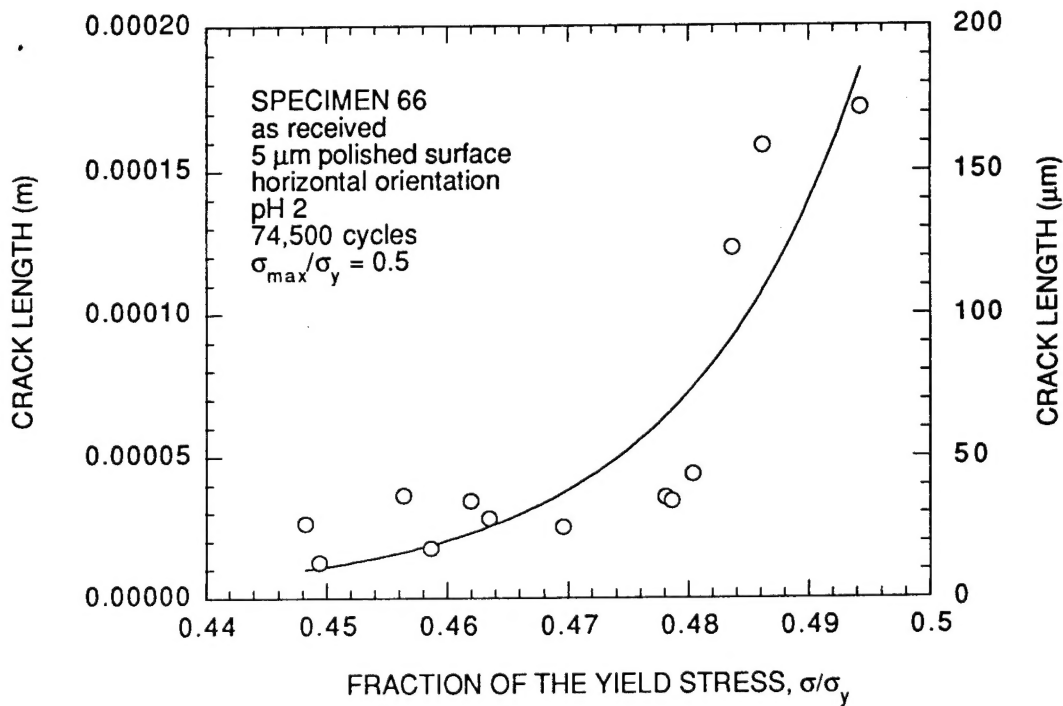


Figure A-39. Crack length data measurements and the least squares fit for Test 66.

$y = m1 \cdot \exp(150000 \cdot m0^{\wedge} 2 \cdot 2217 \dots)$		
	Value	Error
m1	8.2731e-06	8.7935e-06
m2	9.8239e-11	1.4642e-10
Chisq	5.9667e-10	NA
R	0.19332	NA

The solid line is a least squares fit of the integrated form of the Paris Law to the data.

$m1 = a_{\text{initial}}$

$m2 = C$

where $da/dN = C (\Delta K)^2$.

a is in meters and ΔK is in $\text{MPa}\sqrt{\text{m}}$.

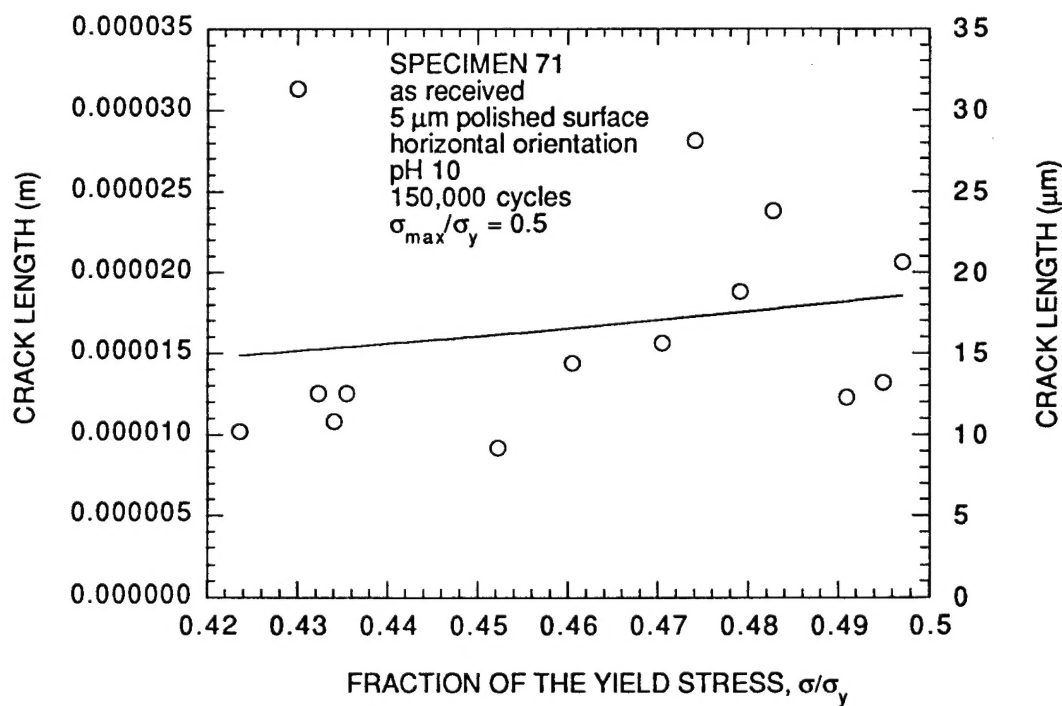


Figure A-40. Crack length data measurements and the least squares fit for Test 71.

y = m1*exp(125190*m0^ 2*2217...		
	Value	Error
m1	1.0386e-10	2.2612e-10
m2	2.0631e-09	3.3891e-10
Chisq	2.2203e-10	NA
R	0.96395	NA

The solid line is a least squares fit of the integrated form of the Paris Law to the data.

$m1 = a_{\text{initial}}$

$m2 = C$

where $da/dN = C (\Delta K)^2$.

a is in meters and ΔK is in $\text{MPa}\sqrt{\text{m}}$.

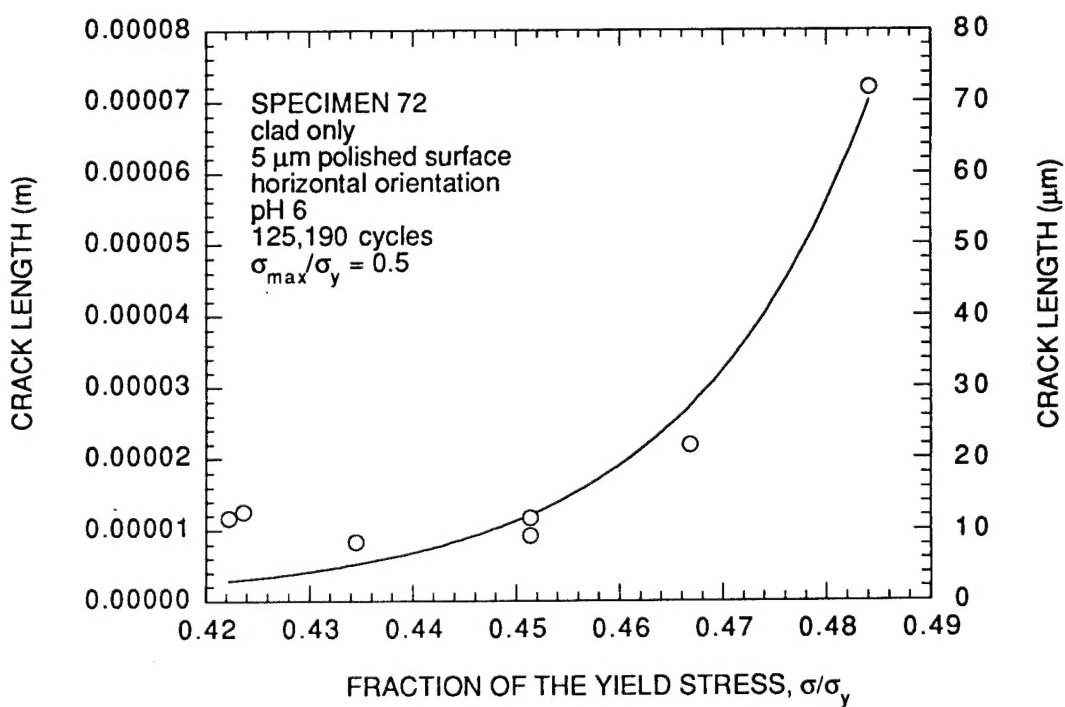


Figure A-41. Crack length data measurements and the least squares fit for Test 72.